DEVELOPING MASS SPECTROMETRIC METHODS FOR DISTINGUISHING ISOMERS, CHARACTERIZING COMPLEX MIXTURES AND DETERMINING THE CAPABILITY OF ORGANIC COMPOUNDS TO SWELL AIRCRAFT O-RING SEALS
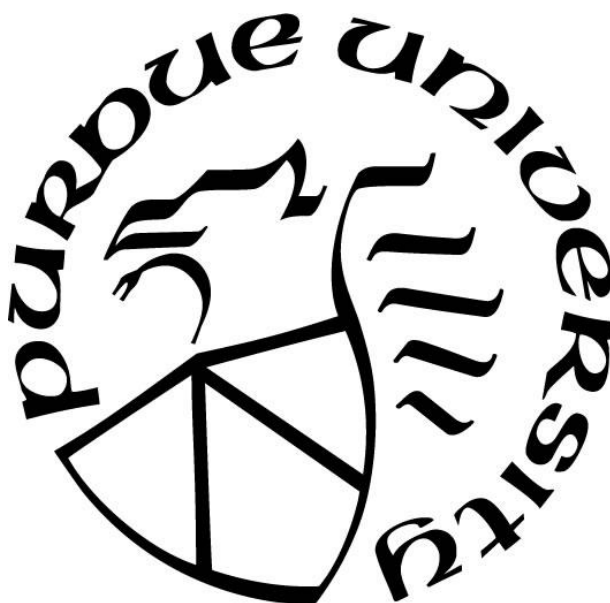
by

Mark Romanczyk

A Dissertation

Submitted to the Faculty of Purdue University

In Partial Fulfillment of the Requirements for the degree of

Doctor of Philosophy

Department of Chemistry

West Lafayette, Indiana

May 2019

THE PURDUE UNIVERSITY GRADUATE SCHOOL
STATEMENT OF COMMITTEE APPROVAL

Dr. Hilkka I. Kenttämaa, Chair

    Department of Chemistry

Dr. Kavita Shah

    Department of Chemistry

Dr. Chittaranjan Das

    Department of Chemistry

Dr. Alexander Laskin

    Department of Chemistry

Dr. John Davis

    School of Aviation and Transportation Technology

Approved by:

    Dr. Christine A. Hrycyna

        Head of the Graduate Program

To my beloved parents,

Roseann and David Romanczyk

You were my first teachers who taught me the value of hard work, nurtured my curiosity and faith and taught me to let true character be my compass.

ACKNOWLEDGMENTS

My first acknowledgement is to my research advisor, Professor Hilkka I. Kenttämaa. Her countless scientific achievements and accolades can only be outshined by her character, willingness and constant dedication to her graduate students and her altruistic personality. My success in graduate school was greatly influenced by her support, patience and guidance. From her mentorship, I gained scientific and instrumentation knowledge, learned how to effectively communicate in a clear and concise manner and learned technical writing. My success reflects her effort and time dedicated to teaching me. I am sincerely grateful for all she has done for me.

Past and present Kenttämaa group members have also contributed to my success. I would like to thank Dr. Chris Marcum for training me on my first mass spectrometer and his assistance and advice in graduate school. I would also like to thank Dr. Huaming Sheng, Dr. Weijuan Tang, Dr. Raghavendhar Kotha, Dr. Mckay Easton, Dr. Priya Murria, Dr. Hanyu Zhu, Dr. Yuan Jiang, Dr. Chunfen Jin and Dr. John Degenstein for their assistance and mentorship during my first few years in graduate school. I would also like to thank Dr. Ravikiran Yerabolu for his advice in the field of analytical chemistry during my years attending graduate school. I also would like to thank Dr. John Kong, Dr. Joann Max, Xueming Dong, Laurance Cain, Rashmi Kumar, Mingzhe Li, Xin Ma, Jacob Milton, Yuyang Zhang, Duanchen Ding, Jeremy Manheim, Edouard Niyonsaba, Katherine Wehde, Lan Xu, Zaikuan Yu, Leah Easterling, Hao-Ran Lei, Jifa Zhang, Erlu Feng, Brent Modereger and Judy Kuan-Yu Liu who I have thoroughly enjoyed working with these past few years.

I would also like to thank Dr. Gozdem Kilaz, Petr Vozka and Dr. Rodney Trice from Purdue University, Dr. Dianne J. Luning Prak from the U.S. Naval Academy, and Tiina Laaksonen and Kirsi Salorinne from Neste Oil.

TABLE OF CONTENTS

LIST OF TABLES

LIST OF FIGURES

ABSTRACT

Author: Romanczyk, Mark. PhD
Institution: Purdue University
Degree Received: May 2019
Title:Developing Mass Spectrometric Methods for Distinguishing Isomers, Characterizing Complex Mixtures and Determining the Capability of Organic Compounds to Swell Aircraft O-Ring Seals
Committee Chair: Hilkka I. Kenttämaa

Mass spectrometry is a powerful analytical tool for characterization of complex mixtures and determination of the structures of unknown compounds in mixtures. The sensitivity, acquisition speed and the wide range of different ionization methods and analyzers available has positioned mass spectrometry at the forefront of analytical techniques for providing thorough solutions to challenging problems. This dissertation focuses on research using high-resolution tandem mass spectrometry to distinguish ionized structural isomers and using high-resolution mass spectrometry coupled to two-dimensional gas chromatography (GCxGC) to determine chemical compositions for aviation fuels, alternative fuels, fuel additives and potential fuels, as well as on research using a variety of tools to determine the effectiveness of organic compounds to swell o-ring seals commonly found in aircraft fuel circulation systems.

Chapter 2 describes the instruments and ionization methods used to complete the research discussed in this dissertation. In Chapter 3, the success at differentiating ionized naphthene-containing structural isomers by using two collision-activated dissociation (CAD) methods, medium-energy collision-activated dissociation (MCAD) in an octupole collision cell and collision-activated dissociation in a linear quadrupole ion trap (ITCAD), is discussed. MCAD and ITCAD measurements were completed in the energy-resolved mass spectrometry (ERMS) mode. In Chapter 4, the chemical compositions of petroleum-based aviation fuels, alternative fuels, fuel

additives and potential fuels determined by using two-dimensional gas chromatography (GCxGC)/(electron ionization (EI)) high-resolution time-of-flight (TOF) mass spectrometry (GCxGC/(EI)TOF MS) is discussed. Identification of the compounds in fuels is important as the chemical composition influences the chemical and physical properties of the fuel that affect aircraft performance. Chapter 5 describes the effectiveness of different organic dopants to swell o-ring seals commonly used in airplanes.

CHAPTER 1.   INTRODUCTION

1.1   Introduction

At its simplest, mass spectrometry is an analytical tool that measures the mass-to-charge ratio of an ionized compound. More detailed information can also be obtained. For example, tandem mass spectrometry (MS[n]) involves isolation of an ionized compound and examination of its reactions, usually in order to obtain structural information. On the other hand, high-resolution mass spectrometry can be used to determine the chemical formulas of unknown ions. Combining these two approaches results in high-resolution tandem mass spectrometry, an analytical technique that has proven to be extraordinarily powerful in a variety of disciplines, including fuel research,[1] petroleomics[2] and pharmaceutical research.[3]

To produce a mass spectrum, four steps are required: sample evaporation, ionization, ion separation and detection.[4] The sample molecules are first brought into the gas phase by evaporation and nearly simultaneously or subsequently ionized. Most modern ionization methods combine the evaporation and ionization steps. The ions are then separated from each other based on their mass-to-charge (m/z) ratios by using one of many different approaches, including a scanning magnetic field that separates ions based on their momentum, a stationary magnetic field that separates ions based on their frequency of motion, or a flight tube that separates ions based on their flight time. Lastly the ions are detected, and their abundances are determined. A mass spectrum typically displays the m/z ratios of ions on the x-axis and their relative abundances on the y-axis.

Tandem mass spectrometry (MS[n]) experiments are one common method used to identify the ion structures. Many types of tandem mass spectrometers are commercially available, such as triple quadrupole mass spectrometers,[5] linear quadrupole ion trap instruments, [6] and Fourier-transform ion cyclotron resonance mass spectrometers.[7] In this dissertation, structural information for ions

was obtained by using collision-activated dissociation (CAD) in a linear quadrupole ion trap (LQIT) and in an octupole collision cell. In these CAD experiments, ions produced in the ion source are isolated, subjected to energetic collisions with a target gas, and dissociate to produce fragment ions that are detected and used to elucidate the structures of the ions.[7,8]

1.2   Thesis Overview

The research described in this dissertation focuses on several areas: developing analytical methods to distinguish structural isomers, identifying the chemical compositions of aviation fuels and evaluating the effectiveness of organic dopants to swell aircraft o-ring seals. Chapter 2 discusses fundamental aspects of mass spectrometry, and ionization methods and the instrumentation used to complete this research. The instruments include a linear quadrupole ion trap (LQIT), a LQIT coupled to a high-resolution orbitrap mass spectrometer, and a two-dimensional gas chromatograph (GCxGC)/(electron ionization (EI)) high-resolution time-of-flight (TOF) mass spectrometer (GCxGC/(EI)TOF MS).

Chapter 3 discusses and compares two activation methods used to distinguish ionized structural isomers. This work was supported by the Finnish oil company, Neste. Ionized naphthene-containing aromatic structural isomers were subjected to collision-activated dissociation (CAD) in an ion trap (ITCAD) and to medium-energy collision-activated dissociation (MCAD) in an octupole collision cell, both in the energy-resolved mass spectrometry mode (ERMS). MCAD was shown to be superior over ITCAD at the structural differentiation of the ionized isomers. MCAD imparted greater internal energies into the activated ions compared to ITCAD. Triplicate measurements completed by using MCAD were more reproducible than for ITCAD.

,Determination of the chemical compositions of petroleum-based jet and diesel fuels, potential alternative fuels and fuel blending components by using a GCxGC/(EI)TOF MS is discussed in chapter 4. This study was funded by the Naval Enterprise Partnership Teaming with Universities for National Excellence (NEPTUNE) program through the Office of Naval Research (ONR 33). The ability to determine the chemical compositions of fuels and to correlate the identified compounds and their concentrations to the physical and chemical properties and aircraft performance of the fuels is vital for the development of future resilient, alternative fuels. The chemical compositions of petroleum-based fuels were found to be different from potential alternative fuels. The MW range of hydrocarbons in petroleum-based fuels is wider than in potential alternative fuels. Further, more polycyclic aromatic hydrocarbons were found in the petroleum-based fuels than in the alternative fuels. Additional studies showed that some harmful compounds (*i.e.,* alkenes and heteroatom-containing compounds) have GCxGC elution times that are similar to those of saturated hydrocarbons. Hence, harmful compounds may be assigned incorrectly to a wrong chemical category (*i.e.,* cycloalkanes) based solely on elution times and qualitative elution boundaries determined using model compounds. However, harmful compounds were identified by using GCxGC/(EI)TOF MS. The harmful compounds may decrease the storage stability and combustion properties of fuel.

Chapter 5 discusses the effectiveness of aromatic and nonaromatic compounds in swelling air craft o-ring seals, which prevents leaks in the fuel circulation systems. This work was also supported by the NEPTUNE program. Aromatic compounds have been previously shown to swell o-ring seals more effectively than any other class of organic compounds found in jet fuel. However, aromatic compounds also produce the most soot and lead to the greatest carbon emissions. The aim of this study was to identify aromatic and nonaromatic compounds that most effectively swell

o-ring seals while generating as little soot and emissions as possible to be used in the future as dopants in alternative fuels. Steric effects were shown to decrease the efficiency of the compounds to swell seals. Ethylbenzene and indane were found to swell o-ring seals more effectively than any other compounds studied, including a currently approved alternative fuel. Finally, nonlinear correlations were found between the molar volume, molar mass and Hansen Solubility parameters of compounds and the volume swell percent.

1.3   References

1. Dietzel, K.D.; Campbell, J.L.; Bartlett, M.G.; Witten, M.L.; Fisher, J. W. Validation of a Gas Chromatography/Mass Spectrometry Method for the Quantification of Aerosolized Jet Propellant 8. *J. Chromatogr A* **2005**, *1093* (1-2), 11 – 20.

2. Marshall, A.G.; Rodgers, R.P. Petroleomics: Chemistry of the Underworld. *Proc. Natl. Acad. Sci. USA.* **2008**, *105* (47), 18090 – 18095.

3. Belas, F.J.; Blair, I.A. Mass Spectrometry in Pharmaceutical Analysis. *J. Liposome Res.* **2001**, *11* (4), 309 – 342.

4. de Hoffman, E.; Stroobant, V. Mass Spectrometry: Principles and Applications, 2nd Ed.; John Wiley and Sons, Ltd.: New York, 2002.

5. Yost, R.A.; Enke, C.G. Selected Ion Fragmentation with a Tandem Quadrupole Mass Spectrometer. *J. Am. Chem. Soc.* **1978**, *100* (7), 2274 – 2275.

6. March, R.E. An Introduction to Quadrupole Ion Trap Mass Spectrometry. *J. Mass Spectrom.* **1997** *32* (4), 351 – 367.

7. McLuckey, S.A.; Goeringer, D.E. Slow Heating Methos in Tandem Mass Spectrometry. *J. Mass Spectrom.* **1997**, *32* (5), *461 – 474.*

8. Busch, K.L.; Glish, G.L.; McLuckey, S.S. Mass Spectrometry/Mass Spectrometry: Techniques and Applications of Tandem Mass Spectrometry; VCH Publishers: New York, 1988.

CHAPTER 2.   INSTRUMENTATION AND EXPERIMENTAL PROCEDURES FOR THE LINEAR QUADRUPOLE ION TRAP MASS SPECTROMETER, HIGH RESOLUTION ORBITRAP MASS SPECTOMETER AND TWO-DIMENSIONAL GAS CHROMATOGRAPH / (ELECTRON IONIZATION) HIGH RESOLUTION TIME-OF-FLIGHT MASS SPECTROMETER

2.1   Introduction

Mass spectrometry is a powerful analytical tool that is used to address complex problems in many fields, such as fuel research,[1] petroleomics,[2] proteomics,[3] pharmaceutical studies, [4] forensics,[5] and environmental sciences.[6] The success and wide usage of mass spectrometry in scientific research is well founded on constant innovation, including development of new instruments, ionization methods and ion sources.[7-9] For example, John Fenn and Koichi Tanaka shared a Nobel Prize in 2002 for the development of electrospray ionization.

To complete mass spectrometric experiments, several steps must occur: 1) analytes are evaporated and ionized, 2) the ions are separated according to their mass-to-charge ratios (m/z), and 3) the ions are individually detected. A variety of methods are available for evaporation and ionization of compounds, such as atmospheric pressure chemical ionization (APCI),[10] electrospray ionization (ESI),[11] atmospheric pressure photon ionization (APPI),[12] and field ionization (FI).[13] It is noteworthy that the ionization efficiencies of analytes with different polarities and sizes vary for the different methods. Hence, it is critical to chose an ionization method that effectively ionizes the analyte(s) of interest. After ionization, ions can be separated based on their m/z-ratios by using a variety of different mass analyzers, including magnetic fields and flight tubes.

Prior to ion detection, tandem mass spectrometry (MS^n) experiments may be performed that provide structural information for the ions.[14] To complete MS^n experments, an ion of interest is isolated and its reactions are examined. The most common method, CAD, involves accelerating the ion and allowing it to collide with a target gas (usually helium, nitrogen or argon). Collisions

convert part of the kinetic energy of the ion into its internal energy. When the internal energy of the ion is greater than a dissociation threshold, the ion dissociates. The measured fragment ions may be further examined by isolating them and subjecting them to CAD.

In MS^n experiments, the parent or fragment ions may be isolated either in space or in time by using a scanning mass spectrometer or an ion trapping mass spectrometer, respectively. Scanning mass spectrometers perform different events (*i.e.,* ion isolation and dissociation) in different regions of the instrument. Conversely, ion trapping mass spectrometers perform different events (*i.e.,* ion isolation and dissociation) at the same location in the instrument but at different times. The MS^n experiments conducted in this disseration were mostly performed by using a LQIT mass spectrometer. Other instruments used to collect data for this disseration include a LQIT coupled to an orbitrap mass spectrometer and a two-dimensional gas chromatograph/electron ionization time of flight mass spectrometer .The details of these instruments are presented in the following sections.

2.2 Linear quadrupole ion trap (LQIT) mass spectrometer

Quadrupole ion traps are widely employed in commercial and academic laboratories[15] and have a wide variety of applications.[16] The LQIT has improved sensitivity and versatility compared to the first commercial quadrupole ion trap, the 3-D quadrupole ion trap.[17,18] A schematic of the Thermo Scientific LQIT mass spectrometer used in the research discussed here, including operational pressures and differential pumping rates, is shown in Figure 2.1. The LQIT contained four major regions: ion source box, atmospheric pressure ionization (API) stack, ion optics and the ion trap. The ion source box housed the API source (*i.e.,* electrospray ionization (ESI) probe or atmospheric pressure chemical ionization (APCI) probe) and was operated at 760 Torr. The pressure of the API stack was approximately 1 Torr and was maintained by two Edwards E2M30

rotary-vane mechanical pumps with an evacuation rate of 650 L/min. The pressure of the ion optics region ranged from 0.5 Torr up to 1×10^{-5} Torr and was maintained by a triple ported Leybold TW220/150/15S turbomolecular pump. The first, second and third inlets had evacuation rates of 25 L/s, 300L/s and 400 L/s, respectively. The ion trap region had a pressure of approximately 1×10^{-5} Torr, which was maintained by the third inlet of the turbomolecular pump. The pressure of the ion trap region was monitored by a cathode ionization gauge.
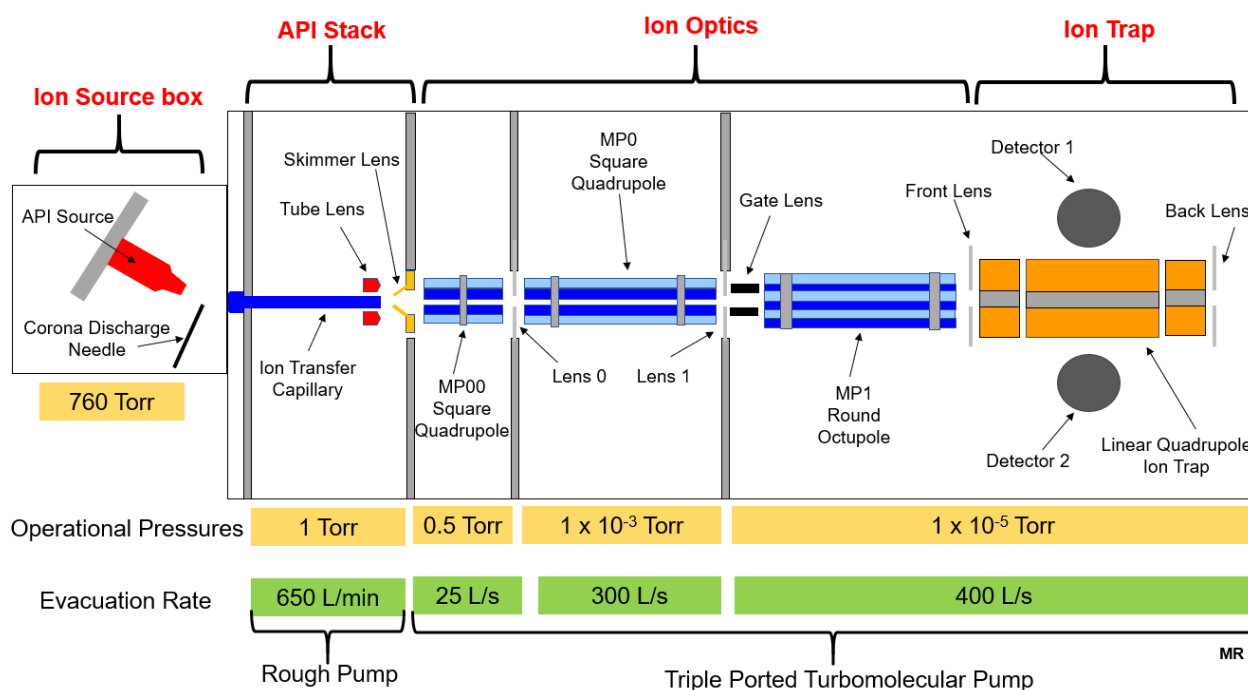
Figure 2.1 Labeled components and regions of a Thermo Scientific LQIT mass spectrometer with operational pressures (in yellow boxes) for each region of the instrument and the evacuation rates (in green boxes) of rough and turbomolecular pumps. The four major regions of the LQIT mass spectrometer are labeled in red bold letters.

2.2.1 Instrumentation

2.2.1.1 Ion source box and API stack

The ion source box housed an ionization source (*i.e.,* APCI or ESI source) that facilitated the evaporation and ionization of analytes prior to entering the API stack. For a detailed description

of APCI and ESI, please see sections 2.2.1.2 and 2.2.1.3, respectively. After analytes had been evaporated and ionized, the ions were entrained into the mass spectrometer by using a potential difference (0 – 20 V) between the ion source box and API stack and sheath and auxiliary gases (N_2) that flew through the ion source. The ions entered the mass spectrometer via the ion transfer capillary. Heat and DC voltage were applied to the ion transfer capillary to facilitate desolvation of the ions and enable transmission of the ions into the tube lens, respectively. A voltage was applied to the tube lens to transmit the ions into the off-centered opening of the skimmer lens. The motion of neutral compounds does not change in response to the voltage applied to the tube lens. Hence, neutral compounds were not transmitted into the ion optics region.

2.2.1.2   Ionization via atmospheric pressure chemical ionization (APCI)

APCI is thought to be a gas-phase ionization process that effectively ionizes analytes that are thermally stable and range in polarity from nonpolar to semi-polar. A solution containing analyte(s) was first flown through a fused silica transfer capillary kept at a temperature of 250 – 315 °C. In the APCI experiments discussed below, carbon disulfide was used as the solvent as it ionizes aromatic analytes with minimal fragmentation.[19] N_2 sheath and auxillary gases were flown through the probe outside of the heated transfer capillary to converge with the gaseous mixture of solvent (CS_2) and analytes effusing from the heated capillary. The N_2 gas helped transport the gaseous CS_2 solvent and analyte molecules near the Corona discharge needle held at 2.0 – 4.0 kV potential. The Corona discharge needle ionized the ambient N_2 gas to produce primary $N_2^{+\bullet}$ molecular ions. These ions reacted with CS_2 solvent molecules to generate secondary ions ($CS_2^{+\bullet}$) that reacted with the analyte molecules via electron abstraction to generate analyte molecular ions. Molecular ions generated from aromatic analytes using the above approach generally do not

fragment while those generated from aliphatic analytes may.[19] Figures 2.2 and 2.3 illustrate the

ionization process for aromatic compounds by using (+)APCI/N_2 and CS_2 solvent.
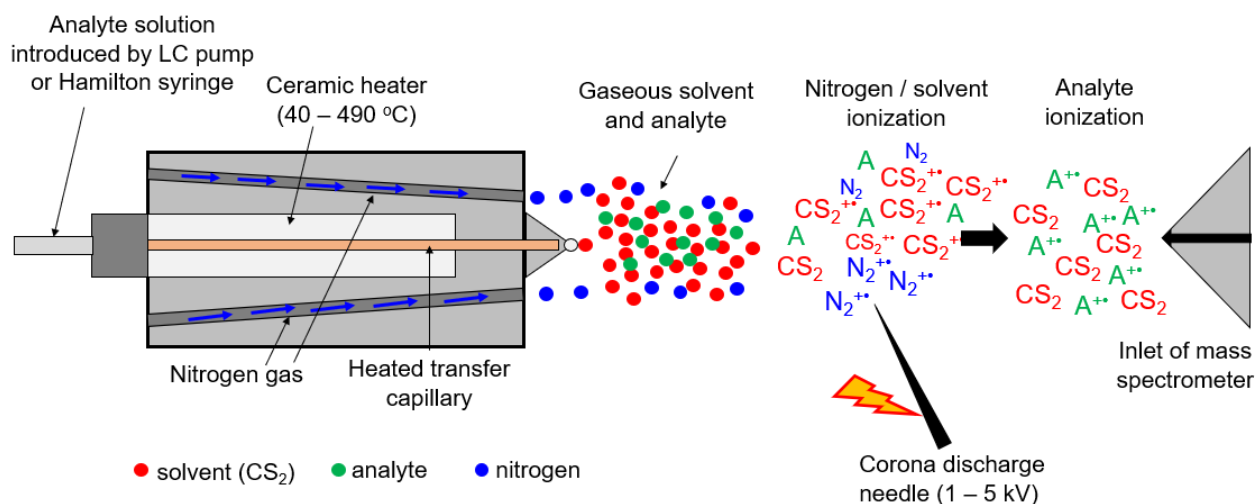
Figure 2.2 A schematic of an APCI source. The CS_2 solvent (red dots) and analyte molecules (green dots, A) are evaporated by the ceramic heater and enter the ion source box via the aperture of the heated transfer capillary. The N_2 molecules (blue dots) facilitate the transport of the CS_2 and analyte molecules near the Corona discharge needle. Ionization occurs via an electron transfer process (please see Figure 2.3 for a description).
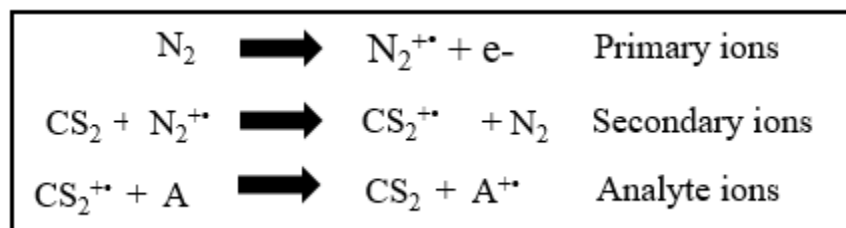
Figure 2.3 The N_2 gas is ionized by the Corona discharge needle to form $N_2^{+\bullet}$ radical cations. The primary $N_2^{+\bullet}$ ions abstract an electron from CS_2 solvent molecules because CS_2 has a lower ionization energy than N_2. $CS_2^{+\bullet}$ ions abstract an electron from analytes (A) when the analytes have lower ionization energies than CS_2. Hence, molecular radical cations are produced from the analytes. As the $CS_2^{+\bullet}$ ions contain no hydrogen atoms, protonation does not occur as a competitive ionization process."

2.2.1.3   Electrospray ionization (ESI)

ESI is effective at ionizing analytes that are polar and thermally labile, such as drug metabolites, peptides and proteins, via acid / base chemistry. The mechanisms associated with ESI are still under debate. In some cases, ionization may occur in solution before the analytes enter the ESI needle. Other analytes may be ionized via one of several possible mechanisms during the ESI process.[20,21] ESI involved passing the analyte solution through the ESI needle and exists as a spray plume (Figure 2.4). A voltage (1 – 5 kV) was applied to the tip of the needle to generate charges on the outer perimeters of the droplets. N_2 gas passed through the ESI probe coaxially to the needle to facilitate solvent evaporation from the droplets. One of the possible mechanisms of ionization is described as follows. As the solvent evaporates from the droplets, the charge density on the surface of the droplet increases until the electrostatic forces exceed the surface tension of the droplet. At this point, the droplet divides into smaller droplets. This process is repeated until the volume of the droplet is so small that the electrostatic repulsion between the ionized analytes results in their ejection from the droplet into the gas phase (see Figure 2.5).
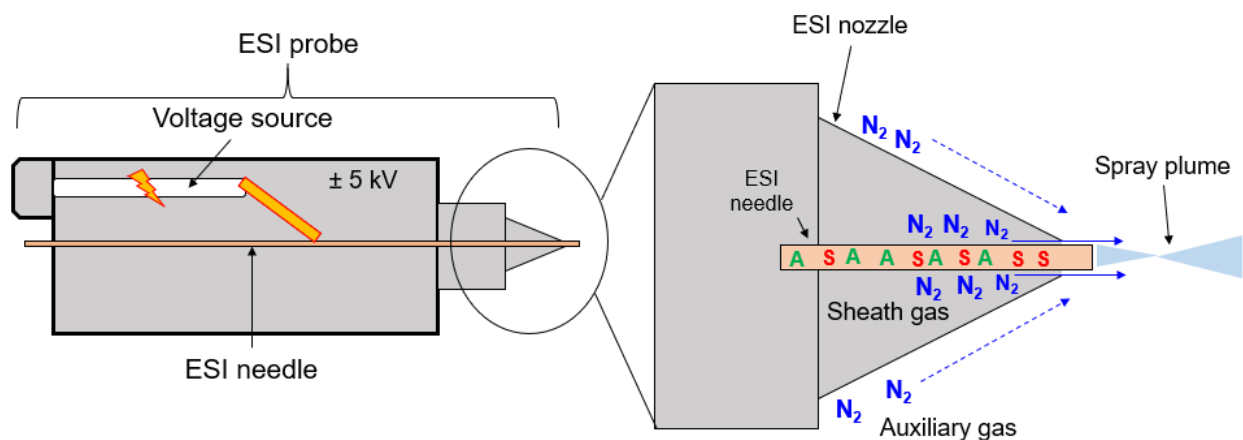
Figure 2.4 A schematic of an ESI probe. Analyte solution passes through the ESI needle. The N_2 sheath gas flows coaxially through the probe alongside the ESI needle. The N_2 auxiliary gas flows alongside the ESI needle and converges at the tip of the probe. The sheath and auxiliary gases generate a spray plume composed of a fine mist of droplets.
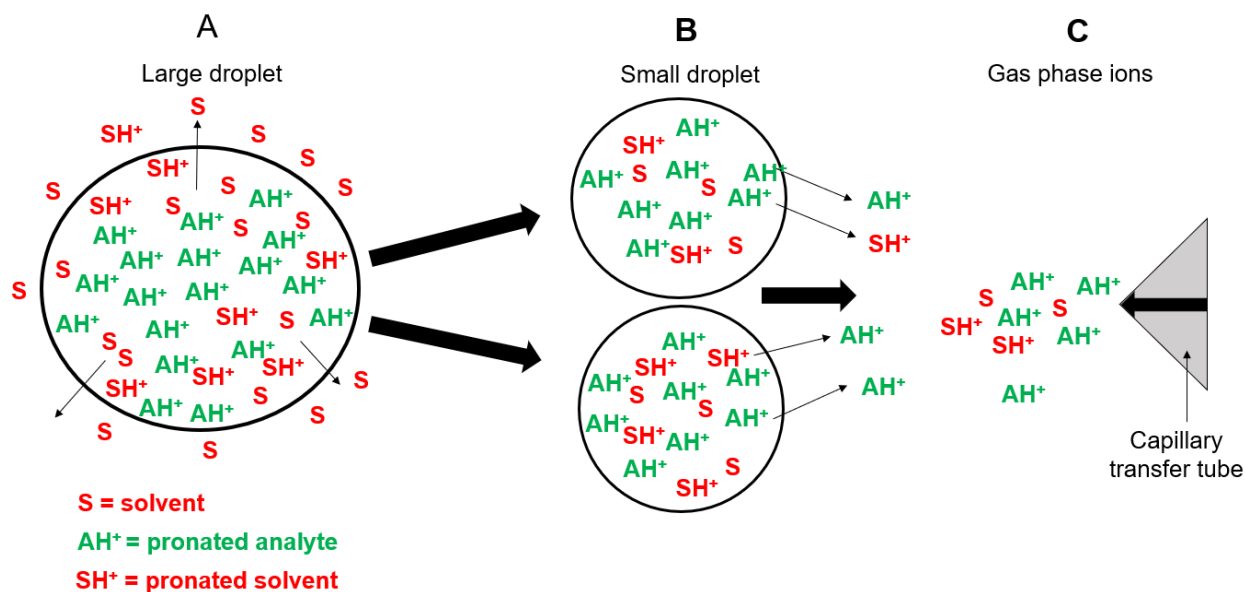
Figure 2.5 One of the possible mechanisms for ESI is shown above. (A) A mist of large droplets exits the ESI probe and the solvent molecules keep evaporating from the droplets. (B) As the droplet decreases in size, the electrostatic repulsions between the ions increase. (C) The electrostatic repulsion between the ions increases until the repulsion force exceeds the surface tension of the droplet, resulting in ion ejection from the droplet into the gas phase.

2.2.1.4 Ion optics region

After ions passed through the API stack (Figure 2.1), they entered the ion optics region and passed through four lenses. A DC voltage was applied to each lens to focus the ions as they entered and exited several ion guides. The four lenses (in sequential order) are referred to as lens 0, lens 1, gate lens and front lens (Figure 2.1). The ion guides (in sequential order) are referred to as MP00, MP0 and MP1 (Figure 2.1). MP00 and MP0 were square quadrupole ion guides and MP1 was a round-rod octupole ion guide. The trajectories of the ions in the multipoles were restricted in the x- and y-directions via RF potentials applied to the electrodes. An RF voltage of the same phase and amplitude was applied to opposing electrodes while the same voltage but 180° out of phase was applied on the adjacent electrodes. The RF voltage oscillated over time from positive to neutral to negative on opposing electrodes and from negative to neutral to positive on adjacent electrodes, analogous to a sine wave (Figure 2.6). The generated RF field induced a corkscrew-like trajectory for the ions.
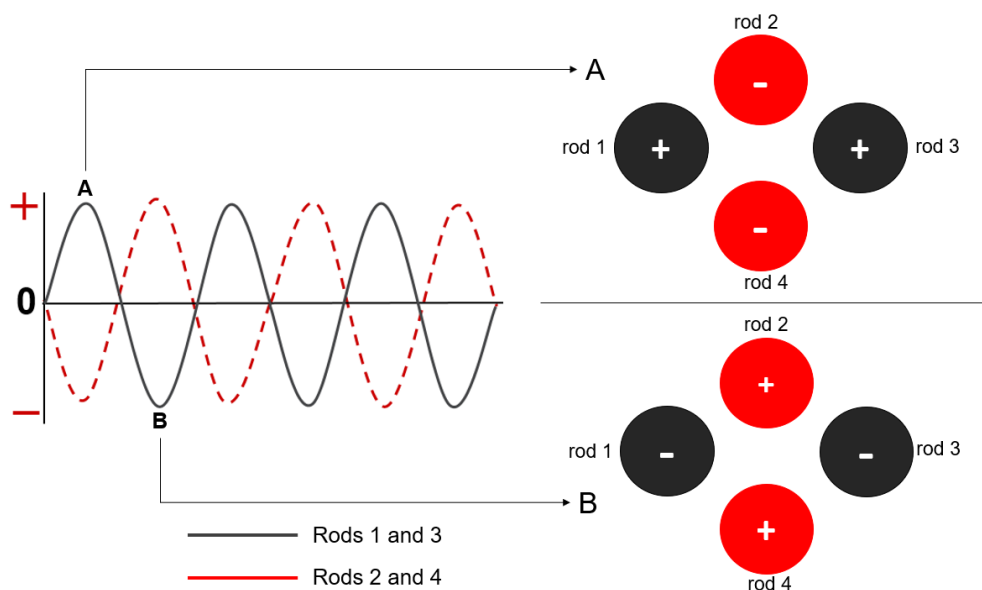
Figure 2.6 (A) A positive RF voltage was applied to electrodes 1 and 3 and a negative RF voltage to electrodes 2 and 4. (B) A negative RF voltage was applied to electrodes 1 and 3 and a positive voltage to electrodes 2 and 4.

To facilitate ion motion in the axial direction and influence the translation energy of the ions, a DC offset voltage was applied on the lenses and ion guides (Figure 2.7). The pressure in multipole MP00 was approximately 0.5 Torr, which reduced the kinetic energy of the ions. A decreasing potential was applied to multipoles MP0 and MP1 and lens 0, lens 1 and the gate lens to increase the kinetic energy of ions and their transmission efficiency into the ion trap.
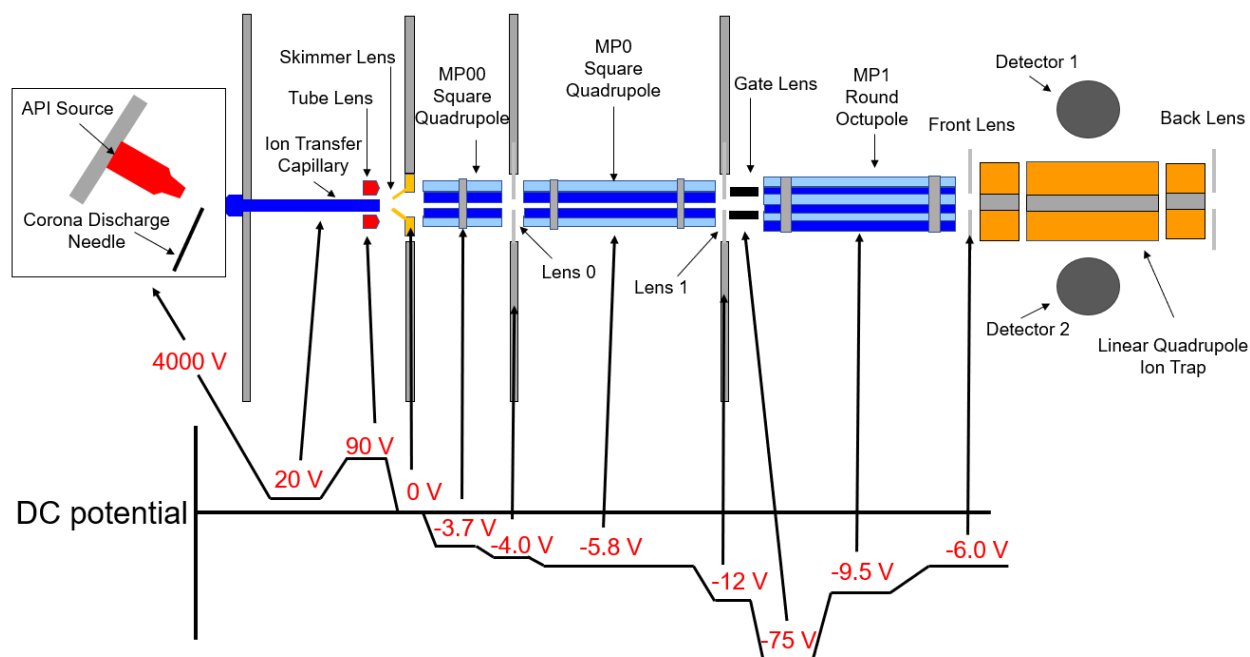
Figure 2.7 A DC voltage gradient facilitated the transmission of ions in the axial direction through the ion optics region.

2.2.1.5 Ion trap region

The ion trap was composed of four hyperbolic electrodes and a front and back lens. The hyperbolic electrodes were split into three parts: the front, center and back part, with lengths of 12 mm, 37 mm and 12 mm, respectively (Figure 2.8). Slits in were in the center x-electrodes in order to enable ions to exit the trap for detection. For a description of ion ejection, please see section 2.2.2.7.
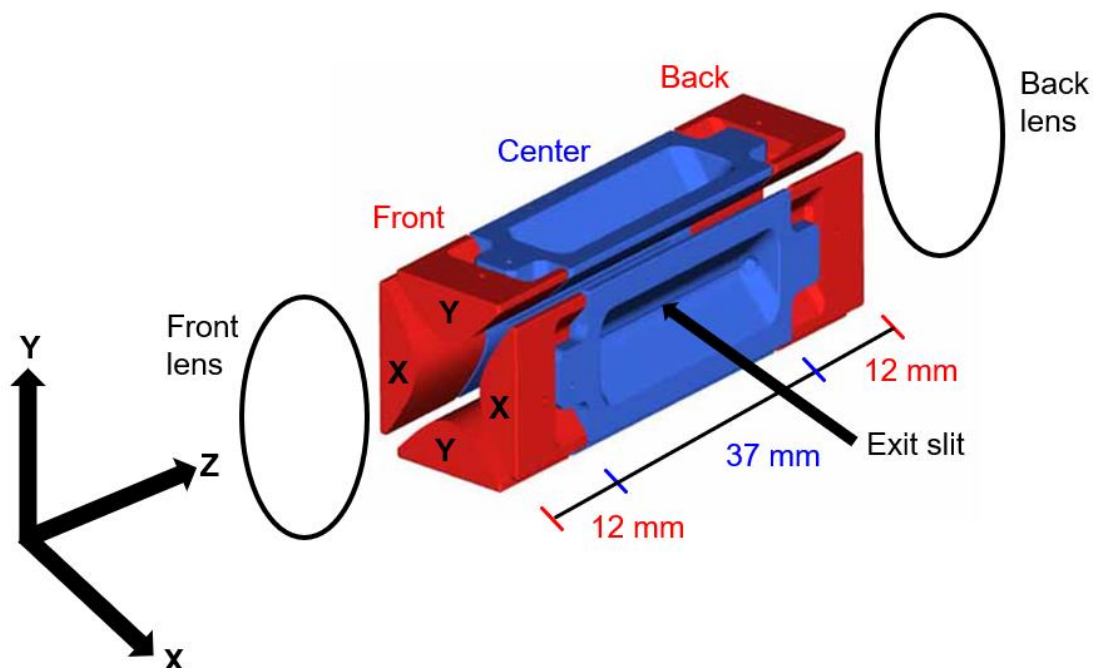
Figure 2.8 A picture of a linear quadrupole ion trap, showing the lengths of the three parts of the four hyperbolic electrodes and the location of an exit slit.

The ions entered the ion trap through the front lens. Two detectors were located perpendicular to the z-axis of the ion trap, each consisting of a conversion dynode and an electron multiplier (Figure 2.9; ejection of the ions into the detectors is discussed later). The conversion dynodes resemble a shallow, concave basin. To attract positive and negative ions ejected from the ion trap, a potential of -15 kV or +15 kV, respectively, was applied to the conversion dynodes. When positive ions struck a negatively charged dynode, electrons and negative ions were released. When negative ions struck a positively charged dynode, positive ions were released. The secondary ions were focused by the concaved surface of the dynode and accelerated into the electron multiplier via an attractive electric field between the dynode and the electron multiplier.
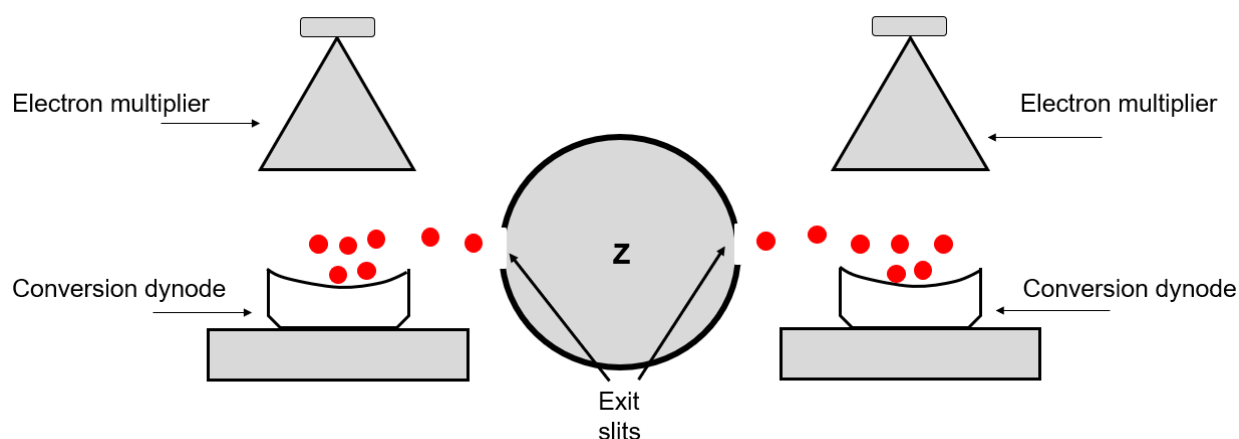
Figure 2.9 Location of the conversion dynode and electron multiplier relative to the exit slits in the x-electrodes of the linear quadrupole ion trap. The red circles represent ions ejected from the ion trap. The schematic is in the direct line-of-sight of the z-axis of the ion trap.

The electron multiplier was composed of a cathode and an anode (Figure 2.10). The cathode was made of lead oxide and resembled an inverted funnel. The anode resembled a small wide basin that connected to the tapered end of the cathode funnel. The secondary ions produced from the dynode struck the cathode releasing electrons. The released electrons struck the cathode again and released more electrons. This process was repeated multiple times, resulting in an electron cascade that generated an electrical current. The current was collected by the anode and was proportional to the number of secondary ions that strike the cathode, which was proportional to the number of ejected ions that struck the conversion dynode. Hence, the current was proportional to the abundance of ions ejected from the ion trap. The ions ejected from the trap were assigned an m/z value based on the RF amplitude during the ejection scan (discussed in detail below).
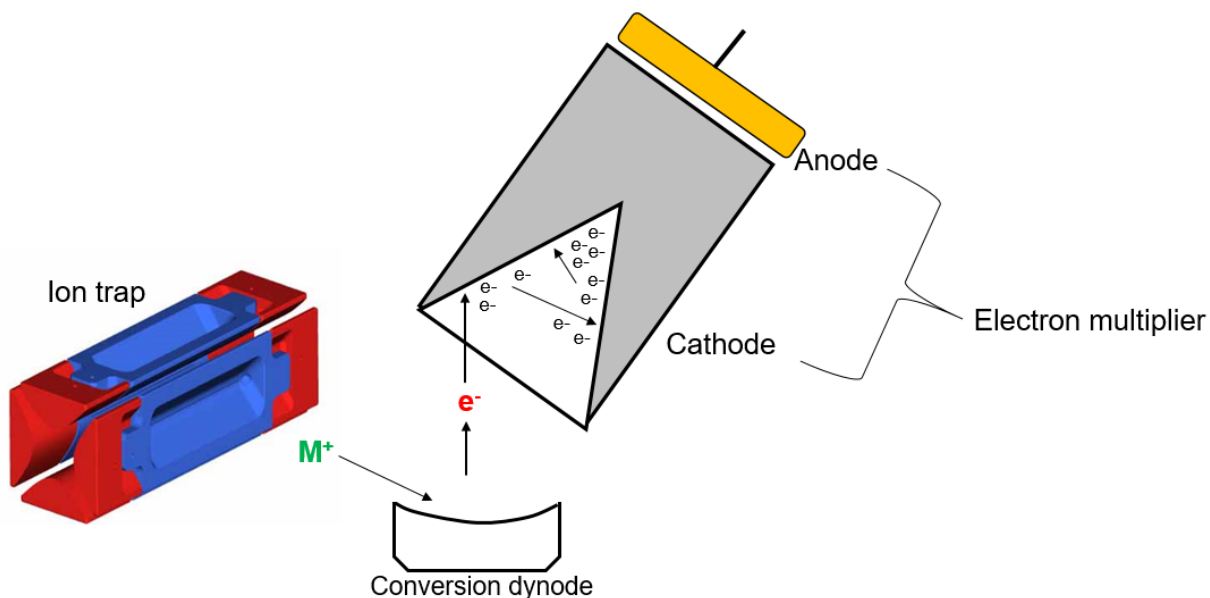
Figure 2.10 The relative locations of the linear quadrupole ion trap, conversion dynode, and electron multiplier. Ions were ejected from the ion trap, struck the conversion dynode and produced electrons that were accelerated to the cathode of the electron multiplier via an attractive electrical potential. Each electron that struck the cathode released additional electrons that continued to strike the cathode to generate a cascade of electrons.

2.2.2. Functions of the linear quadrupole ion trap

A concise description of the four major functions of the ion trap are presented in the following sections, including ion trapping, ion isolation, ion activation and CAD, and ion ejection for detection.

2.2.2.1 Ion trapping

When ions reached the ion trap, DC and RF potentials and helium buffer gas were used to trap the ions. The DC and RF potentials trapped the ions in the axial and radial direction, respectively. The helium buffer gas cooled the ions through low-energy collisions and restricted the ions' motion into the center region of the ion trap. The collisions with helium were not energetic enough to induce dissociation of most trapped ions.

2.2.2.2 Ion trapping in the axial (z) direction

To trap ions axially, DC voltages were applied to the front, center and back parts of the electrodes. When trapping positive ions, positive DC voltages were applied to the rods. The situation was reversed for negative ions. The relative electrical potentials applied to the front and back parts of the electrodes were more repulsive than those applied to the center parts of the electrodes. Hence, ions were trapped axially in a potential well that restricted their movement into the center section of the ion trap (Figure 2.11).
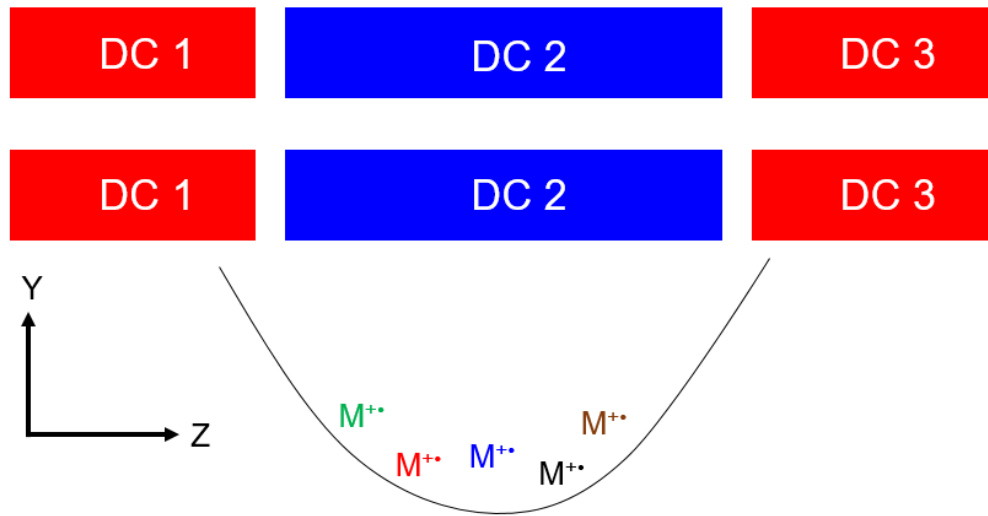
Figure 2.11 Positively charged ions were trapped axially (*i.e.*, in z-direction) by applying greater repulsive DC potentials to the front and back parts of the rods of the ion trap compared to the center parts. Hence, the motion of ions was confined into the center section by an electrical potential well.

2.2.2.3 Ion trapping in the radial (x and y) axis

To trap ions in the radial direction of a quadrupole ion trap, RF and DC potentials were applied to the front, center and back parts of all electrodes to produce a quadrupolar potential [18, 22] (Φ) that can be defined as

$$\Phi = \frac{\Phi_0}{r_o^2} (\lambda x^2 + \sigma y^2 + \gamma z^2) \tag{2.1}$$

where Φ_o is the applied electric potential, λ, σ and γ are weighing constants for the x, y and z coordinates, respectively, and r_o is a constant which is defined distinctly if the quadrupole is a mass filter or an ion trap. Within any electrical field, differential equations defined by Laplace transform must be satisfied.[18] When the Laplace transform is satisfied, the following expression for the weighing constants can be expressed as

$$\lambda + \sigma + \gamma = 0 \tag{2.2}$$

For a linear quadrupole ion trap, the values for λ, σ and γ are as follows: $\lambda = \sigma = 1$ and $\gamma = -2$.[18] When the values for λ, σ and γ are substituted into equation 2.1, the potential at any point inside the quadrupolar field may be defined as [18]

$$\Phi x, y, z = \frac{\Phi_0}{r_o^2} (x^2 + y^2 - 2z^2) \tag{2.3}$$

Equation 2.3 can be changed to polar coordinates by utilizing the standard transformations x = rcosθ, y = rsinθ and z = z. Therefore, equation 2.3 can be expressed as [18]

$$\Phi r, z = \frac{\Phi_0}{r_o^2} (r^2 cos^2\theta + r^2 sin^2\theta - 2z^2) \tag{2.4}$$

By applying the trigonometric identity $cos^2 + sin^2 = 1$, equation 2.4 is defined as [18]

$$\Phi r, z = \frac{\Phi_0}{r_o^2} (r^2 - 2z^2) \tag{2.5}$$

The quadrupolar potential is depended on the RF potential (VcosΩt) and the DC potential (U). Combining the RF and the DC potential, Φ_o is defined as

$$\pm \Phi o = \pm(U - Vcos\Omega t) \tag{2.6}$$

where U is the DC voltage and V is the amplitude of the RF voltage with an angular frequency Ω (expressed in rad • s^{-1}), for time t.

When the applied electric potential (Φ_o) defined by equation 2.6 and $\lambda = 1$ are substituted into equation 1 and Φ_o is differentiated with respect to x, the quadrupole potential becomes [18]

$$\frac{\delta\emptyset}{\delta x} = \frac{2x}{r_o^2}(U + Vcos\Omega t) \tag{2.7}$$

The force experienced by an ion with a mass m and a charge z in the x- and y-directions within a quadrupolar field is expressed as

$$Fx = m\frac{d^2x}{dt^2} = -ze\frac{d\phi}{dx} \tag{2.8}$$

$$Fy = m\frac{d^2y}{dt^2} = -ze\frac{d\phi}{dy} \tag{2.9}$$

where e is the elementary charge, 1.602 x 10^{-19} Coulombs.

When equation 2.7 is substituted into equation 2.8, the force of the ion in the x-direction is defined as [23, 24]

$$\frac{d^2x}{dt^2} = \frac{-2ze}{mr_o^2}(U + Vcos\Omega t)x = 0 \tag{2.10}$$

Similarly, the force of the ion in the y-direction is defined as [23, 24]

$$\frac{d^2y}{dt^2} = \frac{-2ze}{mr_o^2}(U + Vcos\Omega t)y = 0 \tag{2.11}$$

Equations 2.10 and 2.11 define ion motion in the quadruple ion trap and can be used to determine the stability of ion trajectories in a linear quadrupole ion trap. Equations 2.10 and 2.11 resemble the Mathieu equation provided below:

$$\frac{d^2u}{d\xi^2} + (a_u + 2q_u cos2\xi)u = 0 \tag{2.12}$$

where the parameter ξ is defined as:

$$\xi = \frac{\Omega t}{2} \tag{2.13}$$

When equation 2.13 is substituted into equations 2.10 and 2.11, equations 2.10 and 2.11 can be expressed as Mathieu equations [22, 23]

$$q_u = q_x = (-)q_y = \frac{4zeV}{mr_o^2\Omega^2} \tag{2.14}$$

$$a_u = a_x = (-)a_y = \frac{8zeU}{mr_o^2\Omega^2} \tag{2.15}$$

where q_u and a_u are defined as the Mathieu stability parameters. The parameters describe the motion of ions and the overall stability of the ion motion inside the linear quadrupole ion trap. Based on equations 2.14 and 2.15, the mass of the ions is inversely related to the q_u and a_u parameters.

Ions with stable trajectories in the ion trap have q_u and a_u values that fall within the coordinates of the Mathieu stability diagram (Figure 2.12). For example, the box labeled as A in Figure 2.12 corresponds to an ion whose q_u and a_u values are approximately 0.72 and 0.10, respectively. The parameters indicate that the ion has a stable trajectory in the ion trap. However, the box labeled B represents a different ion that does not have a stable trajectory in the x-direction because the a_u parameter is too negative. This unstable trajectory means that this ion cannot be trapped under these conditions.

When the a_u parameter is set to 0, the range of q_u is at its maximum within the Mathieu stability diagram. Therefore, setting a_u to 0 enables the trapping of ions with the largest possible mass range. When a_u is set to 0, the motions of the ions in the trap are manipulated by altering the main RF potential amplitude. As the amplitude increases, the ion q_u values increase. When the q_u parameter of a given ion equals 0.908, the trajectories of this ion become unstable in the x- and y-directions, resulting in ion ejection. Since q_u and the mass of ions are inversely related, the first ions ejected from the trap have the lowest m/z values.
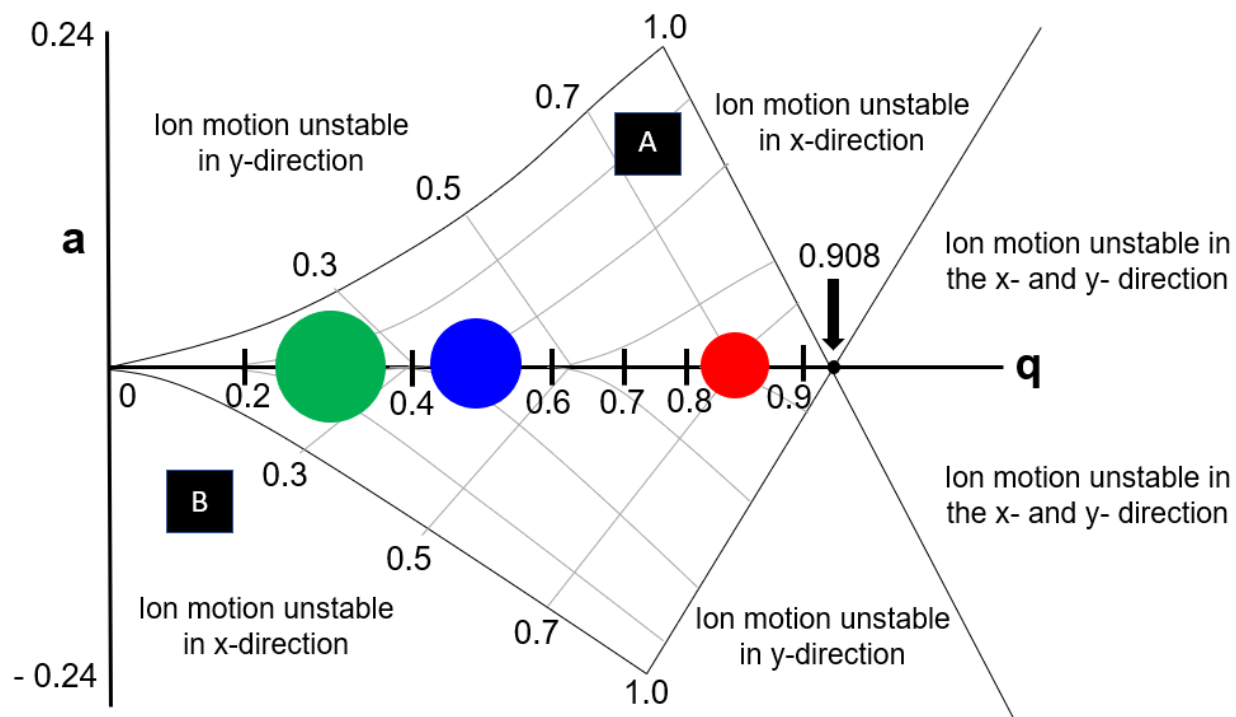
Figure 2.12 Mathieu stability diagram. The green, blue and red circles represent three different ions in the ion trap, with the smallest circle representing the smallest ion. As the RF potential amplitude is increased, the q parameter for the ions increases. The smallest ion (red circle) reaches a q value of 0.908 first and is ejected from the ion trap, followed by the medium-sized ion (blue circle) and then by the largest ion (green circle).

2.2.2.4 The role of helium buffer gas

When ions undergo frictional collisions with helium buffer gas inside the ion trap, they are kinetically cooled and located into the center of the trap. This increases their trapping and detection efficiencies, thus improving sensitivity. [25] The cooled ions do not gain enough internal energy to dissociate.

2.2.2.5 Ion isolation

To perform tandem mass spectrometry experiments, ions of a chosen m/z value must be isolated by ejecting all other ions from the ion trap. Since ions of a specific m/z value oscillate at

a unique frequency, tailored RF waveforms can be used to eject unwanted ions from the trap. Before these isolation waveforms were applied, the RF voltage was increased until the ions of interest had a q_u value of 0.83. Ions with lower m/z values were ejected because their q_u values are greater than 0.83. (Figure 2.13). Next, dipolar excitation was applied to the x-electrodes at frequencies from 5 up to 500 kHz with exception of the frequency corresponding to the ion with $q_u = 0.83$ (Figure 2.14).
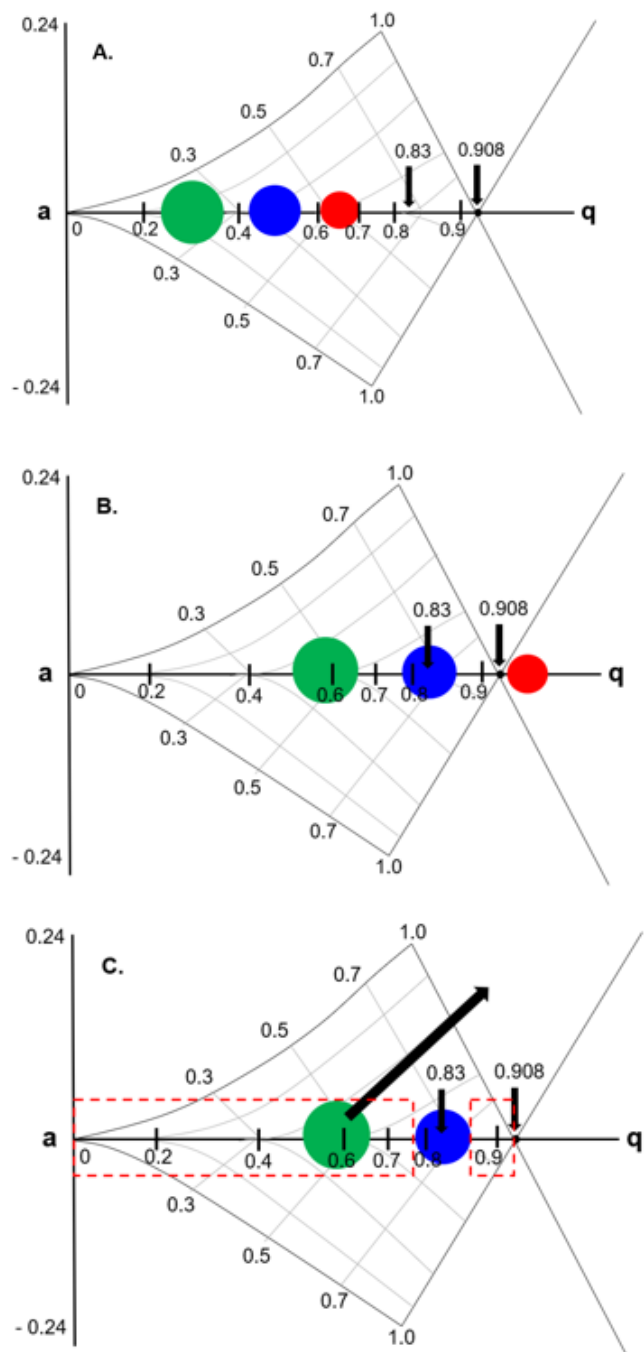
Figure 2.13 (A) Mathieu stability diagram showing ions of different m/z values (represented with different sized and colored circles) with stable trajectories. (B) The RF amplitude is increased until the ion of interest (indicated using a blue circle) obtains a q value of 0.83. The smallest ion (*i.e.*, red circle) is ejected from the ion trap. (C) A tailored RF waveform is applied to the x-rods at all frequencies except for the secular frequency of the motion of the ions of interest located at q = 0.83 (*i.e.*, blue circle). The black arrow drawn from the green circle denotes an unstable trajectory for the ion when the tailored RF waveform is applied. This process results in isolation of the desired ion (blue circle).
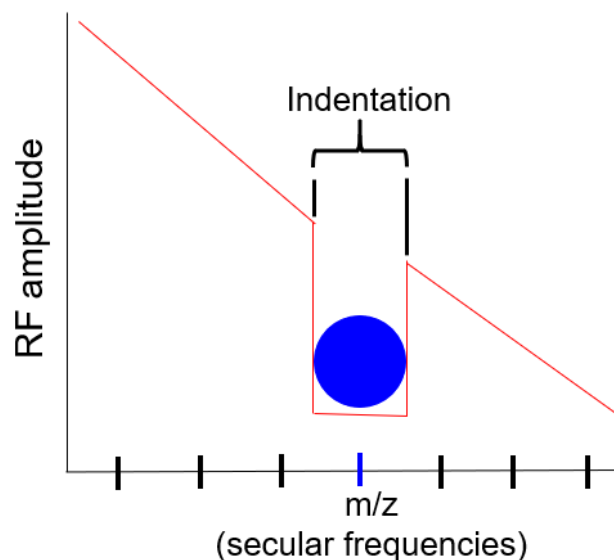
Figure 2.14 A tailored excitation waveform containing frequencies that result in ejection of ions other than the ion of interest. An indentation is present in the waveform whose width is equal to the isolation window set by the user. The secular frequency of the ion of interest is not included in the tailored RF waveform.

2.2.2.6 Ion activation for CAD

After ions are isolated in the ion trap, they can be subjected to collision-activated dissociation (CAD). CAD in an ion trap is a slow heating method that facilitates fragmentation of ions via low-energy pathways.[14] In order to achieve this, the RF amplitude of the main RF-field was reduced until the isolated ions reached a user-specified q value (usually 0.25). After this, the ions were accelerated via dipolar excitation by applying a supplementary RF potential to the x-electrodes that had a frequency equal to the secular frequency of the isolated ions. The accelerated ions underwent multiple low-energy collisions with helium buffer gas for a selected period of time, typically 30 ms. If the internal energy deposited into the ions upon the activating collisions exceeded a dissociation energy threshold, the ions underwent fragmentation via that dissociation pathway.

2.2.2.7 Ion ejection for detection

Ions must be ejected from the ion trap into the external detection system for detection. This process was facilitated by resonance ejection. Unlike ion isolation, x-electrode dipolar resonance ejection was employed to systematically eject ions. This ejection technique increases resolution and sensitivity. [26, 27]

Resonance ejection involves dipolar excitation of ions when q equals 0.88. To complete resonance ejection, a supplementary RF voltage was applied to the x-electrodes (Figure 2.15). As the main RF voltage was ramped, the q value for the ions increased until it reached 0.88. At this point, the secular frequency of the ions was in resonance with the supplemental RF voltage. The ions gained kinetic energy and began to oscillate. The ions were eventually ejected as a tight packet through the slits of the x-rods of the ion trap, struck the conversion dynode, and were detected as described in section 2.2.1.5.
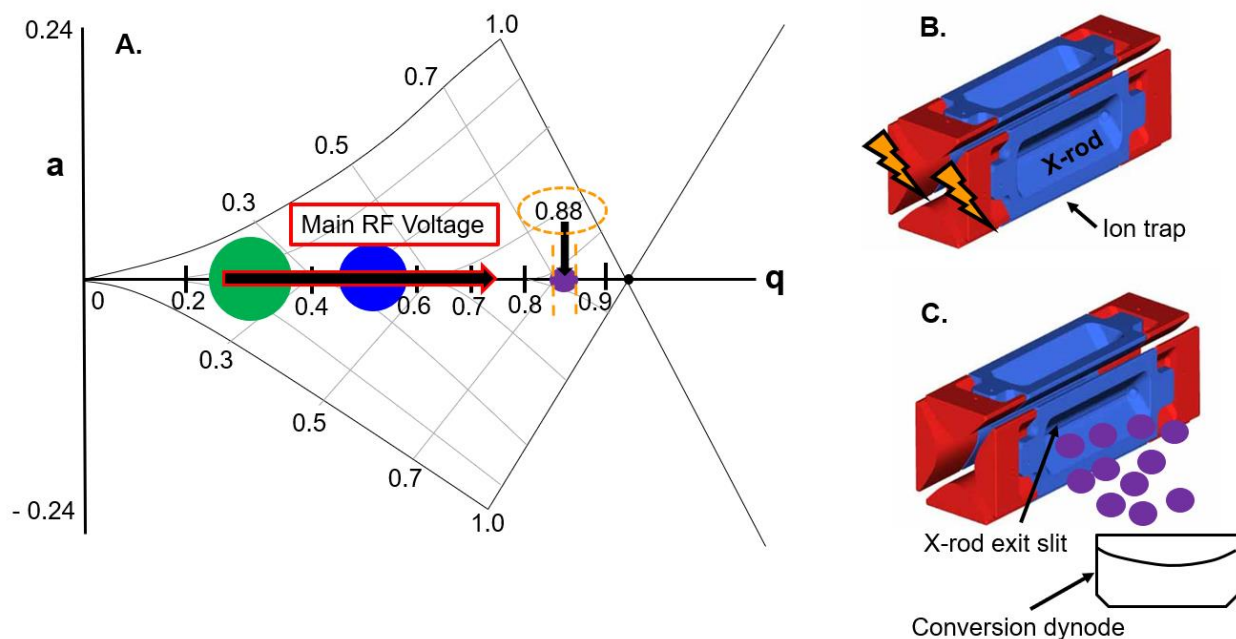
Figure 2.15 (A) As the main RF amplitude increases, the q values of the ions also increase. (B) When the q value of the smallest ion (smallest and purple circle) reaches 0.88, a supplementary RF voltage is applied to the x-electrodes. The frequency of motion of the ions whose q value is 0.88 will be in resonance with the frequency of the supplementary RF voltage applied to the x-electrodes (C) These ions (purple circles) gain kinetic energy, move away from the center of the ion trap, exit via slits in the x-electrodes and strike the conversion dynode. For clarity, ions are ejected from only one exit slit.

2.3 Orbitrap mass spectrometer

The orbitrap was first introduced as a mass analyzer in 2000 by Makarov.[28] Unlike many mass spectrometers that use RF or magnetic fields to separate ions, the orbitrap uses only a DC field.[28] The ions are dynamically trapped inside the orbitrap by using this field and detected as discussed below. Dynamic trapping of ions can be accomplished in one of three ways: linear trapping, segmented ring trapping and orbital trapping.[28] Orbital trapping of ions has been used previously in spectroscopy experiments.[29-32] This approach was also employed in the orbitrap mass spectrometer employed in this research. The original design was developed by Kingdon in 1923 and is often referred to as a Kingdon trap.[33] At its simplest, the Kingdon trap has a wire stretched

along the axis of an outer cylinder that contains flanges to close off a trapping volume.[28] When a voltage is applied between the cylinder and the metal wire, a strong field attracts the ions toward the wire.[28] Ions with a large enough tangential velocity will be trapped because they orbit around the wire but cannot collide with it.[28] A schematic of an LQIT coupled to an orbitrap is shown in Figure 2.16.
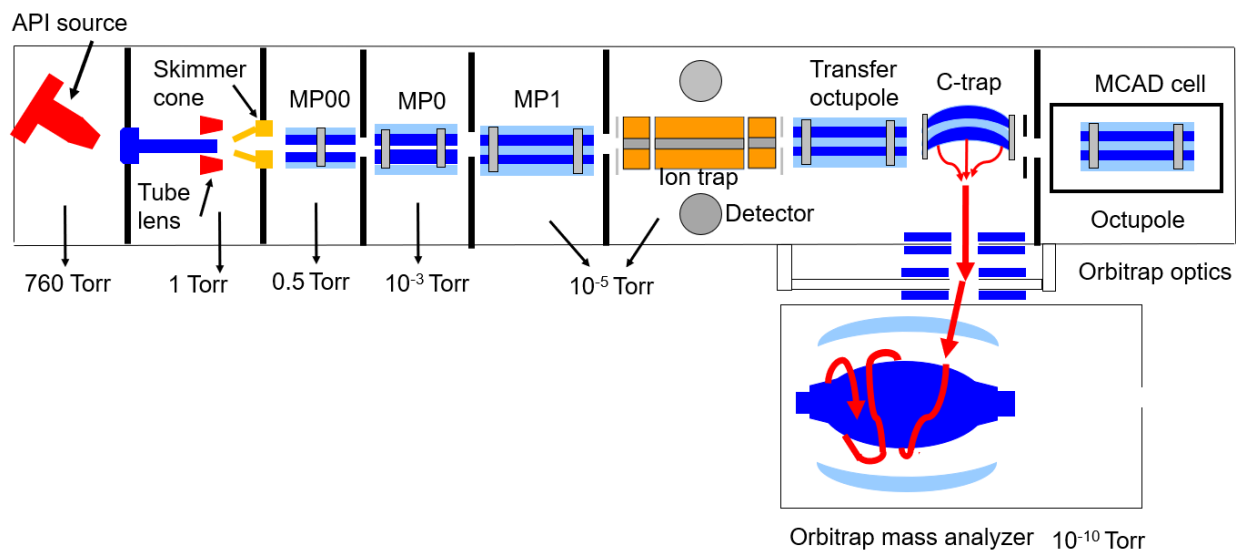
Figure 2.16 Schematic of an LQIT coupled to an orbitrap mass spectrometer. The pressures in different areas are indicated. The red arrows represent the injection of a tight packet of ions from the C-trap into the orbitrap.

2.3.1 Ion trajectories in the orbitrap

The orbitrap employed in this research was composed of two electrodes: a central electrode resembling a spindle and an outer electrode that looks like a barrel. When a DC voltage was applied between the electrodes, a three-dimensional electrostatic field defined below was created. [28, 34,35]

$$U(r,z) = \frac{k}{2}\left(z^2 - \frac{r^2}{2}\right) + \frac{k}{2}(R_m)^2 \ln\left[\frac{r}{R_m}\right] + C \tag{2.16}$$

where r represents the angular coordinate, z represents the axial coordinate, k is a constant related to the field curvature, R_m is a characteristic radius, and C is a constant. [34,35] The geometric shape of the electrodes can be derived from equation 2.16 and is expressed as [36]

$$z_{1,2}(r) = [\frac{r^2}{2} - \frac{(R_{1,2}^2)}{2} + (R_m)^2 \ln(\frac{R_{1,2}}{r})]^{1/2} \tag{2.17}$$

where z is the plane of symmetry, and R_1 and R_2 are the maximum radii of the central and outer electrodes, respectively. [36]

For ions to be trapped in the orbitrap, their trajectories must be stable around the central electrode Ions with stable trajectories field have three motions, each with a unique frequency: radial oscillations (frequency ω_r), rotational oscillations around the central electrode (frequency ω_φ) and axial oscillations along the z-axis (frequency ω_z). The motion of ions (with a mass-to-charge ratio = m/q) along the polar coordinates (r, φ and z) is defined by the following equations

$$\frac{\partial^2 r}{\partial t^2} - \left(\frac{\partial \varphi}{\partial t}\right)^2 = -\frac{q}{m}\frac{k}{2}\left[\frac{R_m^2}{r} - r\right] \tag{2.18}$$

$$\frac{d}{dt}\left[r^2 \frac{\partial \varphi}{\partial t}\right] = 0 \tag{2.19}$$

$$\frac{\partial^2 z}{\partial t^2} = -\frac{q}{m} kz \tag{2.20}$$

Of the three unique frequencies, only the axial frequency is used for ion detection because it is independent of the position and energy of the ion. Hence, the axial frequency is used to determine the m/q value of the ion. The axial frequency of oscillation for an ion is provided below

$$\omega = \sqrt{\left(\frac{q}{m}\right)k} \tag{2.22}$$

where q and m are the charge and mass of the ion, respectively, and k is a constant proportional to the voltage applied between the inner and outer electrodes.

2.3.2 Transferring ions into the orbitrap

Ions were transferred into the orbitrap via the quadrupole ion trap, a transfer octupole and a C-shaped–RF only quadrupole called the C-trap (see Figure 2.16).[37] The C-trap was filled with N_2 gas at approximately 1 mTorr. N_2 gas was used instead of He gas because it is more effective at collisional cooling of ions.[37] After collisional cooling, the ions were axially compressed by electrostatic fields into the center of the C-trap, which facilitated their ejection into the orbitrap as a tight ion packet.[37] The ion packet passed through ion optics where it was accelerated to high kinetic energies and injected into the orbitrap in less than one ms. Carryover of N_2 from the C-trap was prevented from reaching the orbitrap by using an electrostatic deflector.[38] The injected ions were trapped in the orbitrap as described above .[28,40, 41]

2.3.3 Detecting ions in the orbitrap

Ions with the same m/z ratio move very fast and coherently as a packet in the orbitrap. The outer electrode was used to measure the image current caused by the axial oscillations of the ion packets (Figure 2.17). [37, 40] After amplification, fast Fourier transformation (FFT) was used to convert the image current into a frequency spectrum. The frequency spectrum was then converted to a mass spectrum by using a two-point calibration.[37]
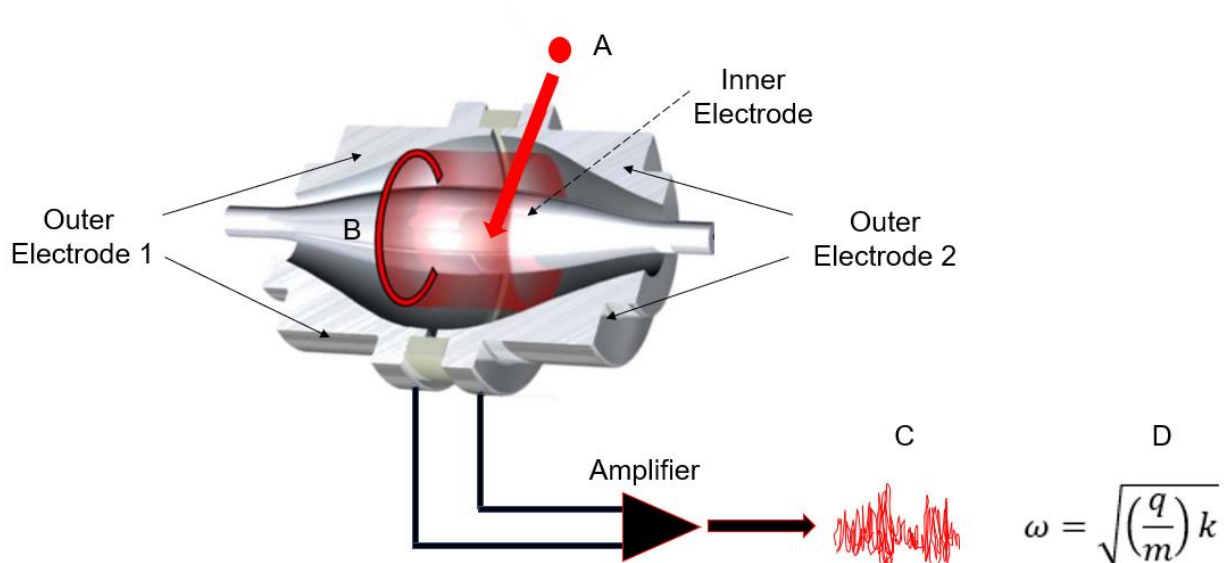
Figure 2.17 (A) Ions enter the orbitrap slightly off axis. (B) In the orbitrap, the electric field induces ions to oscillate around and along the inner electrode so that ions of the same m/z-value move in tight packets (illustrated as thin rings). (C) The outer electrode measures an image current for the motion of the ion packets along the inner electrode. (D) The frequency of the harmonic oscillations is proportional to the m/z value of the ions.

2.3.4 Medium-energy collision-activated dissociation (MCAD)

The LTQ Orbitrap XL mass spectrometer employed here was equipped with an octupole collision cell (referred to by Thermo as an HCD cell) filled with nitrogen gas at a nominal pressure of 3.8 mTorr.[40] CAD experiments carried out in this octupole collision cell haveThis technique has been referred to as "higher-energy C-trap dissociation" or "higher-energy collision-activated dissociation" (HCD).[41,42] However, according to IUPAC recommendations, the term high-energy collision-activated dissociation is designated for an ion with a laboratory-frame translational energy greater than 1 keV.[43] Therefore, the use of the term "higher-energy" for this dissociation technique is not appropriate. Further, the use of the term "higher" is uncertain as this activation method is not directly compared to another activation method. To avoid ambiguity, our group has started referring to this beam-type technique as medium-energy collision-activated dissociation

(MCAD) because the activation method may impart greater internal energy into ions than CAD in an ion trap but less than high-energy activation methods (*i.e.,* keV CAD).

Ions were subjected to MCAD in above octupole collision cell (referred here to as MCAD cell) as follows. The ions of interest were isolated in the linear quadrupole ion trap and transferred through the transfer octupole into the C-trap. Next, the electrical offset between the C-trap and the octupole collision cell was changed to accelerate the ions into the collision cell where they underwent collisions with N_2 gas (Figure 2.18). This mode of CAD is analogous to beam-type CAD performed in quadrupole instruments. The front of the octupole collision cell was equipped with a lens that facilitated ion ejection into and out of the collision cell.
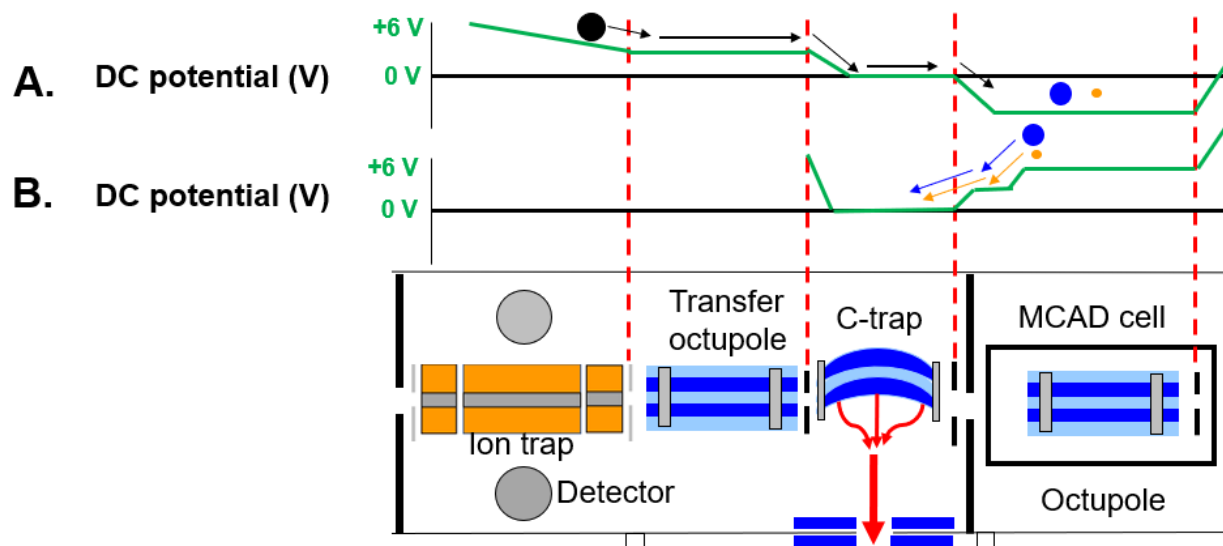
Figure 2.18 (A) DC offset potentials applied between the C-trap and the MCAD cell to induce fragmentation of positive ions. (B) Typical offset potentials applied to eject ions from the MCAD cell back into the C-trap. The ions are then transferred into the orbitrap mass spectrometer. Ions cannot be transmitted back into the linear quadrupole ion trap. For clarity, only transfer of ions from the linear quadrupole ion trap via the C trap into the MCAD cell and then back into the C-trap is illustrated. The black circle represents a positively charged fragmenting ion, and the blue and orange circles represent positively charged fragment ions.

2.4 Two-dimensional gas chromatograph/electron ionization high-resolution time-of-flight mass spectrometer (GCxGC/(EI)TOF MS)

Two-dimensional gas chromatography (GCxGC) is a powerful analytical technique for the separation of volatile complex mixtures into individual components. Compared to 1D GC, GCxGC has a substantially greater resolving power.[44]

In this research, an Agilent 7890A GCxGC system coupled to a Pegasus-HRT 4D electron ionization (EI) high-resolution time-of-flight (TOF) mass spectrometer (GCxGC/(EI) TOF MS) was used to determine the chemical compositions of aviation fuels, potential aviation fuels, alternative aviation fuels and fuel blending components. A schematic for the GCxGC/(EI)TOF MS is shown in Figure 2.19. The samples were injected into the GCxGC with an auto injector (Agilent G4513A). The columns employed were a 60 m polar primary column (Rxi-17Sil ms, Restek, Bellefonte, PA) located in the primary oven and a 2 m nonpolar secondary column (Rxi-1 ms, Restek, Bellefonte, PA) located in the secondary oven. This GCxGC system was equipped with a quad-jet dual stage modulator (see section 2.4.1.2. for a detailed description of the modulator). Eluates from the secondary column were ionized by using positive ion mode EI at 70 eV electron kinetic energy. The ions were analyzed by using a high-resolution folded-flight-path TOF mass spectrometer with a resolution of up to 50,000. Measured values include the analyte elution times in both columns, peak areas, accurate m/z values of the analyte molecular ions and their fragment ions, and a list of possible chemical formulas and structures based on comparison of the measured EI mass spectra to those in EI mass spectral libraries.
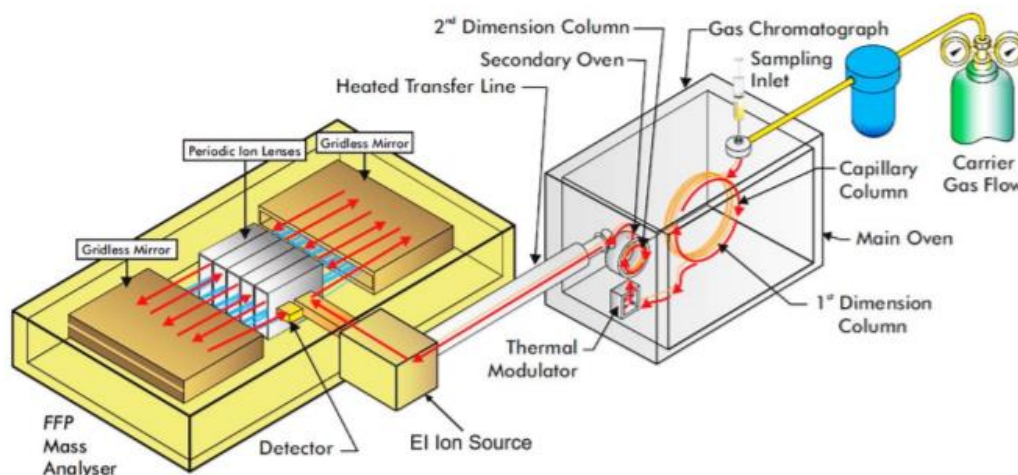
Figure 2.19 A schematic of the GCxGC/(EI)TOF MS instrument. The folded-flight-path of ions in the mass spectrometer is abbreviated as FFP. Each part of the instrument is described in the sections below.

2.4.1 2-Dimensional gas chromatography

The GCxGC system consisted of an auto injector, a primary oven that housed the primary column, a secondary oven that housed the secondary column and a modulator that united the primary and secondary columns (Figure 2.20). The secondary oven was located in an enclosed region separated from the primary oven to enable the use of different temperatures in the ovens (Figure 2.20).

Depending on the components in the mixture of interest, the columns can be used in normal or reversed phase configuration. In normal phase, the first column is nonpolar and the second column is polar. The normal phase column configuration enhances the separation of aromatic compounds from each other in jet fuel[45] and heavy polycyclic cycloalkanes from polycyclic aromatic compounds in oil samples.[46] The reversed phase column configuration has first a polar column and then a nonpolar column. This set-up is suitable for separating light saturated branched alkanes and cycloalkanes from each other in crude oil[46] and in petroleum-derived fuels and fuel blending components.[45,47-49]

At the heart of 2D GCxGC is the modulator.[50] The modulator performs three vital functions: periodic sampling of eluates from the primary column, trapping the eluates inside the modulator by cryo-focusing and injecting the eluates into the secondary column.[50] A critical function of the modulator is preserving the separation of the eluates obtained from the primary column before transfer into the secondary column.

Over the past 30 years, many types of modulators have been developed, including two-stage thermal desorption modulators,[51] rotating thermal modulators,[52] diaphragm valve modulators,[53] differential flow modulators,[54] flow-switching modulators,[55] and Wang's differential flow modulators.[56] The modulator in the GCxGC system used here was a quad-jet dual stage thermal modulator (Figure 2.21). Two separated stages are present in this modulator, each with a cold and a hot jet. For a description of how modulation works, please see Figure 2.22.
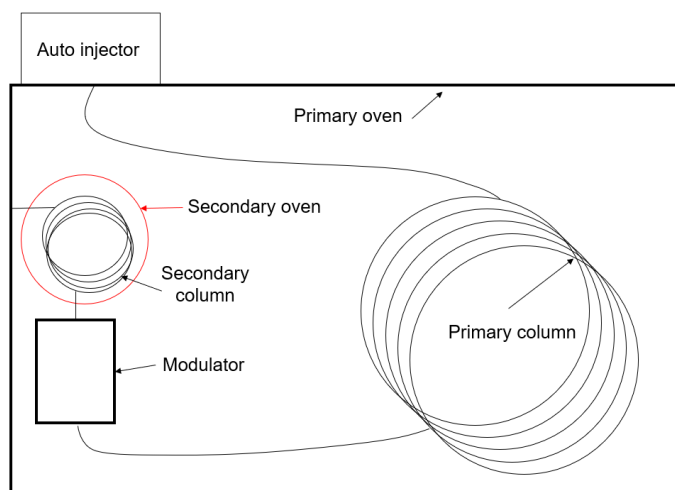
Figure 2.20 Main components of the GCxGC system in the GCxGC/(EI)TOF MS instrument used in this research. The primary column is enclosed in a primary oven and the secondary column is enclosed in a secondary oven.
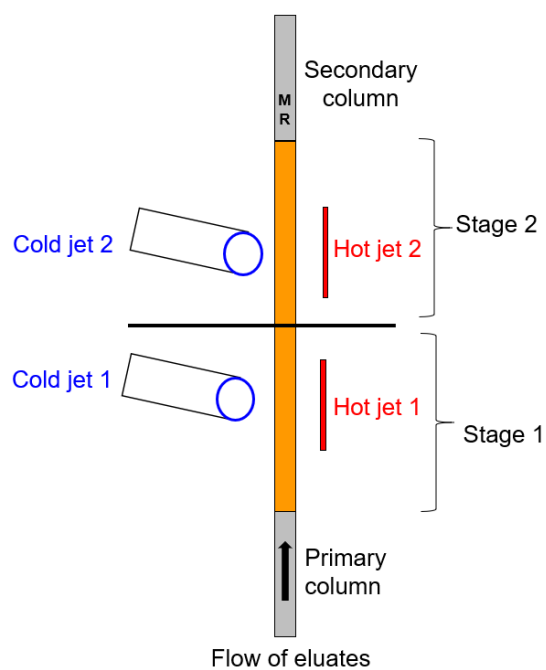
Figure 2.21 A pictorial representation of the quad-jet dual stage modulator.
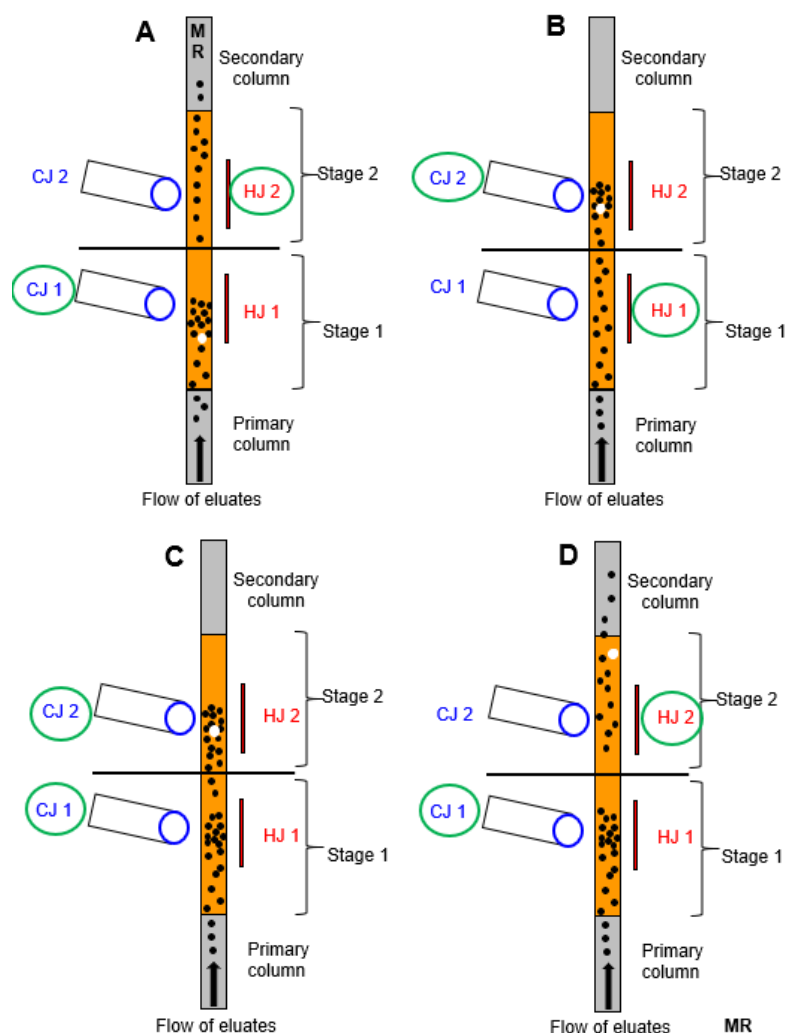
Figure 2.22 A modulation period is composed of four steps as indicated above. A-D: A white circle represents an eluate that can be used as a reference point for the four individual steps. The green circles indicate which cold jet (*e.g.,* CJ) or hot jet (*e.g.,* HJ) is open during each of the four steps. (**A**) In the first step, cold jet 1 is open, allowing chilled nitrogen gas to cryo-focus eluates into the first stage of the modulator. Hot jet 2 is open, allowing hot nitrogen gas to desorb any cryo-focused eluates from the second stage of the modulator. (**B**) In the second step, hot jet 1 is open, allowing hot nitrogen gas to desorb eluates in the first stage of the modulator. Cold jet 2 is open, allowing cold nitrogen gas to cryo-focus eluates in the second stage of the modulator. (**C**) In the third step, both cold jets 1 and 2 are open, allowing cold nitrogen gas to cryo-focus eluates in the first and second stages of the modulator. (**D**) In the final step, cold jet 1 is open, allowing nitrogen gas to continue cryo-focusing of the eluates in the first stage of the modulator. Hot jet 2 is open, allowing hot nitrogen gas to desorb eluates from the second stage of the modulator. In the final stage, the white circle (eluate reference point) desorbs from stage 2 of the modulator and enters the secondary column.

2.4.2 Method development for GCxGC

To separate compounds in complex mixtures by using a GCxGC system, several parameters may be adjusted to enhance the separation which include the modulation period, secondary oven offset temperature, temperature ramping rate, modulator offset temperature and hot and cold jet pulse time during the modulation period. These parameters are discussed below.

2.4.2.1 Modulation period

One complete modulation period must be sufficiently long for all eluates from the primary column to enter the modulator and then be injected into the secondary column before the second set of eluates emerge from the primary column. The modulation period is separated into two stages (Figure 2.23). If the modulator period is too short, wrap-around may occur. Wrap-around is a phenomenon when the retention time in the secondary column of an eluate is greater than the modulation period. In thid case, the compounds may coelute with other compounds emerging from the next modulation period.

If the modulation period is too long, the separation of compounds in the primary column may be lost and the secondary column may be overloaded, decreasing the peak capacity of the column. The peak capacity refers to the maximum number of analytes that can be separated with a column.[57]
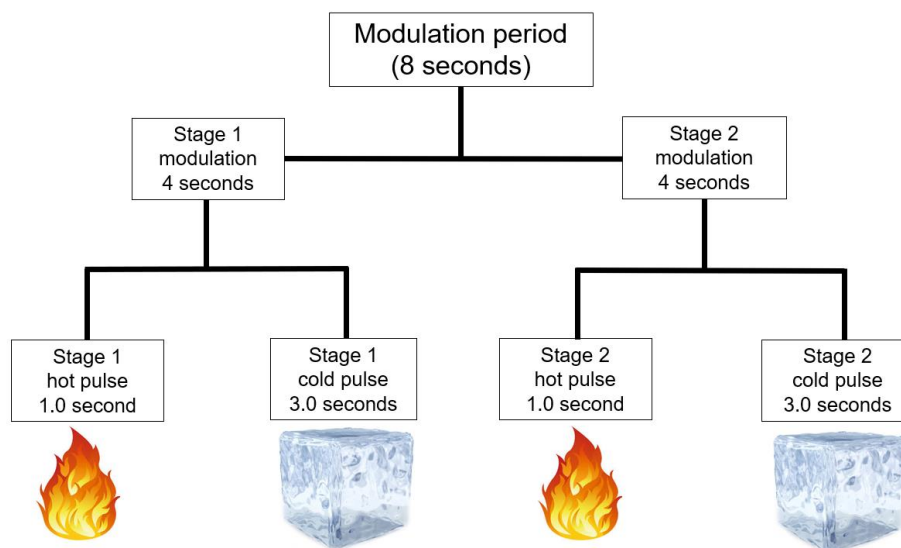
Figure 2.23 An example of a modulation period of 8 seconds that was split between two stages, 4 seconds each, each with hot and cold pulse of 1 and 3 seconds, respectively.

2.4.2.2 Secondary oven offset temperature

The secondary oven offset temperature is the temperature difference between the primary and secondary ovens. As the offset temperature increases, the eluates travel through the secondary column faster, which decreases both the retention time and the resolution of the secondary column. However, increasing the secondary oven offset temperature may be necessary if analytes are strongly retained in the secondary column, in order to prevent wrap-around of the analytes.

2.4.2.3 Temperature ramp rate

The temperature ramp rate is the rate of temperature change (^{o}C/min) for the primary and secondary ovens and the modulator. As the ramp rate increases, the analytes pass through the columns and modulator faster. Hence, the retention times of an analytes decrease as the ramp rate increases. Although the total separation time of the GCxGC decreases as the ramp rate increases,

the chromatographic separation of analytes in both dimensions decreases and coelution of analytes may occur.

2.4.2.4 Modulator offset temperature

The modulator offset temperature is the difference in temperature between the secondary oven and the modulator. The temperature of the modulator influences the temperature of the N_2 gas expelled from the hot jets in the modulator. A greater temperature difference between the secondary oven and the modulator results in a sharper peak for the analyte in the GCxGC chromatogram. Therefore, a large modulator offset temperature is highly recommended, provided that it does not surpass the maximum operational temperature of the column in the modulator.

2.4.2.5 Hot and cold jet pulse times during modulation

The hot and cold jet pulse times refer to how long the jets of hot and cold N_2 gas are expelled in the first and second stages in the modulator. Volatile analytes are cryo-focused when the cold jet is on and desorb when the hot jet is on. As the hot jet pulse time increases, the peak sharpness and resolution increases in the secondary column. If the hot jet is on too long, analytes may not be adequately cryo-focused, resulting in over loading of the secondary column and coelution of analytes. If the hot jet is too short, the analytes may not have enough time to desorb before the next modulation period, resulting in wrap-around.

2.4.3 Folded flight path (FFP) time-of-flight (TOF) mass spectrometer

Time-of-flight mass analyzers provide the fast acquisition rates required for detectors in GCxGC systems. The TOF MS used in this research had a folded-flight-path (FFP) design (2.24). The FFP configuration used nonlinear electrostatic fields in gridless mirrors to transmit ions through a long flight path before striking the detector. The ions were refocused by central lenses

before moving onto the next electrostatic mirror. The FFP design minimized ion loss and improved

the resolution of the instrument. Flight paths of 20 m and 40 m (when the ions travel through the

folded-flight-path twice) had resolutions of approximately 25,000 and 50,000, respectively.
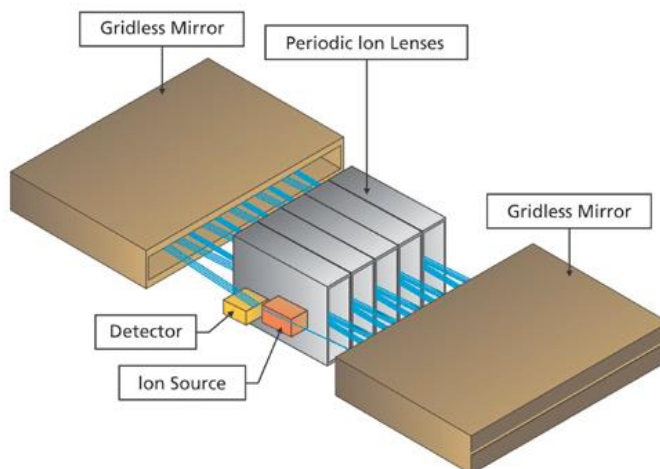
Figure 2.24 Folded-flight-path design of the time-of-flight mass analyzer utilized here.

2.5 References

1. Dietzel, K.D.; Campbell, J.L.; Bartlett, M.G.; Witten, M.L.; Fisher, J. W. Validation of a Gas Chromatography/Mass Spectrometry Method for the Quantification of Aerosolized Jet Propellant 8. *J. Chrom. A* **2005**, *1093* (1-2), 11 – 20.

2. Marshall, A.G.; Rodgers, R.P. Petroleomics: Chemistry of the Underworld. *Proc. Natl. Acad. Sci. USA* **2008**, *105* (47), 18090 – 18095.

3. Han, X.; Aslanian, A.; Yates, J.R. Mass Spectrometry for Proteomics. *Curr. Opin. Chem. Biol.* **2008**, *12* (5), 483 – 490.

4. Belas, F.J.; Blair, I.A. Mass Spectrometry in Pharmaceutical Analysis. *J. Liposome Res*. **2001**, *11* (4), 309 – 342.

5. Maurer, H.H. Mass Spectrometry for Research and Application in Therapeutic Drug Monitoring or Clinical and Forensic Toxicology. *Ther. Drug Monit.* **2018**, *40* (4), 389 – 393.

6. Richardson, S.D. Mass Spectrometry in Environmental Sciences. *Chem. Rev.* **2001**, *101* (2), 211 – 254.

7. Takats, Z.; Wiseman, J.M.; Gologan, B.; Cooks, R.G. Mass Spectrometry Sampling under Ambient Conditions with Desorption Electrospray Ionization. *Science* **2004**, *306* (5695) 471 – 473.

8. Cody, R.B.; Laramee, J.A.; Durst, H.D. Versatile New Ion Source for Analysis of Materials in Open Air Under Ambient Conditions. *Anal Chem.* **2005**, *77* (8), 2297 – 2302.

9. Makarov, A. Electrostatic Axially Harmonic Orbital Trapping: a High Performance Technique of Mass Analysis. *Anal Chem.* **2000**, *72* (6), 1156 – 1162.

10. Carroll, D. I.; Dzidic, I.; Stillwell, R. N.; Horning, M. G.; Horning, E. C. (1974). "Subpicogram Detection System for Gas Phase Analysis Based upon Atmospheric Pressure Ionization (API) Mass Spectrometry". *Anal. Chem.***1974**, *46* (6), 706–710.

11 J. B. Fenn, M. Mann, C. K. Meng, S. F. Wong, and C. M. Whitehouse, Electrospray Ionization for Mass Spectrometry of Large Biomolecules *Science* **1989**, *246*(4926) .64–71, 1989.

12 Robb, D.B.; Covey, T.R.; Bruins, A.P. Atmospheric Pressure Photoionization: An Ionization Method for Liquid Chromatography-Mass Spectrometry. *Anal. Chem.* **2000**, 72 (15), 3653 – 3659..

13. Lattimer, R.P. Schulten, H.R. Field Ionization and Field Desorption Mass Spectrometry: Past, Present and Future. *Anal Chem.* **1989** *61* (21) 1201 – 1215.

14. McLuckey, S.A.; Goeringer, D.E. Slow Heating Methods in Tandem Mass Spectrometry. *J. Mass Spectrom.* **1997**, *32* (5), 461 – 474.

15. Todd, JFJ.; March, RE. A Retrospective Review of the Development and Application of the Quadrupole Ion Trap Prior to the Appearance of Commerical Instruments. *Int. J. Mass Spectrom.* **1999**, *190 (191)*, 9 – 35.

16. Gronert, S. Quadrupole Ion Trap Studies of Fundamenal Organic Reactions. *Mass Spectrom. Rev*. **2005**, *24* (1), 100 – 120.

17. Schwartz, J. C.; Senko, M. W.; Syka, J. E. P. A Two-Dimensional Quadrupole Ion Trap Mass Spectrometer. *J. Am. Soc. Mass Spectrom*. **2002**, *13* (6), 659–669.

18. March, R. E. An Introduction to Quadrupole Ion Trap Mass Spectrometry. *J. Mass Spectrom.* **1997**, *32* (4), 351–369.

19. Owen, B.C.; Gao, J.; Borton, D.J.; Amundson, L.M.; Archibold, E.F.; Tan, X.; Azyat, K.Tywinski, R.; Gray, M.; Kenttämaa, H.I. Carbon Disulfide Reagent Allows the Characterization of Nonpolar Analytes by Atmospheric Pressure Chemical Ionization Mass Spectrometry. *Rapid Commun. Mass Spectrom.* **2011**, *25* (14), 1924 – 1928.

20. Konermann, L.; Rodriguez, A. D.; Liu, J. On the Formation of Highly Charged Gaseous Ions from Unfolded Proteins by Electrospray Ionization, *Anal. Chem*. 2012, *84* (15), 6798

21. Konermann, L.; Ahadi, E.; A. Rodriguez, A.D.; Vahidi, S. Unraveling the Mechanism of Electrospray Ionization *Anal. Chem.* **2013** *85* (1), 2-9

22. March, R. E.; Todd, J. F. J. Quadrupole Ion Trap Mass Spectrometry, 2nd Ed.; Wiley Interscience: Hoboken, N.J., 2005.

23. Douglas, D. J.; Frank, A. J.; Mao, D. Linear Ion Traps in Mass Spectrometry. *Mass Spectrom. Rev.* **2005**, 24 (1), 1–29

24. Douglas, D. J. Linear Quadrupoles in Mass Spectrometry. *Mass Spectrom. Rev.* **2009**, 28 (6), 937–960.

25. Xu. W.; Song, Q.; Smith, S.A.; Chappell, W.J. Ouyang, Z. Ion Trap Mass Analysis at High Pressure: A Theoretical View. *J. Am. Soc. Mass Spectrom.* **2009**, *20* (11), 2144 – 2153.

26. Schwartz, J. C.; Syka, J. E. P.; Jardine, I. J. High Resolution on a Quadrupole Ion Trap Mass Spectrometer. *J. Am. Soc. Mass Spectrom.* **1991**, *2* (3), 198–204.

27. de Hoffmann, E. Tandem Mass Spectrometry: A Primer. *J. Mass Spectrom.* **1996**, *31* (2), 129–137.

28. Makarov, A. Electrostatic Axially Harmonic Orbital Trapping: A High Performance Technique of Mass Analysis. *Anal. Chem*. **2000**, *72* (6), 1156 – 1162.

29. Knight, R.D. Storage of Ions From Laser Produced Plasmas. *Appl. Phys. Lett.* **1981**, *38* (1), 221 – 222.

30. Lewis, R.R. Motion of Ions in the Kingdom Trap. *J. Appl. Phys.* **1982**, *53* (6), 3975 – 3980.

31. Yang, L.; Church, D.A. Confinement of Injected Ions in a Kingdom Trap. *Nucl. Instrum. Methods Nucl. Res.* **1991**, *B56/57* (1), 1185 – 1187.

32. Sekioka, T.; Terasawa, M.; Awaya, Y. Ion Storage in Kingdon Trap. *Rad. Eff. Def. Sol.* **1991**, *117* (1), 253 – 259.

33. Kingdon, K. H. A Method for the Neutralization of Electron Space Charge by Positive Ionization at Very Low Gas Pressures. *Phys. Rev.* **1923**, *21* (408), 408-418.

34. Makarov A. A U.S. Patent 5,886,346, 1999.

35. Gillig KJ,; Bluhm, B.K.; Russell DH. Ion Motion in a Fourier Transform Ion Cyclotron Resonance Wire Ion Guide Cell.*Int. J. Mass Spectrom.* **1996***, 157* (158), 129–147.

36. Perry, R.H.; Cooks, R.G.; Noll, R.J. Orbitrap Mass Spectrometry: Instrumentation, Ion Motion and Applications. *Mass Spec. Rev.* **2008**, *27*(6), 661 – 669.

37. Makarov, A.; Denisov, E.; Kholomeev, A.; Balschun, W.; Lange, O.; Strupat, K.; Horning, S. Performance Evaluation of a Hybrid Linear Ion Trap/Orbitrap Mass Spectrometer. *Anal. Chem.* **2006**, *78* (7), 2113 – 2120.

38. Hardman, M.; Makarov, A.A. Interfacing the Orbitrap Mass Analyzer to an Electrospray Ion Source. *Anal. Chem.* **2003**, *75* (7), 1699 – 1705.

39. Hu, Q.; Noll, R.; Li, H.; Makarov, A.; Hardman, M.; Cooks, R.G. The Orbitrap: a New Mass Spectrometer. *J. Mass Spectrom.* **2005**, *40* (4), 430 – 443.

40. Thermo Fisher Scientific LTQ Orbitrap XL^TM Hardware Manual, Revision B – 1225830, 2008.

41. Olsen, J.V.; Macek, B.; Lange, O.; Makarov, A.; Horning, S.; Mann, M. Higher-energy C-trap Dissociation for Peptide Modification Analysis. *Nature Methods*. **2007**, *4* (9), 709 – 712.

42. McAlister, G.C.; Phanstiel, D.H.; Brumbaugh, J.; Westphall, M.S.; Coon, J.J. Higher-energy Collision-activated Dissociation Without a Dedicated Collision Cell. *Mol. Cell. Proteomic* **2011**, 1 – 6.

43. Murray, K.K.; Boyd, R. K.; Eberlin, M.N.; Langley, G.J.; Li, L.; Naito, Y. Definitions of Terms Relating to Mass Spectrometry (IUPAC recommendations 2013). *Pure Appl. Chem.* **2013**, *85* (7), 1515 – 1609.

44. Liu, Z.; Phillips, J.B. Comprehensive Two-Dimensional Gas Chromatography Using an On-Column Thermal Modulator Interface. *J. Chrom. Sci*. **1991**, *29* (6), 227 – 231.

45. Van der Westhuizen, R.; Ajam, M.; De Coning, P.; Beens, J.; de Villiers, A. Sandra, P. Comprehensive Two-Dimensional Gas Chromatography for the Analysis of Synthetic and Crude-Derived Jet Fuels. *J Chrom. A* **2011**, *1218* (28) 4478–4486.

46 S. Z. Hu, S. F. Li, J. Cao, D. M. Zhang, J. Ma, S. He, X. L. Wang & M. Wu A Comparison of Normal and Reversed Phase Columns in Oil Analysis by Comprehensive Two-dimensional Gas Chromatography With Time-of-flight Mass Spectrometry, *Petrol. Sci.Technol.* **2014**, *32* (5), 565-574,

47. van der Westhuizen, R.; Crouch, A.; Sandra, A. The Use of GCxGC with Time-of-Flight Mass Spectrometry to Investigate Dienes and Diels-Alder Polymerisation Products in High-Temperature Fischer-Tropsch-Based Fuels. *J. Sep. Sci.* **2008,** *31* (1), 3423 – 3428.

48. van der Westhuizen, R.; Potgieter, H.; Prinsloo, N.; de Villiers, A.; Sandra, P. Fractionation by Liquid Chromatography Combined with Comprehensive Two-Dimensional Gas Chromatography-Mass Spectrometry for Analysis of Cyclics in Oligomerisation Products of Fischer-Tropsch Derived Light Alkenes. *J. Chrom. A* **2011**, *1218* (21), 3173 – 3179.

49. van der Westhuizen, R., Crous, R.; de Villiers, A.; Sandra, P.; Comprehensive Two-Dimensional Gas Chromatography for the Analysis of Fischer-Tropsch Oil Products. *J. Chrom. A* **2010**, *1217* (52), 8334 – 8339.

50. Edwards, M.; Mostafa, A.; Gorecki, T. Modulation in Comprehensive Two-Dimensional Gas Chromatography: 20 Years of Innovation. *Anal. Bioanal. Chem.* **2011**, *401* (8), 2335 – 2349.

51. Phillips J.B.; Liu, Z. Comprehensive Two-Dimensional Gas Chromatography Using an On-column Thermal Modulator Interface. *J Chrom. Sci.* **1991**, *29* (6), 227 – 231.

52. Phillips, J.B.; Gaines, R.B.; Blomberg J.; van der Wielen, F.W.M.; Dimandja, J.M.; Green, V.; Granger, J.; Patterson, D.; Racovalis, L.; de Geus H.J.; de Boer, J.; Haglund, P.; Lipsky, J.; Sinha, V.; Ledford E.B. A Robust Thermal Modulator for Comprehensive Two-Dimensional Gas Chromatography. *J. High Res. Chrom.* **1999***, 22* (1), 3 – 10.

53. Bruckner, C.A.; Prazen, B.J.; Synovec, R.E.; Comprehensive Two-Dimensional High-Speed Gas Chromatography with Chemometric Analysis. *Anal. Chem.* **1998**, *70* (14), 2796 – 2804.

54. Seeley, J.V.; Kramp, F.; Hicks, C.J. Comprehensive Two-Dimensional Gas Chromatography via Differential Flow Modulator. *Anal. Chem.* **2000**, *72* (18), 4346 – 4352.

55. Bueno, P.A.; Seeley, J.V. Flow-switching device for Comprehensive Two-Dimensional Gas Chromatography. *J. Chrom. A* **2004**, *1027* (1-2), 3 – 10.

56. Wang, F.C.Y. New Valve Switching Modulator for Comprehensive Two-Dimensional Gas Chromatography. *J. Chrom. A* **2008**, *1188* (2), 274–280.

57. Bertsch, W. Two-Dimensional Gas Chromatography. Concepts, Instrumentation, and Applications – Part 1: Fundamentals, Conventional Two-Dimensional Gas Chromatography, selected Applications. *J. High Res. Chrom.* **1999**, *22* (12), 647–665.

CHAPTER 3.   DISTINGUISHING ISOMERIC HYDROCARBON IONS CONTAINING NAPHTHENE RINGS BY USING ENERGY-RESOLVED MEDIUM ENERGY COLLISION-ACTIVATED DISSOCIATION (MCAD)

3.1   Introduction

In tandem mass spectrometry, unknown isolated ions are often subjected to collision-activated dissociation (CAD) in order to obtain structural information.[1-3] CAD involves acceleration of an ion followed by collisions with a target gas, which converts ion kinetic energy into ion internal energy. The CAD MS^2 spectra depend on the internal energy distribution deposited into the fragmenting ions upon activation.[4,5] The internal energy distribution varies based on the activation method used and on several experimental variables, such as the translational energy of the ions, the mass and type of the target gas atoms or molecules, and the number of activating collisions.[5,6] Some activation methods (such as CAD performed in a quadrupole ion trap) involve multiple collisions between the fragmenting ions and the target gas.[5] Ions may dissociate or isomerize between collisions, which complicates interpretation of the results.[7]

In the linear quadrupole ion trap (LQIT)/orbitrap used in the studies discussed in this thesis, CAD experiments can be performed in several different ways. The most common one involves isolation and CAD of the ions inside the quadrupole ion trap (ITCAD). However, ions isolated in the quadrupole ion trap can also be subjected to CAD in an octupole collision cell (referred here to as medium-energy CAD or MCAD; please see section 2.3.4).[8,9] MCAD is a valuable tool for the structural study of ions because there is no low mass cut-off for fragment ions and the technique can access higher-energy dissociation channels than CAD performed in the quadrupole ion trap.[8] The downside of MCAD is that no further MS^n experiments are possible, and the ions can only be detected in the orbitrap. Direct comparison of ITCAD and MCAD was recently published for

proteomics research.[10-12] Compared to ITCAD, MCAD improved protein quantitation precision,[10] and peptide identification.[11,12] Application of MCAD in other fields is also likely to prove beneficial. While previous studies have demonstrated successful structural molecular level characterization of ions derived from petroleum by using ITCAD,[13,14] only limited information is available on the application of MCAD to petroleum-based samples or related model compounds.[15]

It is noteworthy that the fragment ion spectra of isomeric ions subjected to CAD can be highly sensitive to the collision energy in the low ion kinetic energy regime (1 – 100 eV).[7,16] Therefore, examination of ion fragmentation patterns at different collision energies as opposed to a single energy often provides invaluable structural information that enables the differentiation of ion internal energy effects from structural differences between isomeric ions. This technique is referred to as energy-resolved mass spectrometry (ERMS).

The aim of this study was to compare the effectiveness of ERMS ITCAD and ERMS MCAD at distinguishing ionized aromatic naphthene-containing isomers. The ability to distinguish these isomeric compounds from each other has practical applications for the petroleum industry. For example, to improve the cetane number of diesel fuel and the overall fuel quality, fuel companies may attempt to open the naphthene-rings in aromatic compounds by using oxide and zeolite catalysts.[17-20] The exact structures of the naphthene-containing compounds greatly influence the ring-opening rates (Figure 3.1).[20] Hence, the ability to elucidate the structures of the naphthene-containing compounds in fuels and their precursors is important. Several isomeric aromatic naphthene-containing model compounds and *trans*-stilbene (Figure 3.2) were ionized by using APCI with CS_2 solvent to produce stable molecular ions.[21] The molecular ions were subjected to ITCAD and MCAD in the ERMS mode and the ITCAD fragment ions were detected at low

resolution in the ion trap and at high resolution in the orbitrap while those formed upon MCAD were only detected in the orbitrap.
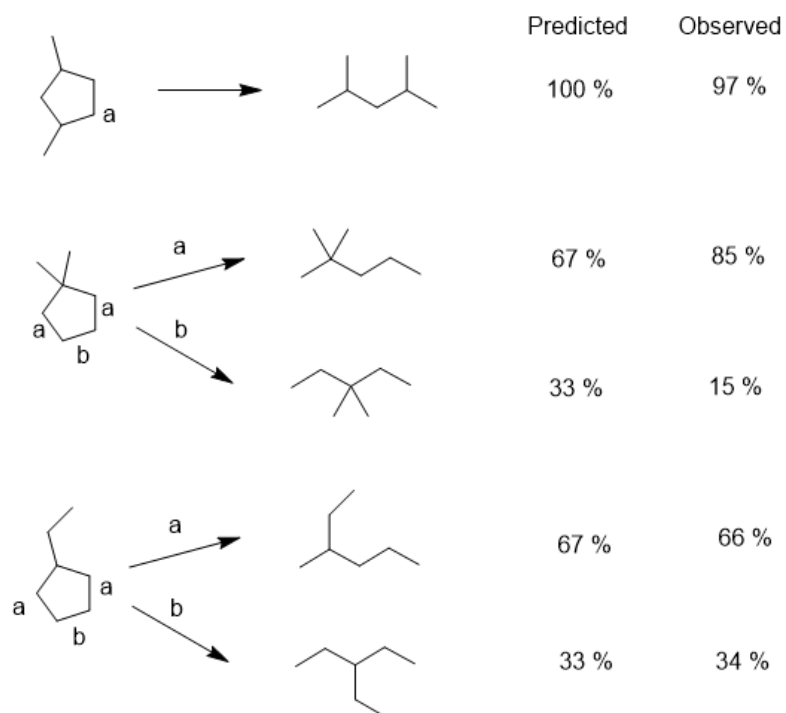
Figure 3.1 The predicted and observed products of isomeric C_7-cyclopentanes with 0.9 % Ir/Al$_2$O$_3$. Conditions were 548 K and 3540 kPa of H$_2$
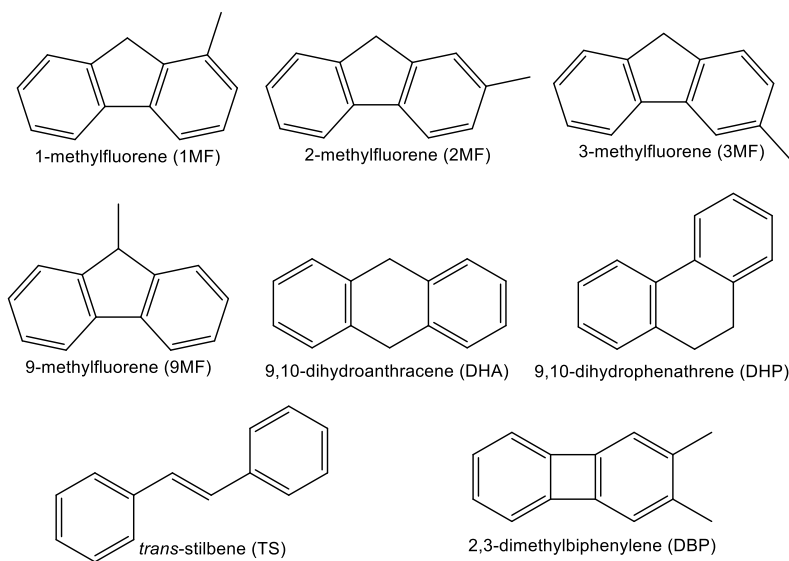
Figure 3.2 Names, abbreviations and structures for the isomeric model compounds studied.

3.2   Experimental

3.2.1   Chemicals

1-Methylfluorene (98 % purity), 9-methylfluorene (purity not provided), 9,10-dihydroanthracene (97 % purity), 9,10-dihydrophenanthrene (94 % purity), and *trans*-stilbene (96 % purity) were purchased from Sigma-Aldrich (St. Louis, MO). 2-Methylfluorene (97 % purity) and 3-methylfluorene (97 % purity) were purchased from AK Scientific (Union City, CA). CS_2 (99.9 % purity) was purchased from Alfa Aesar (Haverhill, MA). All purchased compounds were used as received without additional purification.

3.2.2   Chemical synthesis of 2,3-dimethylbiphenylene (DBP)

2,3-Dimethylbiphenylene was synthesized in house by Yuyang Zhang using previously described methods.[22,23] All reagents and starting materials were obtained commercially and were used as received. Dicarbonylcyclopentadienylcobalt (purity not provided) was purchased from Alfa Aesar. Ethynyltrimethylsilane (98 % purity), 2-butyne (99 % purity) and 1,2-diiodobenzene (98 % purity) were purchased from Sigma-Aldrich (St. Louis, MO).

3.2.3   Instrumentation and sample preparation

ITCAD and MCAD measurements were performed by using a Thermo Scientific LTQ Orbitrap XL mass spectrometer (Thermo Scientific, San Jose, CA, USA) equipped with an APCI source. Each compound (Figure 3.2) was dissolved in CS_2 at a concentration of approximately 20 µM and injected into the APCI source at a flow rate of 2.0 µL / min by using an auto injector. The ionization conditions were as follows: vaporizer temperature 280 ℃, capillary temperature 280 ℃, Corona discharge current 3.2 µA, capillary voltage 10 V, and tube lens voltage 20.5 V. N_2 gas was employed as the sheath and auxiliary gases at flow rates of 28 and 12 arbitrary units,

respectively, to maintain a stable spray. An isolation window of 1.0 m/z unit was used to isolate the molecular ions in the linear quadrupole ion trap.

3.2.4   ITCAD measurements in the ERMS mode at low and high resolution

The molecular ions for all isomeric compounds were subjected to ITCAD at collision energies ranging from 0 up to 60 (arbitrary units) at a q value of 0.25. The activation time was set to 30 ms. For high-resolution measurements, the orbitrap was set to a resolution of 100,000. The measurements were repeated on three separate days for each ionized compound at high and low resolution. The relative abundances of ions of m/z 180, 179, 178 and 165 were recorded for one measurement each day. The three measurements were averaged individually, and a standard deviation ($\sigma = 1$) was determined from the three separate measurements. The average relative abundance values of ions of m/z 180, 179, 178 and 165 were plotted as a function of collision energy for measurements completed at high and low resolution.

3.2.5   MCAD measurements in the ERMS mode at high resolution

Molecular ions were also subjected to MCAD in an octupole collision cell (MCAD cell) at collision energies ranging from 0 up to 34 eV. The activation time was set to 30 ms. The resolution was set to 100,000. The measurements were performed on three separate days for each ionized compound. The relative abundances of ions of m/z 180, 179, 178 and 165 were recorded, averaged individually, and a standard deviation ($\sigma = 1$) was determined from the three separate measurements. The average relative abundances for ions of m/z 180, 179 178 and 165 were plotted as a function of collision energy. For ionized *trans*-stilbene, the average relative abundances of fragment ions of m/z 102 were also plotted as a function of collision energy.

3.2.6 Crossing-point energy and modified crossing point energy determination

Distinction of ionized structural isomers was facilitated by using crossing-point energies (collision energies where the molecular ion and a given fragment ion have an equal abundance) and modified crossing-point energies for either ions of m/z 180 and m/z 165 or ions of m/z 180 and m/z 179. The crossing-point energies were read directly from the plots. The modified crossing-point energies were determined by a two-step process. First, a trend line was produced by plotting the logarithm of the ratio of the abundances of ions of m/z 180 and ions of m/z 165 as a function of collision energy (in arbitrary units for ITCAD and eV for MCAD). Then, the modified crossing-point energies were assigned to be those collision energy values where the trend line intersected the x-axis (where ions of m/z 180 and 165 or ions of m/z 180 and 179 have an equal abundance). The reported crossing-point and modified crossing-point energies were an average of three separate measurements. A standard deviation ($\sigma = 1$) was determined.

3.2.7 Residence time studies

Isolated molecular ions of DHA were subjected to ITCAD and MCAD in the ERMS mode at the collision energies described above for a time period of 0.03 ms, 0.3 ms, 3.0 ms, 30 ms, and 300 ms. The relative abundances of ions of m/z 180 179, 178 and 165 were recorded and plotted individually as a function of ITCAD energy (arbitrary units) or MCAD collision energy (eV).

3.2.8 Calculations and computer program

All calculations were performed with the Gaussian16 program suite.[24] Unrestricted wave functions were utilized for geometry optimization and computation of enthalpies for all structures. Bond dissociation energies were calculated using equation 3.1 (illustrated for an ion R_1-$R_2^{+\bullet}$ dissociating into $R_1^{\bullet}$ and R_2^+)

$$Bond\ dissociation\ energy = \Delta H(R_1^{\bullet}) + \Delta H(R_2^+) - \Delta H([R_1 - R_2]^{+\bullet}) \qquad (3.1)$$

where $\Delta H(R_1{}^\bullet)$ is the enthalpy of the neutral radical fragment, $\Delta H(R_2{}^+)$ is the enthalpy for the fragment ion and $\Delta H([R_1\text{-}R_2]^{+\bullet})$ is the enthalpy of the molecular ion.

Geometry optimizations were completed by using UB3LYP/6-311G(d,p) level of theory[25,26] and thermochemical values were subsequently calculated with the UB3P86 function.[25,27] This function has been shown to successfully estimate bond dissociation energies for neutral molecules.[28-31] The calculations were performed by Dr. Mckay Easton.

3.3   Results and Discussion

ERMS experiments provide a two-dimensional mass spectrum showing the relative abundances of the fragmenting ions as a function of collision energy. When two different ions have an equal abundance, the lines intersect, and a crossing-point energy is obtained.[32] The use of crossing point energies to distinguish ionized structural isomers has been established in the literature[32] and was attempted in this study to facilitate differentiation of ionized aromatic naphthene-containing structural isomers.

3.3.1   Distinguishing isomeric molecular ions of DHA, DHP and TS by using ITCAD and MCAD in the ERMS mode

9,10-dihydroanthracene (DHA)   9,10-dihydrophenathrene (DHP)

trans-stilbene (TS)
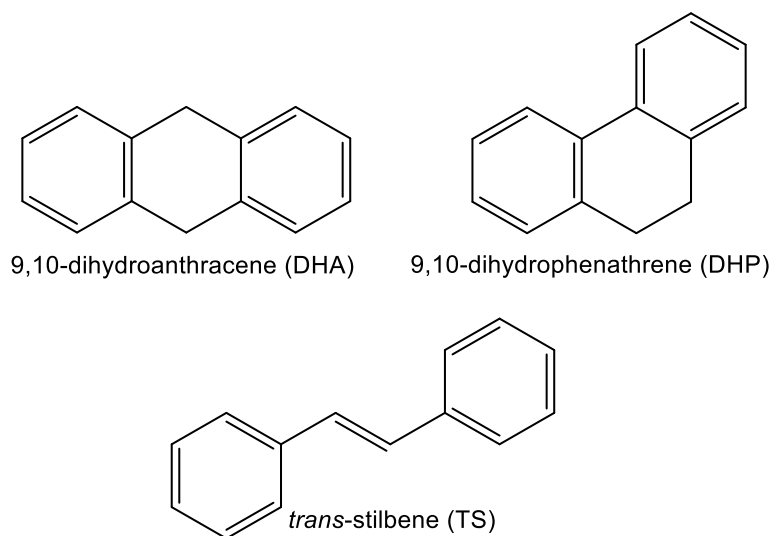
Figure 3.3 Structures of DHA, DHP and TS.

When the molecular ions of DHA, DHP and TS were subjected to ITCAD, they fragmented predominantly via a rearrangement reaction leading to methyl radical loss to produce fragment ions of m/z 165 (Figure 3.4). To a lesser extent, all three ions also fragmented by the loss of a hydrogen atom to produce fragment ions of m/z 179 and the loss of two hydrogen atoms to produce fragment ions of m/z 178. As the relative abundance of the fragment ions of m/z 179 decreased with increasing collision energy, the relative abundance of the fragment ions of m/z 178 increased (Figure 3.4). This result suggests that fragment ions of m/z 178 are produced from ions of m/z 179 via the loss of another hydrogen atom.
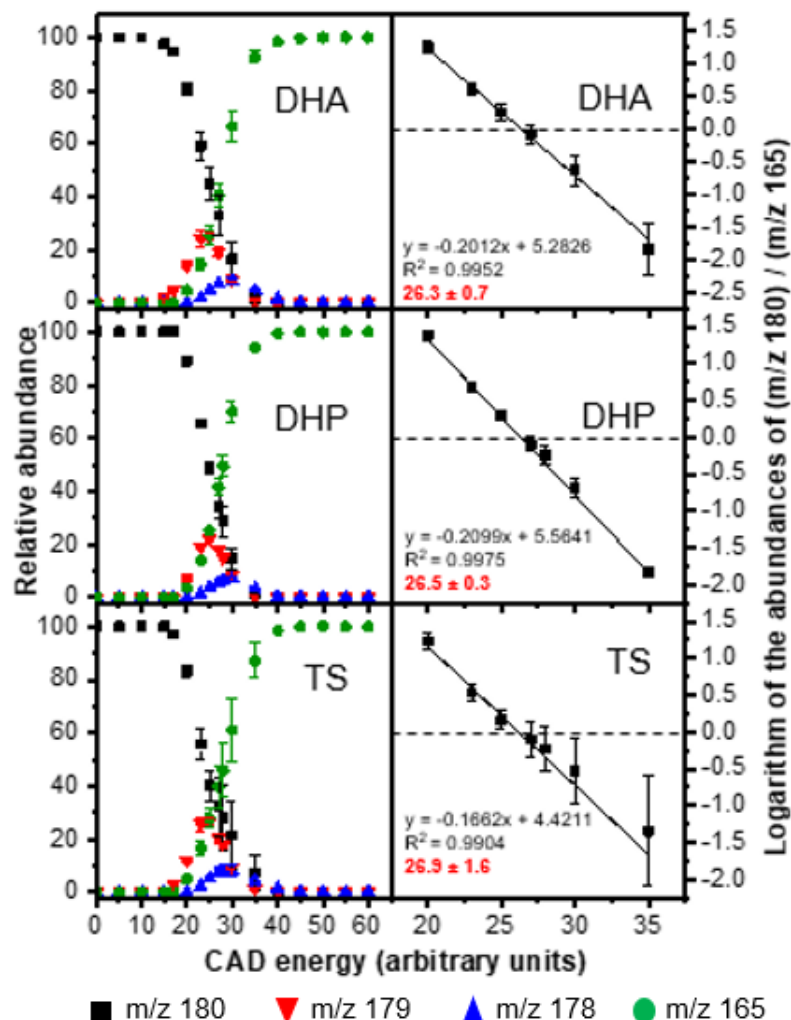
Figure 3.4 ERMS ITCAD plots for ionized DHA, DHP and TS are shown in the left column. The trend lines and formulas used to determine the modified crossing-point energies (where ions of m/z 180 and 165 have an equal abundance) are shown in the right column. The modified crossing-point energies are in red text. Each data point is an average of three separate measurements completed on three separate days. The error bars correspond to one standard deviation ($\sigma = 1$).

The ERMS ITCAD plots for ionized DHA, DHP and TS look similar (Figure 3.4). Indeed, the modified crossing-point energies for ions of m/z 180 and 165 for ionized DHA, DHP and TS are essentially identical (26.3 ± 0.7, 26.5 ± 0.3 and 26.9 ± 1.6, respectively). Hence, this approach cannot be used to distinguish between ionized DHA, DHP and TS.

When ionized DHA, DHP and TS were subjected to ERMS MCAD, they fragmented predominantly via a fast σ-bond cleavage leading to the loss of a hydrogen atom to produce fragment ions of m/z 179 (Figure 3.5). To a moderate extent, all three ions also fragmented by loss of a methyl radical via rearrangement reactions to produce fragment ions of m/z 165.

The modified crossing-point energy for the ions of m/z 180 and 179 (due to elimination of a hydrogen atom) for ionized DHA (13.4 ± 0.2 eV) was distinctly lower than that determined for ionized DHP (17.4 ± 0.1 eV), in agreement with the calculated homolytic bond dissociation energies (BDE) (DHA: 37.0 kcal; DHP: 54.9 kcal; Table 3.1). Possible reaction mechanisms leading to methyl radical loss for ionized 1MF, 2MF, 3MF, 9MF and DBP via sigma bond cleavage are shown in Figure 3.6. Hence, this approach enables the distinction of ionized DHA and DHP.

Table 3.1 The modified crossing-point energies derived from ERMS plots generated based on ITCAD and MCAD measurements and the calculated homolytic bond dissociation energies (BDE) for the molecular ions (for the reactions involving methyl radical loss, see Figure 3.6). The BDE values were calculated using the UB3LYP/6-311G(d,p)//UB3P86/6-311++G(2df,p) level theory (completed by Mckay Easton).

Structural isomer	Dissociation pathway	ITCAD modified crossing-point energy (arbitrary units)	MCAD modified crossing-point energy (eV)	Calculated homolytic bond dissociation energy (kcal)
$DHA^{+\bullet}$	•H atom loss	26.3 ± 0.7	13.4 ± 0.2	37.0
$TS^{+\bullet}$	•H atom loss	26.9 ± 1.6	13.9 ± 0.1	47.5
$DHP^{+\bullet}$	•H atom loss	26.5 ± 0.3	17.1 ± 0.1	54.9
$9MF^{+\bullet}$	•CH_3 loss	23.4 ± 0.5	12.7 ± 0.05	50.8
$1MF^{+\bullet}$	•CH_3 loss	24.5 ± 0.9	15.0 ± 0.2	103.7
$3MF^{+\bullet}$	•CH_3 loss	24.3 ± 0.7	15.1 ± 0.1	107.3
$2MF^{+\bullet}$	•CH_3 loss	24.6 ± 0.7	15.8 ± 0.1	111.7
$DBP^{+\bullet}$	•CH_3 loss	24.3 ± 0.2	18.0 ± 0.1	111.9
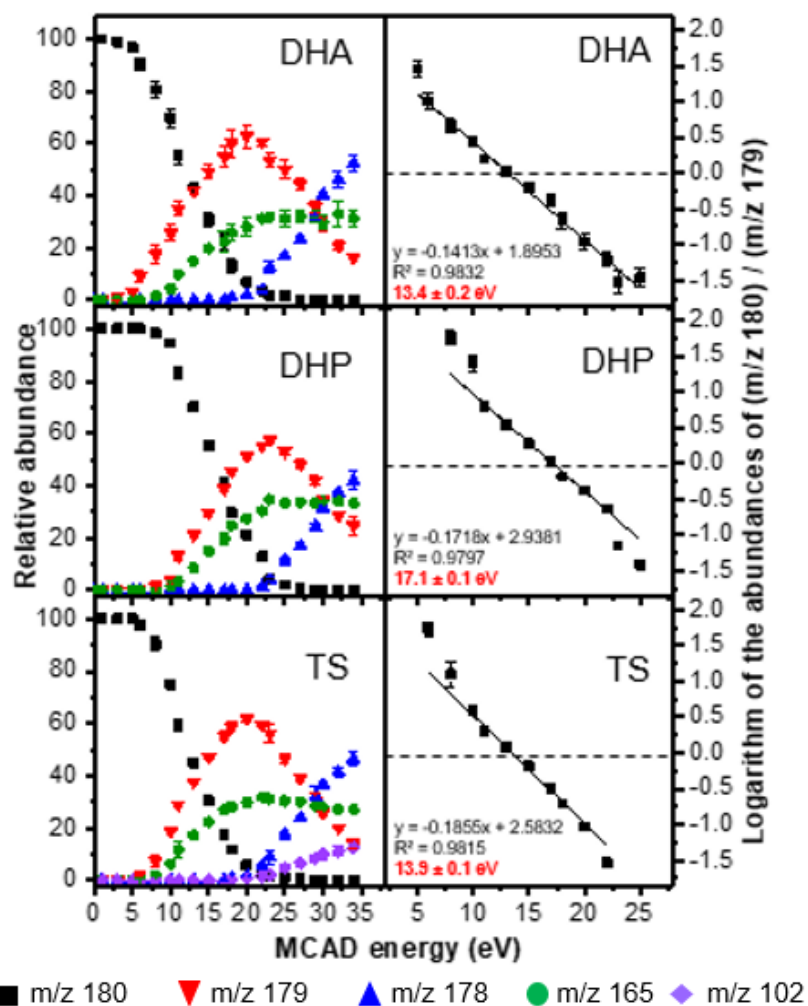
Figure 3.5 ERMS MCAD plots for ionized DHA, DHP and TS are shown in the left column. The trend lines and formulas used to determine the modified crossing-point energies (where ions of m/z 180 and 179 have an equal abundance) are presented in the right column. The modified crossing-point energies are in red text. Each data point is an average of three separate measurements. The error bars correspond to one standard deviation ($\sigma = 1$).
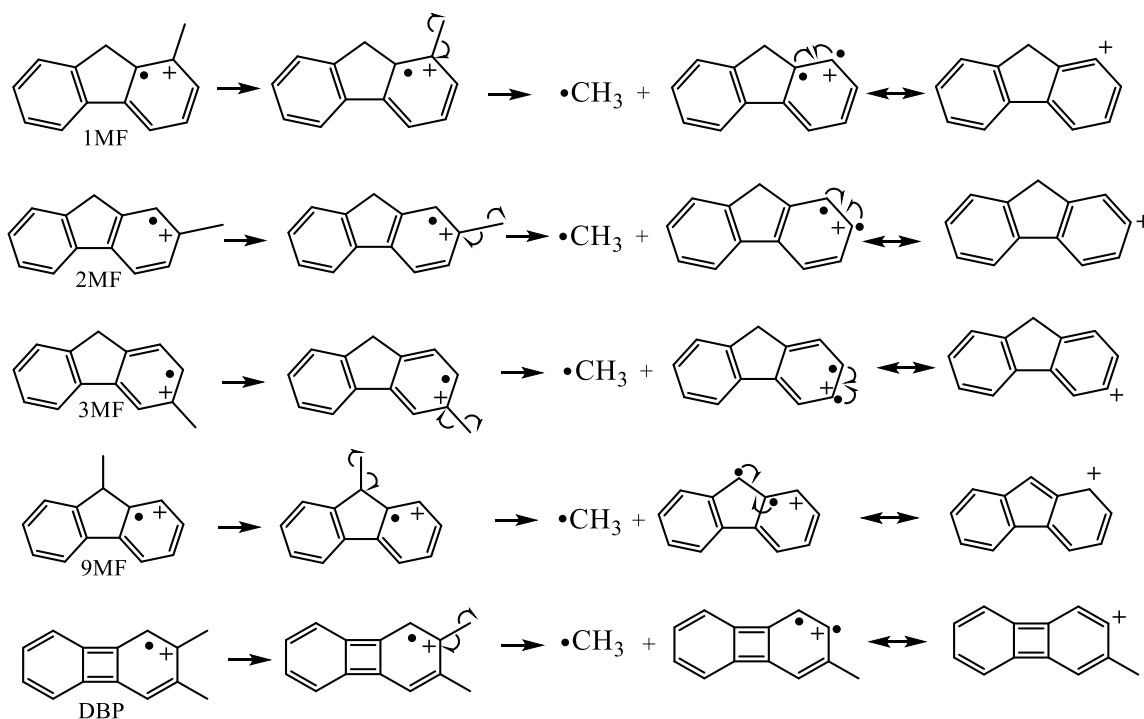
Figure 3.6 Reaction mechanisms leading to methyl radical loss via a direct bond cleavage from ionized 1MF, 2MF, 3MF 9MF and DBP.

Ionized DHA and DHP also generated fragment ions of m/z 178 via loss of two hydrogen atoms upon ERMS MCAD at collision energies at about 18 eV or greater. As the relative abundance of the fragment ions of m/z 179 decreased upon increasing collision energy, the relative abundance of the fragment ions of m/z 178 increased. This finding suggests that the fragment ions of m/z 178 are produced from fragment ions of m/z 179 via loss of another hydrogen atom. Ionized DHA and DHP also fragmented via a rearrangement reactions leading to the loss of a methyl radical to produce fragment ions of m/z 165 but to a lesser extent when compared to the hydrogen atom loss reactions (Figure 3.5).

When the molecular ions of TS were subjected to MCAD, they fragmented predominantly via a σ-bond cleavage leading to the loss of a hydrogen atom (Figure 3.5). The modified crossing-point energy for ions of m/z 180 and 179 was 13.9 ± 0.1 eV, which is distinctly different from that measured for ionized DHA and DHP. Further, fragment ions of m/z 102 were also produced via loss of benzene at MCAD energies ≥ 20 eV. Hence, ionized TS is distinguished from ionized DHA and DHP based on different modified-crossing point energies and the loss of benzene only observed for ionized TS upon MCAD, unlike ITCAD. Hence, additional dissociation reactions that occur when using ERMS MCAD may provide more detailed information than ERMS ITCAD.

It is noteworthy that the major fragmentation pathway for ionized DHA, DHP and TS differed when the ions were subjected to ITCAD and MCAD. When the ions were subjected to ITCAD, the dominant fragmentation was the loss of a methyl radical via rearrangement reactions. However, upon MCAD, the dominant reaction was the loss of a hydrogen atom via a σ-bond cleavage.

During ion activation, greater internal energy is likely deposited into the molecular ions when they are subjected to MCAD compared to ITCAD, which is attributed to the mass of the target gas and the translational energy of the ions prior to collisional activation. The target gas inside the ion trap and the octupole collision cell are He and N_2 gas, respectively. The mass of N_2 (28 Da) is seven times greater than that of helium (4 Da). Hence, ions that collide with N_2 gas acquire greater center-of-mass energy (E_{cm}) when compared to ions that collide with He. The center of mass energy is expressed as[5,33]

$$E_{cm} = KE_{lab} \left(\frac{N}{m_p^+ + N} \right) \tag{3.1}$$

where KE_{lab} is the laboratory kinetic energy of the ion, N is the mass of the target gas and m_p^+ is the mass of the singly-charged ion. Further, to activate ions in the ion trap, resonant excitation is

used to increase their kinetic energy to facilitate energetic collisions with He. The kinetic energy of the ions is limited by the trapping well depth of the ion trap. Conversely, ions activated by MCAD do not have this limitation as they are accelerated via a potential offset between the C-trap and the octupole collision cell (section 2.3.4). Ions entering the octupole collision cell can have greater kinetic energy than in the ion trap. The greater kinetic energy, combined with a heavier target gas, results in a greater conversion of the kinetic energy into internal energy. Hence, ions can dissociate via higher-energy dissociation channels when activated by MCAD compared to ITCAD, which may explain why ionized TS fragments by loss of benzene when subjected to MCAD but not to ITCAD. This difference in the energetics explains, in part, why the lowest-energy fragmentation pathway, methyl radical loss, dominates for ITCAD but the faster reaction, hydrogen atom loss, dominates for MCAD.

To explore the influence of the time regimes of the two activation methods, ionized DHA was subjected to ERMS ITCAD and ERMS MCAD at ion residence times of 0.03 ms, 0.3 ms, 3.0 ms, 30 ms and 300 ms (Figure 3.7). The longer the residence time, the more activating collisions the ions undergo. When subjected to ITCAD, ionized DHA was found to yield fragment ions at residence times ≥ 3 ms. The ERMS ITCAD plot obtained at 3 ms resembled the plots obtained for MCAD but the others do not. Therefore, one reason for the dominance of methyl radical loss upon ITCAD was that at longer residence times, the fragmenting ions underwent many low-energy collisions, which facilitated rearrangement reactions. Only at a short residence time (3 ms), the ions produced an ERMS plot that resembled those obtained by using MCAD.

All ERMS MCAD plots looked similar, independent of the residence time. This result suggests that both the ion activation and fragmentation occurred within the microsecond time regime as changing the residence time longer than 0.03 ms did not change the ERMS plots. Hence,

when ionized DHA, DHP and TS were subjected to MCAD, dissociation via the fast σ-bond cleavage (leading to the loss of a hydrogen atom) was preferred over the slow rearrangement reaction (leading to the loss of a methyl radical). However, when ionized DHA, DHP and TS were subjected to ITCAD, the ions were afforded with more time between activating collisions that only deposited small amounts of internal energy into the ions. Therefore, the ions underwent predominant isomerization (with lower barriers than hydrogen atom loss) and eventually fragmented by loss of the methyl radical via a slow rearrangement reaction.
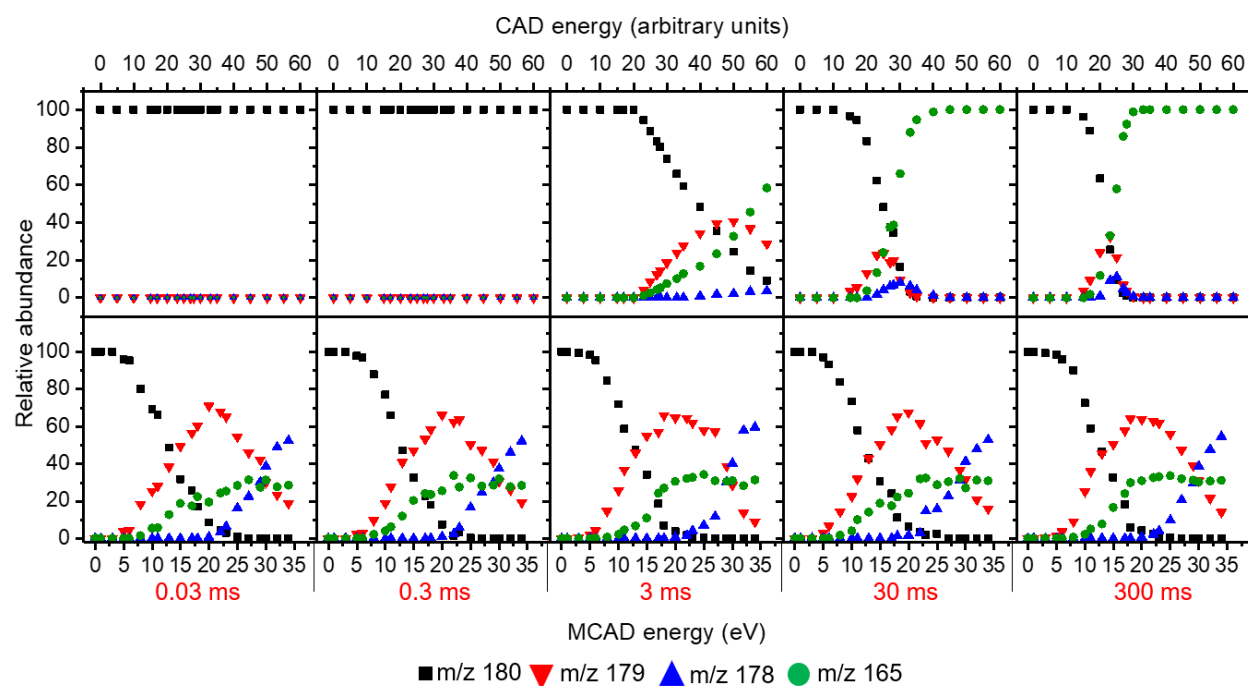
Figure 3.7 The ERMS plots for molecular ions of DHA subjected to ITCAD (top row) and MCAD (bottom row) using different ion residence times. The residence time is in red text.

3.3.2 Distinguishing isomeric ions 1MF, 2MF, 3MF, 9MF and DBP by using ITCAD and MCAD in the ERMS mode
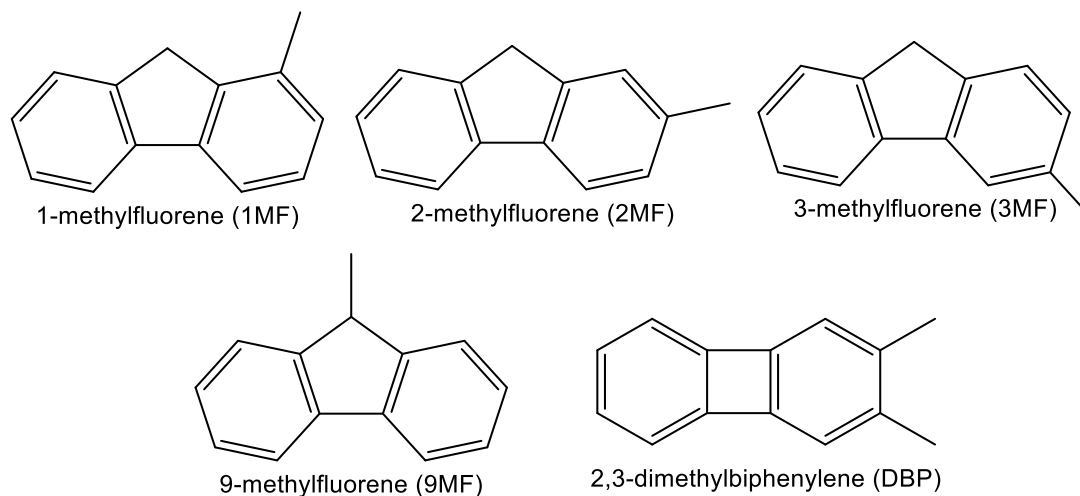
Figure 3.8 Structures of 1MF, 2MF, 3MF, 9MF and DBP.

The ERMS plots for ionized 1MF, 2MF, 3MF and 9MF subjected to ITCAD and MCAD are presented in Figures 3.9 and 3.10, respectively. Upon ITCAD, the ionized five-membered naphthene-containing compounds 1MF, 2MF, and 3MF, fragment predominantly by the loss of a methyl radical via rearrangement reactions as direct σ-bond cleavages require too much energy to compete with the hydrogen atom loss (Table 3.1). Possible rearrangement reactions for methyl radical loss for ionized 1MF and 3MF subjected to ITCAD are shown in Figure 3.11. Ionized 9MF fragments by loss of a methyl radical via a sigma-bond cleavage. The loss of a hydrogen atom was also observed (m/z 179) for ionized 1MF, 2MF, 3MF and 9MF but to a much lesser extent (the maximum relative abundance of fragment ions of m/z 179 was less than 2 %). The ERMS ITCAD plots for ionized 1MF, 2MF, 3MF and 9MF are similar. The average modified crossing-point energies (where ions of m/z 180 and 165 have an equal abundance) were essentially identical for 1MF, 2MF and 3MF but slightly lower for 9MF 1MF (24.5 ± 0.9), 2MF (24.6 ± 0.7), 3MF (24.3

± 0.7) and 9MF (23.4 ± 0.5). Hence, ERMS ITCAD cannot be used to distinguish between ionized

1MF, 2MF, and 3MF and even distinguishing 9MF from the other isomers is questionable.
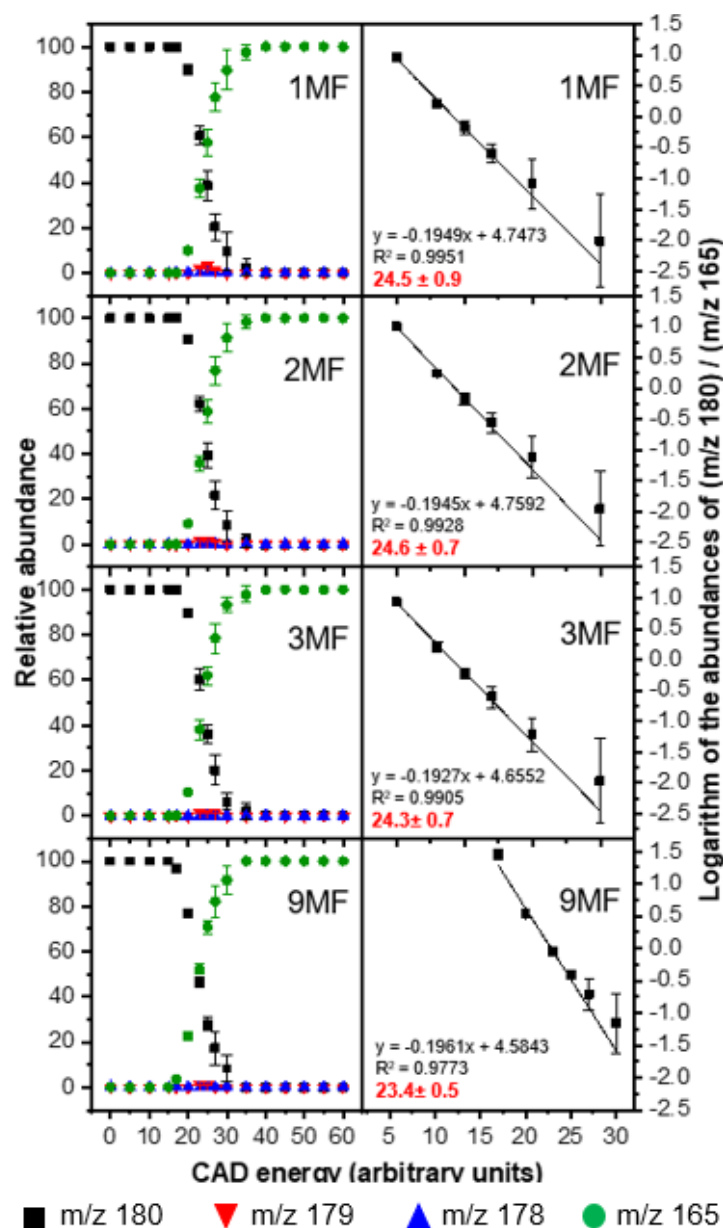
Figure 3.9 ERMS ITCAD plots for ionized 1MF, 2MF, 3MF and 9MF are presented in the left column. The trend lines and formulas used to determine the modified crossing-point energies (where ions of m/z 180 and 165 have an equal abundance) for ionized 1MF, 2MF, 3MF and 9MF are presented in the right column. The modified crossing-point energies are in red text. Each data point is an average of three separate measurements. The error bars correspond to a standard deviation of one σ = 1).
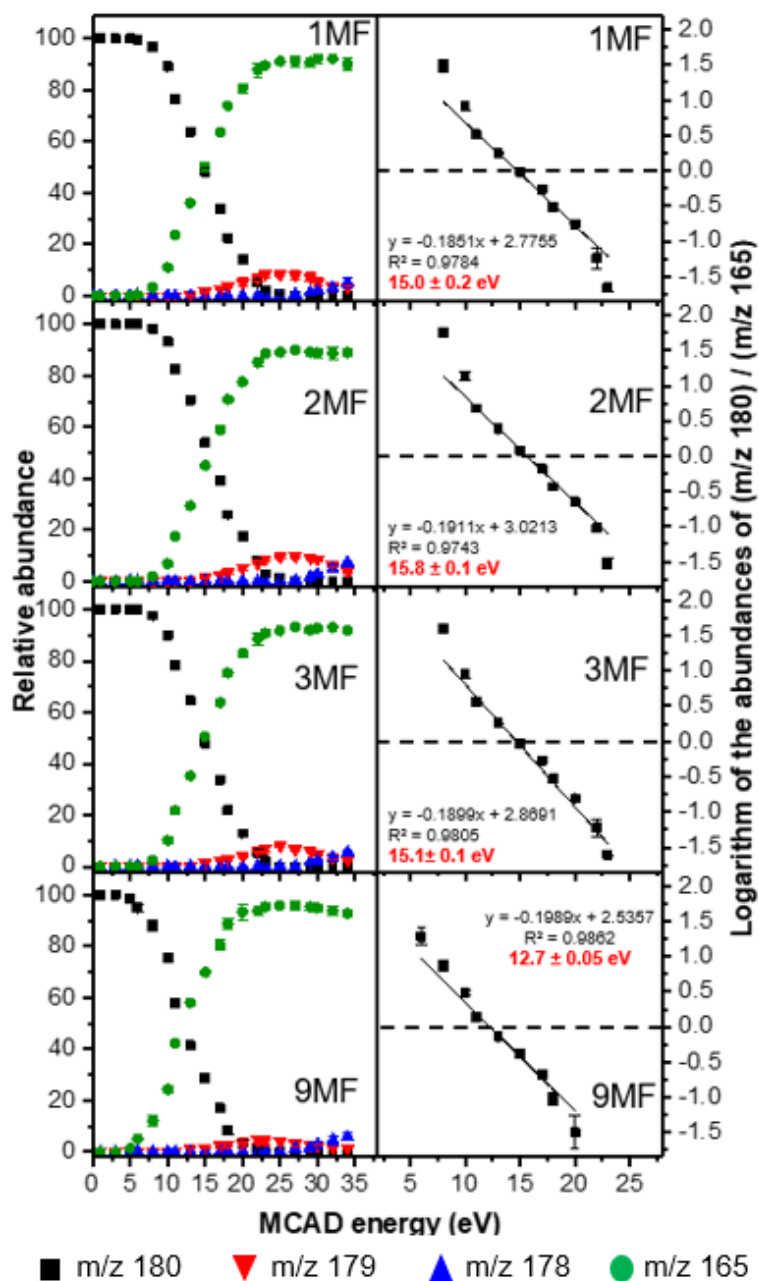
Figure 3.10 MCAD / ERMS plots for ionized 1MF, 2MF, 3MF and 9MF are shown in the left column. The trend lines and formulas used to determine the modified crossing-point energies (where ions of m/z 180 and 165 have an equal abundance) are presented in the right column. The modified crossing-point energies are in in red text. Each data point is an average of three separate measurements. The error bars correspond to one standard deviation ($\sigma = 1$).
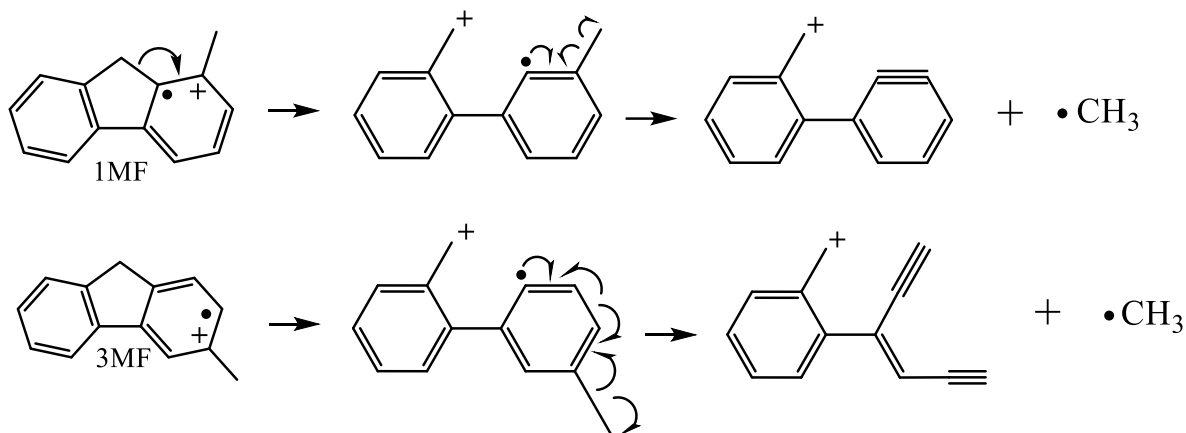
Figure 3.11 Possible rearrangement reactions for methyl radical loss for ionized 1MF and 3MF subjected to MCAD.

Upon MCAD, ionized 1MF, 2MF, 3MF and 9MF fragment predominantly by the loss of a methyl radical (Figure 3.10), just as upon ITCAD. However, the molecular ions yield larger amounts of fragment ions formed upon loss of a hydrogen atom (m/z 179) and consecutive loss of two hydrogen atoms (m/z 178). The maximum relative abundances of fragment ions of m/z 179 and 178 range from 6 up to 9 %. The greater abundances of these fragment ions for MCAD is attributed to the greater internal energy deposited into the molecular ions.

As ionized 1MF, 2MF, 3MF and 9MF fragment predominantly by loss of a methyl radical while ionized DHA and DHP fragment predominantly by loss of a hydrogen atom upon MCAD, this technique can be used to differentiate between the five- and six-membered naphthene-containing isomeric ions.

The ERMS MCAD plots for ionized 1MF, 2MF, 3MF and 9MF look similar but the modified crossing-point energies (where ions of m/z 180 and 165 have an equal abundance) can be used to distinguish most of the isomers. The modified crossing-point energies in increasing order are 12.7 ± 0.05 eV for 9MF, 15.0 ± 0.2 eV for 1MF, 15.1 ± 0.1 eV for 3MF, and 15.8 ± 0.2

eV for 2MF. Therefore, all other isomers can be distinguished from the others except for ionized 1MF and 3MF that cannot be distinguished from each other.

The ERMS ITCAD and ERMS MCAD plots for the ionized four-membered naphthene-containing compound DBP are presented in Figure 3.12. Ionized DBP fragments predominantly by methyl radical loss via a rearrangement reaction. For ITCAD, the modified crossing-point energy (where ions of m/z 180 and 165 have an equal abundance) for ionized DBP is 24.3 ± 0.2. This value is not significantly different from those determined for the ionized five-membered naphthene-containing compounds 1MF, 2MF, 3MF and 9MF and the six-membered compounds DHA and DHP. Hence, ITCAD cannot be used to distinguish between the ionized four- and five- and six-membered naphthene-containing isomeric compounds.

For MCAD, DBP fragments predominantly by methyl radical loss via a rearrangement reaction. The loss of a hydrogen atom was also observed (m/z 179) with a maximum relative abundance of 7 %. Ionized DBP also yielded fragment ions of m/z 178 by consecutive losses of two hydrogen atoms (m/z 178) with the maximum abundance of 7 %. The modified crossing-point energy (where ions of m/z 180 and 165 have an equal abundance) for ionized DBP is 18.0 ± 0.1 eV, which is different from the modified crossing-point energies determined for the ionized five-membered naphthene-containing compounds. The dominant dissociation pathway for ionized DBP differs when compared to the six-membered naphthene-containing compounds DHA and DHP. Hence, ionized DBP can be distinguished from the ionized the five-membered naphthene-containing compounds 1MF, 2MF, 3MF and 9MF and the six-membered naphthene-containing compounds DHA and DHP.
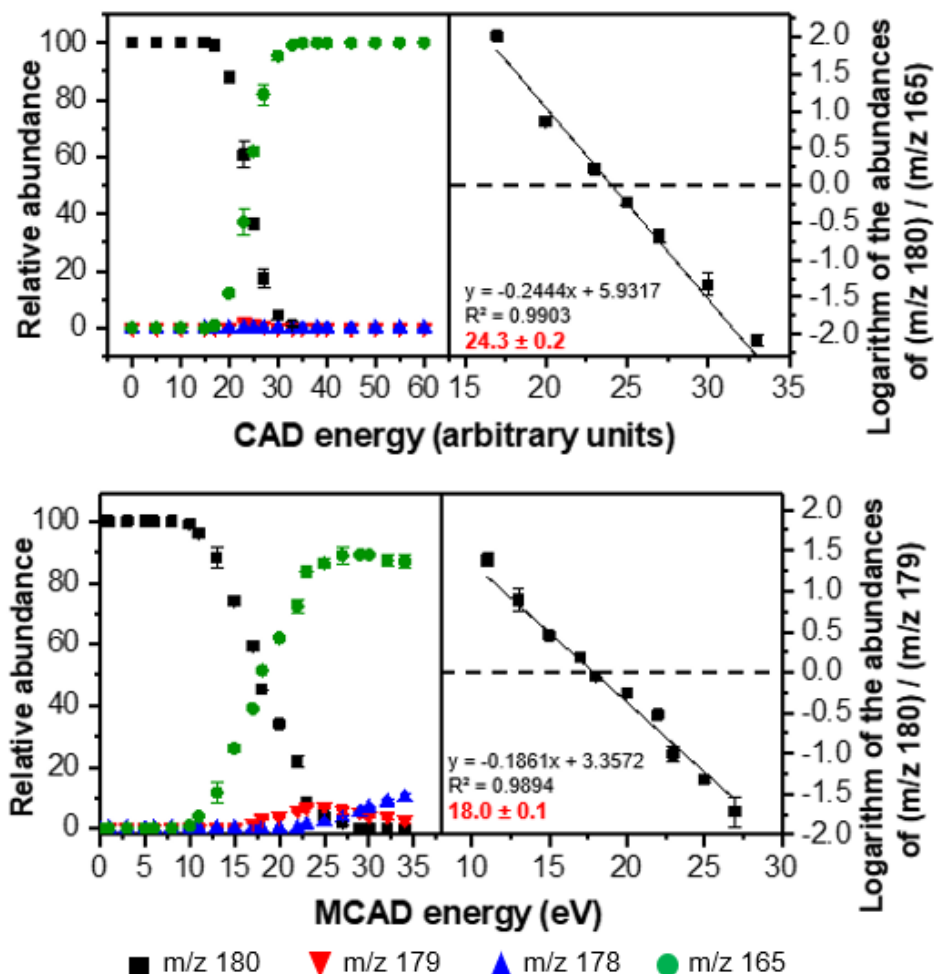
Figure 3.12 ITCAD / ERMS plot for ionized DBP is shown in the top left column and the trend line and formula used to determine the modified crossing-point energy (where ions of m/z 180 and 165 have an equal abundance) are presented in the top right column.. MCAD / ERMS plot for ionized DBP is shown in the bottom left column and the trend line and formula used to determine the modified crossing-point energy (where ions of m/z 180 and 165 have an equal abundance) are presented in the bottom right column. Each data point is an average of three separate measurements. The error bars correspond to one standard deviation ($\sigma = 1$).

A striking difference between the ITCAD and MCAD / ERMS plots is the reproducibility of the relative abundances of the molecular and fragment ions from the three separate measurements (compare Figures 3.4 and 3.5 and Figures 3.9 and 3.10). The relative abundances for the ions in the ERMS MCAD plots are more reproducible than the ERMS ITCAD plots. For example, the average standard deviations for the relative abundances of ionized 1MF from the

ERMS ITCAD and MCAD plots are ± 5.1 and ± 1.2, respectively. The exception was for ionized DBP where the standard deviations from both plots are similar. For example, the standard deviations for the relative abundances of fragment ions of m/z 165 in the ERMS ITCAD and MCAD plots were ± 2.0 and ± 1.4, respectively. The great reproducibility of the ERMS MCAD plots facilitated successful differentiation of the ionized isomeric compounds.

3.3.3 ERMS ITCAD measurements at low and high mass resolution

The low- and high-resolution data obtained for ionized DHA and DHP subjected to ERMS ITCAD are compared in Figure 3.13. The fragment ions of m/z 179 and 178 appeared to be less abundant or were not detected when using high-resolution detection as compared to low-resolution detection. This finding suggests that the ERMS ITCAD measurements performed at high mass resolution are less reliable at providing structural information than low-resolution measurements. For example, for low-resolution ITCAD measurements performed for ionized DHA, fragment ions of m/z 179 and 178 have maximum relative abundances of 24.0 % and 8.4 %, respectively. For the analogous high-resolution measurements, fragment ions of m/z 179 had a maximum relative abundance of 3.6 % while fragment ions of m/z 178 were not detected. For low-resolution ITCAD measurements performed for ionized DHP, fragment ions of m/z 179 and 178 have maximum abundances of m/z 22.1 % and 7.0 %, respectively. For the analogous high-resolution measurements, fragment ions of m/z 179 had a maximum relative abundance of 1.6 % while fragment ions of m/z 178 are not detected. The limited dynamic range of the orbitrap may explain above observations (Figure 3.14).
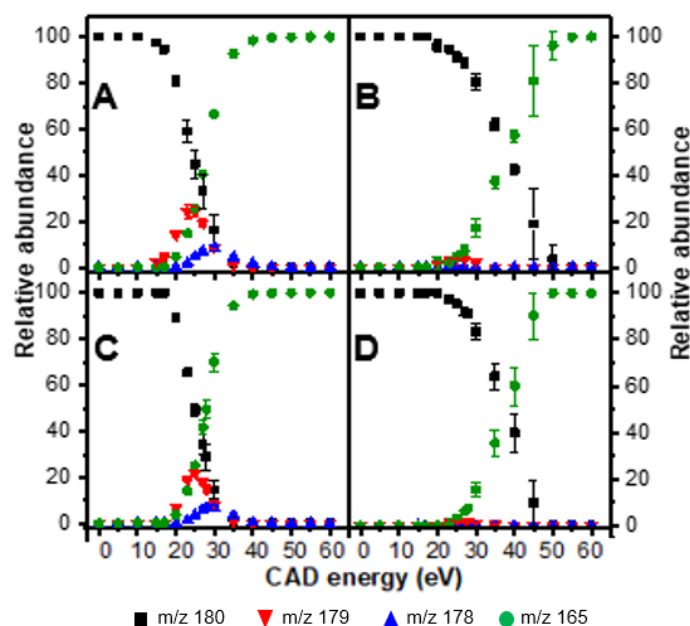
Figure 3.13 The ERMS ITCAD plots measured for ionized DHA at (A) low mass resolution and (B) at high mass resolution and for ionized DHP at (C) low mass resolution and (D) high mass resolution.

When the MS spectra A and B (Figure 3.14) with a mass range of 10 m/z units are compared, the ions of m/z 179, 180 and 181 have approximately equal abundance. When the MS spectra C and D (Figure 3.12) with a mass range of 250 m/z units are compared, the ions of m/z 167, 168, 179 and 181 have lower relative abundances or are undetected at high resolution when compared to measurements completed at low resolution.
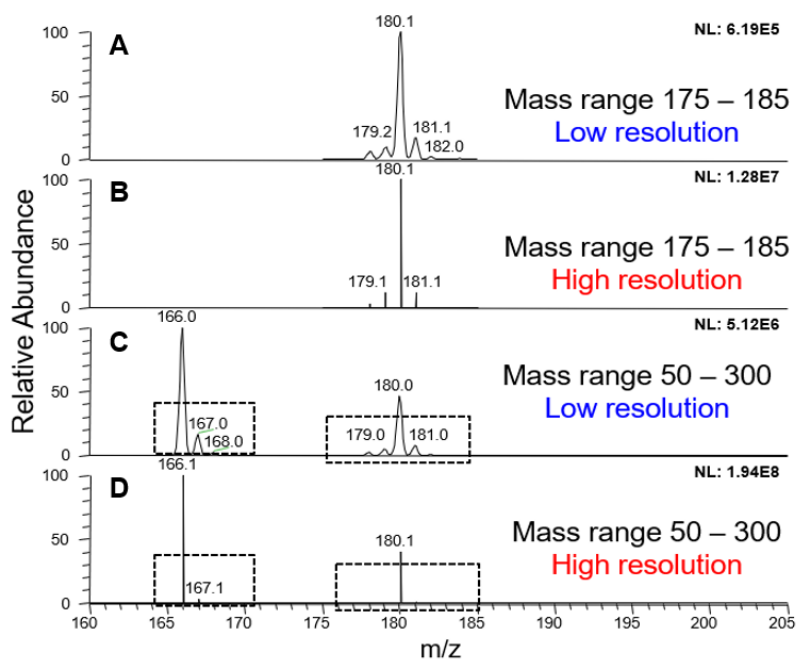
Figure 3.14 (A) MS spectra measured for ionized DHA by using a small mass range (A) at low resolution and (B) at high resolution (100,000). MS spectra measured for ionized fluorene and ionized DHA at a wider mass range (C) at low resolution and (D) at high resolution (100,000).

The high-resolution ERMS plots determined for ionized 1MF, 2MF, 3MF, 9MF DBP and TS subjected to ITCAD are presented in Figure 3.15. These plots look similar. The molecular ions fragmented predominantly by loss of a methyl radical to produce fragment ions of m/z 165. Fragment ions of m/z 179 and 178 have very low abundance or were undetected. Clearly, this approach was not effective at providing detailed structural information for the ionized isomers.
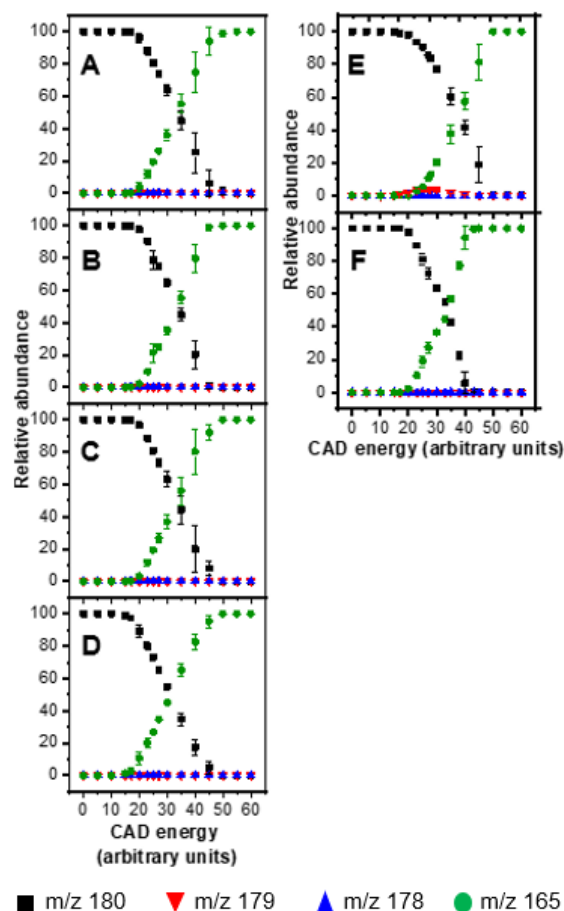
Figure 3.15 ITCAD ERMS plots measured at high resolution (100,000) for ionized 1MF (A), 2MF (B), 3MF (C), 9MF (D), TS (E), and DBP (F). The molecular ions fragment by loss of a methyl radical to produce fragment ions of m/z 165. For low-resolution ITCAD measurements performed for ionized TS, fragment ions of m/z 179 and 178 had a maximum relative abundance of 4.2 % and 1.0 %, respectively. When ionized 1MF, 2MF, 3MF, 9MF and DBP were subjected to low resolution ITCAD, the fragment ions of m/z 179 and 178 were not detected.

3.4   Conclusions

ERMS MCAD was shown to be superior over ERMS ITCAD at distinguishing ionized isomeric aromatic compounds and providing detailed structural information for the compounds. The modified crossing-point energies derived from the ERMS MCAD plots were reproducible and facilitated the distinction of six of the eight ionized isomers examined (1MF and 3MF were not distinguished.). This approach was shown to effectively distinguish between ionized compounds that contained a four- (DBP), five- (1MF, 2MF, 3MF and 9MF) or six-membered (DHA and DHP) naphthene ring or no naphthene ring (TS). The dominant dissociation pathways of ionized compounds were used to distinguish the different compound classes. For example, the six-membered naphthene-containing compounds dominant fragmentation pathway was loss of a H atom and the five-membered naphthene-containing compounds dominant fragmentation pathway was loss of a methyl radical. TS contained no naphthene ring and fragmented by loss of benzene.

MCAD was shown to impart greater internal energy into molecular ions than ITCAD, which facilitated the fragmentation of the molecular ions via higher-energy pathways. The additional fragmentation reactions were used to distinguish between the ionized isomers. The residence times for ions in MCAD and ITCAD experiments were in the microsecond and millisecond time regime, respectively. When molecular ions DHA, DHP and TS were subjected to MCAD, the dominant fragmentation pathway was loss of a hydrogen atom via σ-bond cleavage. When molecular ions DHA, DHP and TS were subjected to ITCAD, the major fragmentation pathway was loss of a methyl radical via a rearrangement reaction.

ERMS MCAD was shown to distinguish between the ionized six-membered naphthene-containing compounds (DHA and DHP) and TS from ionized DBP and the five-membered naphthene-containing compounds (1MF, 2MF 3MF and 9MF). ERMS ITCAD could not differentiate between ionized DHA, DHP and TS from each other, and 1MF, 2MF 3MF, 9MF and

DBP from each other. Hence, ITCAD measurements did not facilitate differentiation between a four- five- and six-membered naphthene-containing compounds, determination of the position of the methyl group or whether the compound contained a six-membered ring or no naphthene ring.

Further, the modified crossing-point energies derived from ERMS ITCAD plots were less reproducible when compared to ERMS MCAD measurements. Hence, the modified crossing-point energies could not be used to distinguish between DHA, DHP and TS, and between 1MF, 2MF, 3MF and 9MF and DBP.

When molecular ions were subjected to ITCAD and the ions were sent into the orbitrap for mass analysis, fragment ions were shown to be less abundant or not detected when compared to low-resolution measurements. The high-resolution measurements were considered less reliable at providing structural information and distinguishing the molecular ions when compared to the low-resolution measurements. At high resolution, the fragment ions of m/z 179 and 178 were undetected or had a relative abundance below 2 %. As a result, the high-resolution ERMS ITCAD plots for the isomeric ions looked essentially identical. . The dynamic range of the orbitrap may explain this limitation.

The results presented here demonstrate that MCAD can be used to distinguish between ionized isomeric aromatic ions and can provide more in-depth structural information for ionized compounds than ITCAD.

3.5   References

1. Cooks, R.G.; Busch, K.L.; Glish, G.L. Mass Spectrometry: Analytical Capabilities and Potentials. *Science* **1983**, *222* (4621), 273 – 291.

2. Amy, J.M., Baitinger, W.E., Cooks, R.G.: Building Mass Spectrometers and a Philosophy of Ressearch. *J. Am. Soc. Mass Spectrom.* **1990**, *1* (2), 119 – 128.

3. McLafferty, F.W. Tandem Mass Spectrometric Analysis of Complex Biological Mixtures *Int. J. Mass Spectrom.* **2001**, *212*, 81 – 87.

4. Vekey, K. Internal Energy Effects in Mass Spectrometry. *J Mass Spectrom.* **1996**, *31* (5), 445 – 463.

5. Wells, J.M.; McLuckey, S.A. Collision-induced dissociation (CID) of Peptides and Proteins. *Methods Enzymol.* **2005**, *402* (5), 148 – 185.

6. Xia, Y.; Liang, X.; McLuckey, S.A. Ion Trap Versus Low Energy Beam-type Collision-induced dissocation of Protonated Ubiquitin ions. *Anal. Chem.* **2006**, *78* (4), 1218 – 1227.

7. McLuckey, S.A.; Goeringer, D.E. Slow Heating Methods in Tandem Mass Spectrometry. *J. Mass Spectrom.* **1997**, *32* (5), 461 – 474.

8. Olsen, J.V.; Macek, B.; Lange, O.; Makarov, A.; Horning, S.; Mann, M. Higher-energy C-trap dissociation for Peptide Modification Analysis. *Nature Methods* **2007**, *4* (9), 709 – 712.

9. McAlister, G.C.; Phanstiel, D.H.; Brumbaugh, J.; Westphall, M.S.; Coon, J.J. Higher-energy Collision-activated dissociation without a Dedicated Collision Cell. *Mol. Cell. Proteomic* **2011**, 1 – 6.

10. McAlister, G.C.; Phanstiel, D.; Wenger, C.D.; Lee, M.V.; Coon, J.J. Analysis of Tandem Mass Spectra by FTMS for Improved Large-scale Proteomics with Superior Protein Quantification. *Anal. Chem.* **2010**, *82* (1), 316 – 322.

11. Nagaraj N.; D'Souza, R. C.; Cox, J.; Olsen, J.V.; Mann, M. Correction to Feasibility of Large-Scale Phosphoproteomics with High Energy Collisional Dissociation Fragmentation. *J. Proteome Res.* **2012**, *11* (6), 3506 – 3508.

12. Nagaraj N.; D'Souza, R. C.; Cox, J.; Olsen, J.V.; Mann, M. Feasibility of Large-Scale Phosphoproteomics with High Energy Collisional Dissociation Fragmentation. *J. Proteome Res*. **2010**, *9* (12), 6786 – 6794.

13. Jarrell, T.; Jin, C.; Riedeman, J.S.; Owen, B.C.; Tan, X.; Scherer, A.; Tykwinski, R.R.; Gray, M.R.; Slater, P.; Kenttämaa, H.I. Elucidation of Structural Information Achievable for Asphaltenes via Collision-activated Dissociation of their Molecular Ions in MS[n] Experiments: A Model Compounds Study. *Fuel* **2014**, *133*, 106 – 114.

14. Tang, W.; Hurt, M.R.; Sheng, H.; Riedeman, J.S.; Borton, D.J.; Slater, P.; Kenttämaa, H.I. Structural Comparison of Asphaltenes of Different Origins Using Multi-Stage Tandem Mass Spectrometry. *Energy Fuels* **2015**, *29* (3), 1309 – 1314.

15. Dong, X.; Zhang, Y.; Milton, J., Yerabolu, R.; Easterling, L.; Kenttämaa, H.I. Investigation of the Relative Abundances of Single Core and Multicore Compounds in Asphaltenes by Using In-Source Collision-activated dissociation and Medium-energy collision-activated dissociation with Statistic Considerations. Submitted to *Fuel.*

16. McLuckey, S.A.; Glish, G.L.; Cooks R.G. Kinetic Energy Effects in Mass Spectrometry using a Sector/Quadrupole Tandem Instrument. *Int. J. Mass, Spectrom. Ion Phys.* **1981**, *39* (2), 219 - 230.

17. Kustov, L.: Opening of the Rings of Aromatic and Naphthene Hydrocarbons: A New Way of Improving the Quality of Fuels. *Cataly Ind.* **2011**, *3* (4), 358 – 369.

18. McVicker, G. B.; Touvelle, M. S.; Hudson, C. W.; Vaughan, D. E. W.; Daage, M.; Hantzer, S.; Klein, D. P.; Ellis, E. S.; Cook, B. R.; Feeley, O. C.; and Baumgartner, J. E. U.S. Patent 5,763,731 (1998).

19. McVicker, G. B.; Schorfheide, J. J.; Baird, W. C. Jr.; Touvelle, M.; Daage, M.; Klein, D. P.; Ellis, E. S.; Vaughan, D. E. W.; Chen, J.; Hantzer, S. S. U.S. Patent 6,103,106 (2000).

20. McVicker, G.B.; Daage, M.; Touvelle, M.S.; Hudson, C.W.; Klein, D.P.; Baird, W.C. Jr.; Cook, B.R.; Chen, J.G.; Hantzer, S.; Vaughan, D.E.W.; Ellis, E.S.; Feeley, O.C. Selective Ring Opening of Naphthenic Molecules. *J. Catal.* **2002**, *210* (1), 137–148.

21. Owen, B.C.; Gao, J.; Borton, D.J.; Amundson, L.M.; Archibold, E.F.; Tan, X.; Azyat, K.; Tywinski, R.; Gray, M.; Kenttämaa, H.I. Carbon Disulfide Reagent Allows the Characcterization of Nonpolar Analytes by Atmospheric Pressure Chemical Ionization Mass Spectrometry. *Rapid Commun. Mass Spectrom.* **2011**, *5* (14), 1924 – 1928.

22. Ding, N.;Li, H.; Feng, X.;Wang, Q.;Li, S.W.;Ma, L.; Zhou, J.; Wang, B. . (2016). Partitioning MOF-5 into Confined and Hydrophobic Compartments for Carbon Capture under Humid Conditions. *J. Am. Chem. Soc.* **2016** *138* (32): 10100-10103.

23. de Oteyza, D. G., et al. (2013). Direct Imaging of Covalent Bond Structure in Single-Molecule Chemical Reactions. *Science* **340** (6139): 1434-1437.

24. Gaussian 16, Revision A.03, M. J. Frisch, G. W. Trucks, H. B. Schlegel, G. E. Scuseria, M. A. Robb, J. R. Cheeseman, G. Scalmani, V. Barone, G. A. Petersson, H. Nakatsuji, X. Li, M. Caricato, A. V. Marenich, J. Bloino, B. G. Janesko, R. Gomperts, B. Mennucci, H. P. Hratchian, J. V. Ortiz, A. F. Izmaylov, J. L. Sonnenberg, D. Williams-Young, F. Ding, F. Lipparini, F. Egidi, J. Goings, B. Peng, A. Petrone, T. Henderson, D. Ranasinghe, V. G. Zakrzewski, J. Gao, N. Rega, G. Zheng, W. Liang, M. Hada, M. Ehara, K. Toyota, R. Fukuda, J. Hasegawa, M. Ishida, T. Nakajima, Y. Honda, O. Kitao, H. Nakai, T. Vreven, K. Throssell, J. A. Montgomery, Jr., J. E. Peralta, F. Ogliaro, M. J. Bearpark, J. J. Heyd, E. N. Brothers, K. N. Kudin, V. N. Staroverov, T. A. Keith, R. Kobayashi, J. Normand, K. Raghavachari, A. P. Rendell, J. C. Burant, S. S. Iyengar, J. Tomasi, M. Cossi, J. M. Millam, M. Klene, C. Adamo, R. Cammi, J. W. Ochterski, R. L. Martin, K. Morokuma, O. Farkas, J. B. Foresman, and D. J. Fox, Gaussian, Inc., Wallingford CT, 2016.

25. Becke, A. D. Density-Functional Thermochemistry. III. The Role of Exact Exchange. *J. Chem. Phys*. **1993**, *98* (7), 5648 - 5652.

26. Lee, C.; Yang, W.; Parr, R. G. Development of the Colle-Salvetti Correlation-Energy Formula into a Functional of the Electron Density. *Phys. Rev. B: Cond. Matter Mat. Phys*. **1988**, *37* (2), 785− 789.

27. Perdew, J. P. Density-functional Approximation for the Correlation Energy of the Inhomogeneous Electron Gas. *Phys. Rev. B Cond. Matter Mat. Phys*. **1986**, *33* (12), 8822 - 8824.

28. Lazarou, Y. J.; Prosmitis, A.V.; Papadimitriou, V.C.; Papagiannakopoulos, P. Theoretical Calculation of Bond Dissociation Energies and Ethalpies of Formation for Halogenated Molecules *Phys. Chem. A* **2001**, 105 (27), 6729-6742.

29 Yao, X. J.; Hou, X.J.; Jiao, H.; Xiang, H.W.; Li, Y.W. Accurate Calculations of Bond Dissociation Enthalpies with Density Functional Methods. *J. Phys. Chem. A* **2003**, *107* (46), 9991-9996.

30 Feng, Y. J. Assessment of Experimental Bond Dissociation Energies Using Composite Ab Initio Methods and Evaluation of Performances of Density Functional Methods in the Calculation of Bond Dissociation Energies. *Chem. Inf. Comput. Sci.***2003**, *43* (6), 2005 - 2013.

31 Wiener, J.; Politzer, P. Comparison of various density functional methods for computing bond dissociation energies. **1998** *J. Mol. Struct. (Theochem)* 427 (1-3) 171 - 174

32. Verma, S.; Ciupek, J.D.; Cooks, R.G. Isomeric Structural Distinction Using Energy and Angular Resolution: $C_3H_6O^{+\bullet}$. *Int. J Mass Spectrom. Ion Processes* **1984**, *62 (2)*, 219 – 225.

33. Busch, K.L.; Glish, G.L.; McLuckey, S.A. *Mass Spectrometry / Mass Spectrometry Techniques and Applications of Tandem Mass Spectrometry*. New York: VCH Publishers Inc, 1988, print.

CHAPTER 4. CHEMICAL COMPOSITION ANALYSIS OF JET FUELS, DIESEL FUELS, FUEL BLENDING COMPONENTS, AND ALTERNATIVE JET AND DIESEL FUELS BY USING GCXGC/(EI)TOF MS

4.1 Introduction

Oil refineries distill crude oil at different temperatures to obtain distillate streams with unique chemical compositions that are used to produce different types of petroleum-derived fuels (*i.e.,* gasoline, jet fuel and diesel). For example, jet fuel is produced from a distillate obtained at temperatures between 150 °C and 270 °C, while diesel is produced from a distillate obtained at temperatures between 200 °C and 350 °C. The distillates contain many different types of compounds. They are further treated using various industrial processes (*i.e.,* Merox process) to remove unwanted components, including sulfur- and nitrogen-containing compounds, acids and metals. Additives, such as static inhibitors, may be added to the fuels to improve their performance. The final product is then tested using methods published by the American Society for Testing and Materials (ASTM) to determine whether the fuel meets the necessary physical and chemical properties (*i.e.,* density, viscosity and freezing point) that influence the performance of the vehicle combusting the fuel. Passage in these tests is required for any fuel to be used in the United States and thus newly developed alternative fuels must also meet these standards.

Since crude oil is a limited resource, the development of alternative fuels made from renewable resources via different chemical processes has been explored over the past several decades. For example, the Fischer-Tropsch catalytic process coverts coal, natural gas and biomass to a mixture of linear and branched alkanes with little aromatic content.[1-4] On the other hand, hydroprocessing esters and fatty acids originating from camelina, algae, jatropha and tallow also produces mixtures of linear and branched saturated hydrocarbons.[5,6] These sort of hydrocarbon

mixtures have been approved for use as fuel blending components for jet fuels because they require blending with at least 50 % by volume of a petroleum-based fuel to pass ASTM certification.[5,7-8]

Recently, Applied Research Associates (ARA) and Chevron Lummus Global have used a catalytic hydrothermal process to produce alternative jet and diesel fuel from the oil of plants, algae and animal material that require no blending with petroleum-based fuel.[9] Unlike the fuel blending components discussed above, the catalytic hydrothermal conversion jet (CHCJ) and catalytic hydrothermal conversion diesel (CHCD) fuels are 100 % drop-in ready and have comparable physical and chemical properties to those of petroleum-derived jet and diesel fuel.[9] Currently, these fuels have not been approved by ASTM.

Identifying the compounds in fuels, alternative fuels and fuel blending components is critically important because the chemical composition influences the physical and chemical properties of the fuels, including engine emissions, freezing point, viscosity, thermal stability and elastomeric swelling.[7,10-11] Knowledge of the chemical composition can also lead to a better understanding of how the composition influences these chemical and physical properties. Additionally, identifying both beneficial and harmful compounds in fuels may facilitate the development of future resilient fuels that are tailored to contain the beneficial compounds, not the harmful compounds. To determine the chemical composition of fuels, analytical instruments and techniques are required.

Currently, many analytical approaches are used to measure the chemical compositions of fuels. For example, fluorescent indicator absorption (FIA) is used to determine the volume percent of aromatic compounds,[12] ultraviolet spectroscopy is used to determine the mass percent of naphthalenes,[13] and X-ray fluorescence is used to determine the presence of sulfur-containing compounds.[14] However, each technique enables the determination of the amount of only one

specific class of compounds in fuels. Hence, the total analysis time is increased compared to the situation where only one method would provide all this information.

The aim of this work was to determine the chemical composition of approved jet fuels, approved alternative fuels, unapproved potential fuels and approved and unapproved diesel fuels by using GCxGC(EI)/TOF MS. The coupling of chromatography and mass spectrometry has facilitated the separation and detection of many volatile analytes in complex mixtures.[15,16] Identifying the chemical compositions of petroleum-derived jet fuels and determining how the composition influences the physical and chemical properties of the fuel is critically important to the development of resilient fuels for the future. An ancillary aim was to determine the GCxGC elution times of alkenes and heteroatom-containing compounds and examine whether these compounds coelute with hydrocarbons found in jet and diesel fuels. The alkenes and heteroatom-containing compounds are considered harmful compounds because they adversely affect fuel storage stability and contribute to emissions and particulate matter containing SO_2, which contributes to acid rain.[7,10] If harmful compounds have similar elution times as the beneficial saturated hydrocarbons, the harmful may be classified incorrectly when using GcxGC without mass spectrometric detection. Hence, it is important to compare the elution times of alkenes and heteroatom-containing compounds to those of saturated hydrocarbons to avoid incorrect classification when using GCxGC without mass spectrometric analysis.

4.2   Experimental

4.2.1   Chemicals

Th e linear hydrocarbons *n*-octane (98 % purity), *n*-decane (≥ 99 % purity), *n*-dodecane (≥ 99 % purity), *n*-tetradecane (≥ 99 % purity), *n*-pentadecane (≥ 99 % purity), *n*-hexadecane (99 % purity), *n*-heptadecane (99 % purity), *n*-octadecane (99 % purity), *n*-nonadecane (99 % purity), *n*-eicosane (99 % purity) and *n*-tetracosane (99 % purity) were purchased from Sigma Aldrich. The branched alkane 2,6,10,14-tetramethylpentadecane (> 95 % purity) was purchased from TCI, 2,2,4,4,6,8,8-heptamethylnonane (98 % purity) was purchased from Acros Organics, and 2-methylheptadecane (98 % purity) and 2,2,4,6,6-pentamethylheptane (99 % purity) were purchased from Sigma Aldrich. The cycloalkene 1,4-cyclohexadiene (97 % purity) and the alkenes 1-octene (98 % purity) and 1-octadecene (≥ 95 % purity) were purchased from Sigma Aldrich.

Th e alkybenzenes ethylbenzene (99 % purity), *m*-xylene (99 % purity), and *o*-xylene (99 % purity) were purchased from Alfa Aesar. *n*-Propylbenzene (98 % purity), isopropylbenzene (98 % purity), 1,3,5-trimethylbenzene (98 % purity), *n*-butylbenzene (≥ 99 % purity), *sec*-butylbenzene (≥ 99 % purity), *tert*-butylbenzene (99 % purity), 3-ethyltoluene (99 % % purity), 2-ethyltoluene (99 % purity), 1,2,4-trimethylbenzene (98 % purity), 1,2,3-trimethylbenzene (98 % purity), 1,3-diethylbenzene (≥ 99 % purity), hexamethylbenzene (99 % purity) and 1-phenylundecane (98 % purity) were purchased from Sigma-Aldrich.

The cycloalkanes *n*-butylcyclohexane (≥ 99 % purity), adamantane (≥ 99 % purity) isopropylcyclohexane (99 % purity) and *cis*-decahydronaphthalene (99 % purity) were purchased from Sigma Aldrich. *trans*-Decahydronaphthalene (≥ 99 % purity) was purchased from Fluka. Tetradecahydroanthracene (95 % purity) was purchased from Enamine. *n*-Hexylcyclohexane (98 %

purity) was purchased from Combi-Blocks and *n*-pentylcyclohexane (98 % purity) was purchased from Alfa Aesar.

Saturated ring-containing compounds tetralin (≥ 97 % purity) and 1,2,3,4,5,6,7,8-octahydroanthracene (purity not stated) were purchased from Sigma Aldrich and indane (95 % purity) was purchased from Acros. Cyclohexylbenzene (99.5 % purity) was purchased from Frontier Scientific.

Naphthalene was purchased from Fisher Scientific (certified grade). 1-Methylnaphthalene (95 % purity) and 2-ethylnaphthalene (≥ 99 % purity) were purchased from Sigma Aldrich.

-Compounds containing aromatic rings and C=C bonds, namely,4-methylstyrene (96 % purity), *trans*-β-methylstyrene (99% purity), allylbenzene (98 % purity) and 1,2-dihydronaphthalene (98 % purity) were purchased from Sigma Aldrich. *cis*-1-Propenylbenzene (95 % purity) and 1,1,4,4-tetramethyl-1,2,3,4-tetrahydronaphthalene (≥ 95 % purity) were purchased from Oakwood Chemical.

Polyaromatic compounds fluorene (98 % purity), 9-methylfluorene (purity not provided), 9,10-dihydroanthracene (97 % purity), 9,10-dihydrophenanthrene (94 % purity), and pyrene (98 % purity) were purchased from Sigma Aldrich while 2-methylfluorene (97 % purity) was purchased from AK Scientific and phenanthrene (97 % purity) and anthracene (99 % purity) from Acros Organics. 4-Ethylbiphenyl (97% purity) was purchased from Sigma Aldrich. Biphenyl (99 % purity) was purchased from Alfa Aesar.

Heteroatomic compounds quinolone (98 % purity), isoquinoline (97 % purity), indole (≥ 99 % purity), benzo[a]thiophene (98 % purity) and benzothiazole (96 % purity) were purchased from Sigma Aldrich.

Jet A, Sasol isoparaffinic kerosene (referred to as Sasol IPK) and Jet A mixed with HEFA (hydroprocessed esters and fatty acids) as a 50:50 (v/v) blend (referred to as Jet A / HEFA) were provided by Dr. Timothy James Edwards of the Wright-Patterson Air Force Base, Dayton, OH. Catalytic hydrothermal conversion jet (CHCJ) and catalytic hydrothermal conversion diesel (CHCD) fuels were provided by Dr. Luning Prak of the United States Naval Academy, Annapolis, MD. Petroleum-derived diesel was purchased from Go Low gas station in West Lafayette, IN. All compounds were used as received without additional purification.

4.2.2   Instrumentation and sample preparation

An Agilent 7890A GCxGC system coupled to a Pegasus-HRT 4D electron ionization (EI) time-of-flight (TOF) mass spectrometer (Leco Co., St Joseph, MI, USA) was utilized for the mass spectrometry measurements of all mixtures. To prepare these samples for chemical analysis, approximately 10 µL of CHCJ and CHCD, 12.0 µL of Jet A, Jet A/HEFA and diesel, and 8 µL of Sasol IPK were added individually into 2.0 mL of *n*-hexane. An Agilent G4513A auto injector was utilized to inject 0.5 µL of each sample solution into the GCxGC inlet system with a split ratio of 1:20. The inlet temperature was set to 260 °C for all measurements. Ultrapure helium carrier gas flowed constantly through the instrument at a rate of 1.25 mL/min. A reversed phase column configuration was used to separate the compounds in the samples. It consisted of a 60 m polar capillary column (Rxi-17Sil ms, Restek, Bellefonte, PA) in the primary oven and a 2 m nonpolar capillary column (Rxi-1 ms, Restek, Bellefonte, PA) in the enclosed secondary oven. Between the two columns, a quad-jet dual stage thermal modulator supplied heated and chilled nitrogen gas. The total modulator time was set to 5 s. This time was split between the first and second stages, each 2.5 s. The cold pulse time was set to 1.70 s and the hot pulse time was set to 0.80 s. The primary oven was set to 40 °C and the heat was ramped at a rate of 1 °C/min up to 232 °C where

it was held constant for 6 minutes. The secondary oven and the modulator hot jet temperature had + 10 °C and + 70 °C offsets, respectively, from that of the primary oven and the secondary oven, respectively. To increase the lifetime of the filament in the EI source, an acquisition delay of 400 s was employed to prevent ionization of the solvent (*n*-hexane). The ion source temperature was set to 250 °C. Electron kinetic energy of 70 eV was used to ionize the analytes. The ionized analytes were guided into a folded-flight-path TOF mass spectrometer (flight length 20 m). The resolution was ≥ 25,000. The mass spectra were collected at an acquisition rate of 200 Hz. The detector voltage was set to 1,750 V.

Approximately 1.0 µL or 1.0 mg of each neat model compound was diluted in 5.0 mL of *n*-hexane to produce a stock solution. The stock solution was diluted by a factor of 5 with *n*-hexane. This mixture was injected into the GCxGC/(EI) TOF MS. The elution times of the analytes were recorded and were compared to the elution times of the unknown compounds in the fuels, fuel blending components and potential fuels. The EI mass spectra measured for the unknown eluted compounds were compared to mass spectra in the Peak Find and Library Match Wiley (2011) and NIST (2011) databases to facilitate the identification of the unknown compounds. To assign qualitative regions for n-alkanes, cycloalkanes, alkylbenzenes and naphthalenes in two-dimensional total ion current chromatograms, elution times for known compounds representative of each class were measured.

4.3   Results and Discussion

The aim of this work was to determine the chemical composition of petroleum-based jet and diesel fuels, alternative fuels, and fuel blending components by using a GCxGC(EI)/TOF MS. The fuels measured include Jet A, petroleum-based diesel, CHCJ, CHCD, Sasol isoparaffinic kerosene

(Sasol IPK) and a 50:50 (v/v) blend of Jet A and hydroprocessed esters and fatty acids (Jet A / HEFA). An additional aim was to determine the elution times for several alkene and heteroatomic-containing compounds to determine if these compounds elute in boundaries distinctive from that of elution boundaries assigned to hydrocarbons (*i.e.,* alkane and cycloalkane compound classes).

The compounds in fuels and fuel blending components were first classified into one of three major categories, alkanes, cycloalkanes and aromatic compounds by using qualitative elution boundaries. The boundaries were determined based on the elution times measured for fifty known compounds belonging to one of the three major classes (Figure 4.1).

To perform preliminary identification of the compounds in the fuel samples, a mixture composed of sixty-six hydrocarbons was injected into the GCxGC/(EI)TOF MS, the primary and secondary elution times of the hydrocarbons were determined (Table 4.1), and their elution times were compared to those of the compounds in the fuel samples. The sixty-six hydrocarbons were classified into one of nine chemical groups: linear alkanes, branched alkanes, cycloalkanes, alkenes and cycloalkenes, alkylbenzenes, saturated ring-containing aromatic compounds, naphthalenes, polyaromatic compounds and aromatic compounds containing C=C bonds. For the total ion current (TIC) 2D-chromatogram measured for the sixty-six compounds, please see Figure 4.2. The numerical codes in the TIC chromatogram (Figure 4.2) represent the compounds listed in Table 4.1.
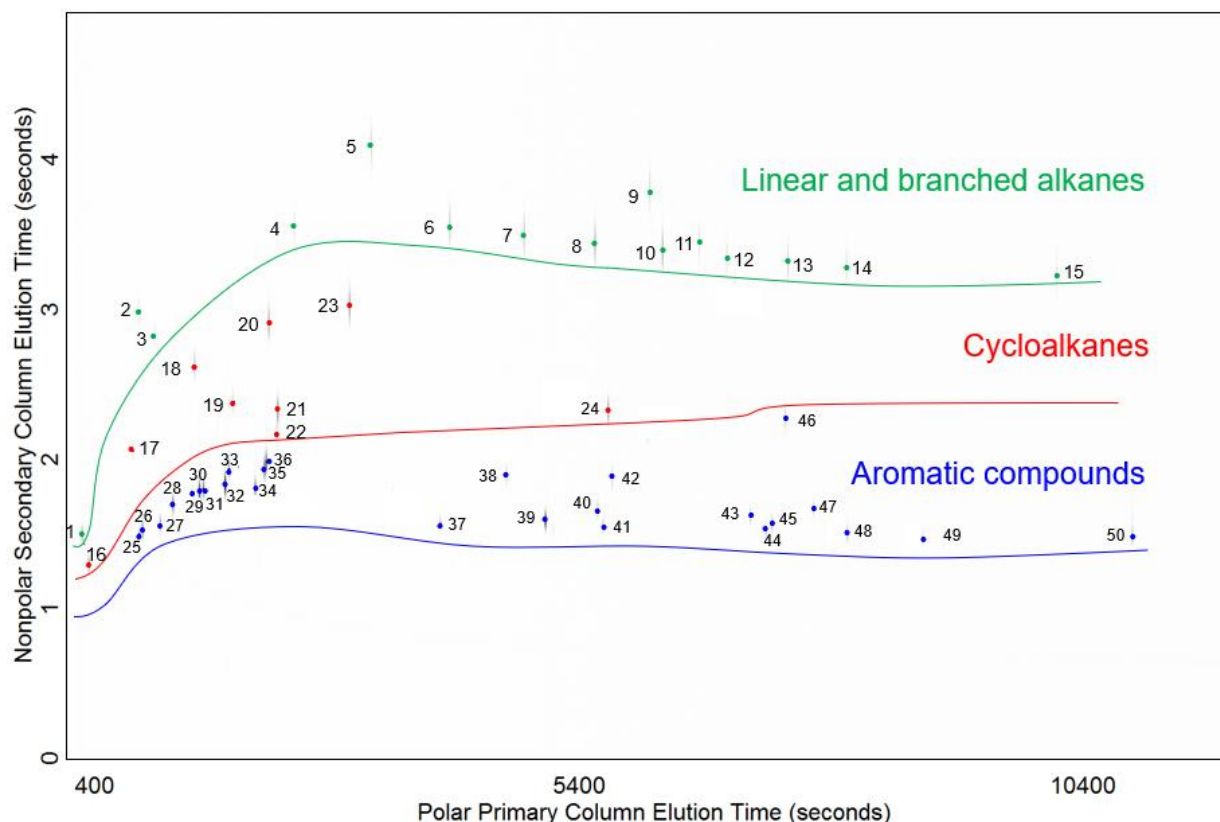
Figure 4.1 Qualitative elution regions for alkane, cycloalkane and aromatic compounds. The identity of the compounds is as follows: *n*-octane **1**, 2,2,4,6,6-pentamethylheptane **2**, *n*-decane **3**, *n*-dodecane **4**, 2,2,4,4,6,8,8-heptamethylnonane **5**, *n*-tetradecane **6**, *n*-pentadecane **7**, *n*-hexadecane **8**, 2,6,10,14-tetramethylpentadecane **9**, *n*-heptadecane **10**, 2-methylheptadecane **11**, *n*-octadecane **12**, n-nonadecane **13**, *n*-eicosane ($C_{20}H_{42}$) **14**, *n*-tetracosane ($C_{24}H_{50}$) **15**, 1-methylcyclohexane **16**, isopropylcyclohexane **17**, n-butylcyclohexane **18**, trans-decahydronaphthalene **19**, *n*-pentylcyclohexane **20**, adamantane **21**, *cis*-decahydronaphthalene **22**, *n*-hexylcyclohexane **23**, tetradecahydroanthracene **24**, ethylbenzene **25**, *m*-xylene **26**, *o*-xylene **27**, isopropylbenzene **28**, *n*-propylbenzene **29**, 3-ethyltoluene **30**, 1,3,5-trimethylbenzene **31**, 1,2,4-trimethylbenzene **32**, *sec*-butylbenzene **33**, 1,2,3-trimethylbenzene **34**, 1,3-diethylbenzene **35**, *n*-butylbenzene **36**, naphthalene **37**, 1,1,4,4-tetramethyl-1,2,3,4-tetrahydronaphthalene **38**, 1-methylnaphthalene **39**, 2-ethylnaphthalene **40**, biphenyl **41**, hexamethylbenzene **42**, 4-ethylbiphenyl **43**, fluorene **44**, 9-methylfuorene **45**, 1-phenyldecane **46**, 2-methylfluorene **47**, 9,10-dihydroanthracene **48**, anthracene **49**, and pyrene **50**.
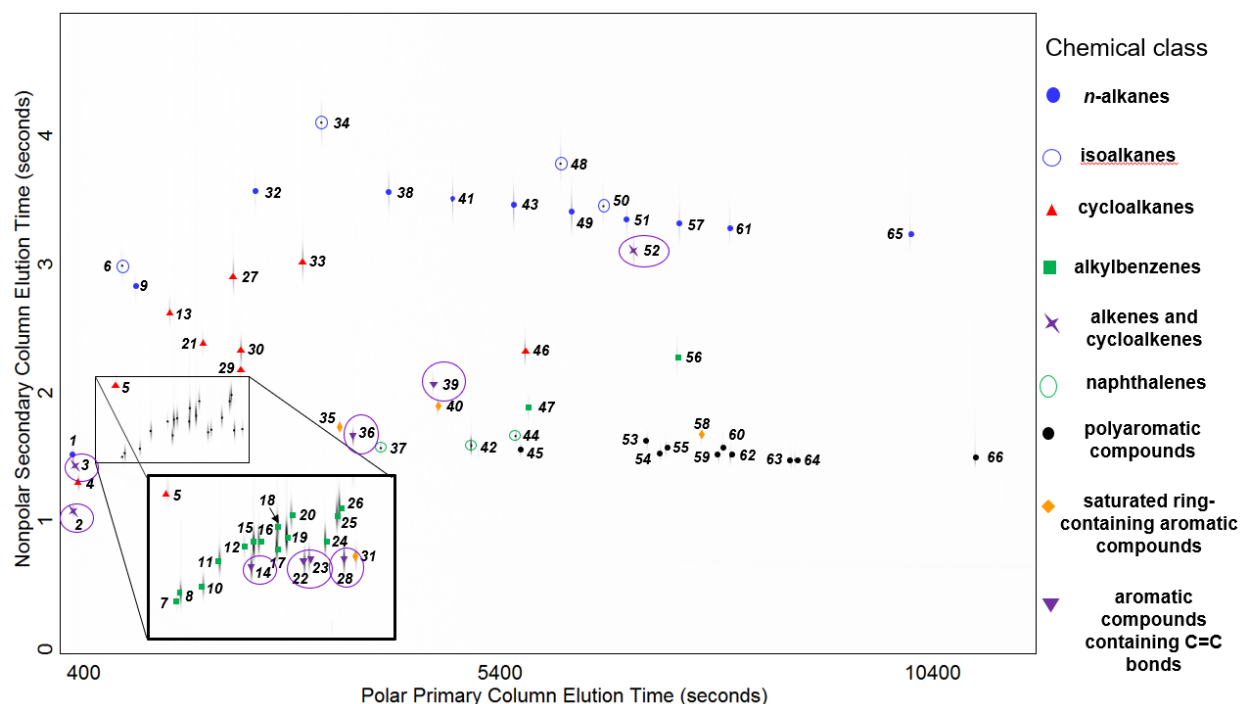
Figure 4.2 Total ion current (TIC) 2D-chromatogram for a mixture of known compounds measured by using GCxGC/(EI)TOF MS. The color code to the right of the TIC chromatogram corresponds to the different classes of the compounds in this mixture and the numbered assigned to each peak corresponds to the numerical indicator in Table 4.1 that identifies the compound.

4.3.1 Chemical compositions of jet fuel, diesel fuel, alternative fuel, and fuel blending components

The chemical composition of petroleum-based Jet A, an approved aviation fuel, differs from that of the potential alternative fuel CHCJ (Figure 4.3 and Tables 4.2 and 4.3) in that small alkanes, cycloalkanes, and aromatic compounds (such as *n*-octane, isopropylcyclohexane, ethylbenzene, and *m*- and *o*-xylenes) are present in Jet A and absent in CHCJ. The absence of small hydrocarbons in CHCJ suggests that this fuel may be less volatile than Jet A. Jet fuels with lower volatility are considered safer for ground crew personnel working on aircraft carriers for two

main reasons: first, less volatile fuels have a decreased risk of fire, and second, volatile organic compounds found in fuels are correlated with an increased risk of lung cancer.[17-19]

The presence of large linear alkanes significantly affect multiple fuel properties, such as the freezing point.[20] The largest linear alkane detected in Jet A was *n*-octadecane that eluted from the primary column at 6858.53 s. The largest linear alkane detected in CHCJ was *n*-pentadecane that eluted from the primary column at 4848.99 s. The presence of larger linear alkanes in Jet A would be expected to contribute to a higher freezing point compared to CHCJ. Indeed, the freezing points for Jet A and CHCJ were measured to be - 40 ºC and - 44 ºC, respectively, by using ASTM D2386 method). Therefore, an aircraft flying at high altitudes and/or cold temperatures may perform better when using CHCJ instead of Jet A because the large linear alkanes in Jet A will crystalize in the fuel lines than smaller alkanes.

Upon combustion, large aromatic compounds with multiple aromatic rings (*e.g.,* naphthalenes) generate more soot than alkylbenzenes and saturated ring-containing aromatic compounds (*e.g.*, tetralin).[21] Greater soot accumulation in aircraft engines requires increased maintenance efforts.[22] The largest aromatic compounds identified in Jet A and CHCJ elute from the primary column at 7358.42 s and 6143.69 s, respectively and were classified as polyaromatic compounds and saturated ring-containing aromatic compounds, respectively. For example, polyaromatic compounds. fluorene and 4-ethylbiphenyl elute from the primary column at 7248.44 s and 7118.47, respectively, and were identified in Jet A but not in CHCJ. Based on the elution times and analysis of the EI mass spectra, Jet A contains more compounds with multiple aromatic rings than CHCJ. This finding suggests that CHCJ may contribute to less soot production upon combustion than Jet A. Combustion studies of Jet A and CHCJ should be pursued to determine whether soot production and total emissions differ for these two fuels.

The smallest aromatic compounds detected in Jet A and CHCJ are alkylbenzenes with molecular weights (MW) of 106 Da and 120 Da, respectively (Figure 4.3) For example, ethylbenzene, *o*-xylene and *m*-xylene elute from primary column at 1034.86 s, 1064.85 s and 1239.81 s, respectively and were identified in Jet A, but not CHCJ. The smallest alkylbenzene detected in CHCJ was *n*-propylbenzene with an elution time of 1559.74 from the primary column. The of small alkylbenzenes in CHCJ may contribute to a lower efficiency to swell o-ring seals compared to Jet A.[23] For example, ethylbenzene (MW 106 Da) has been shown to swell o-rings more effectively than larger alkylbenzenes.[23] Inadequate swelling of o-ring seals may result in leaks in the fuel circulation systems of an aircraft.[7] To test this hypothesis, nitrile o-ring seals were immersed individually in Jet A and CHCJ. Indeed, the volume swell percent values for o-ring seals attributed to Jet A and CHCJ were 6.6 ± 0.4 % and 5.5 ± 0.3 %, respectively (see chapter five for a detailed description of the o-ring study).
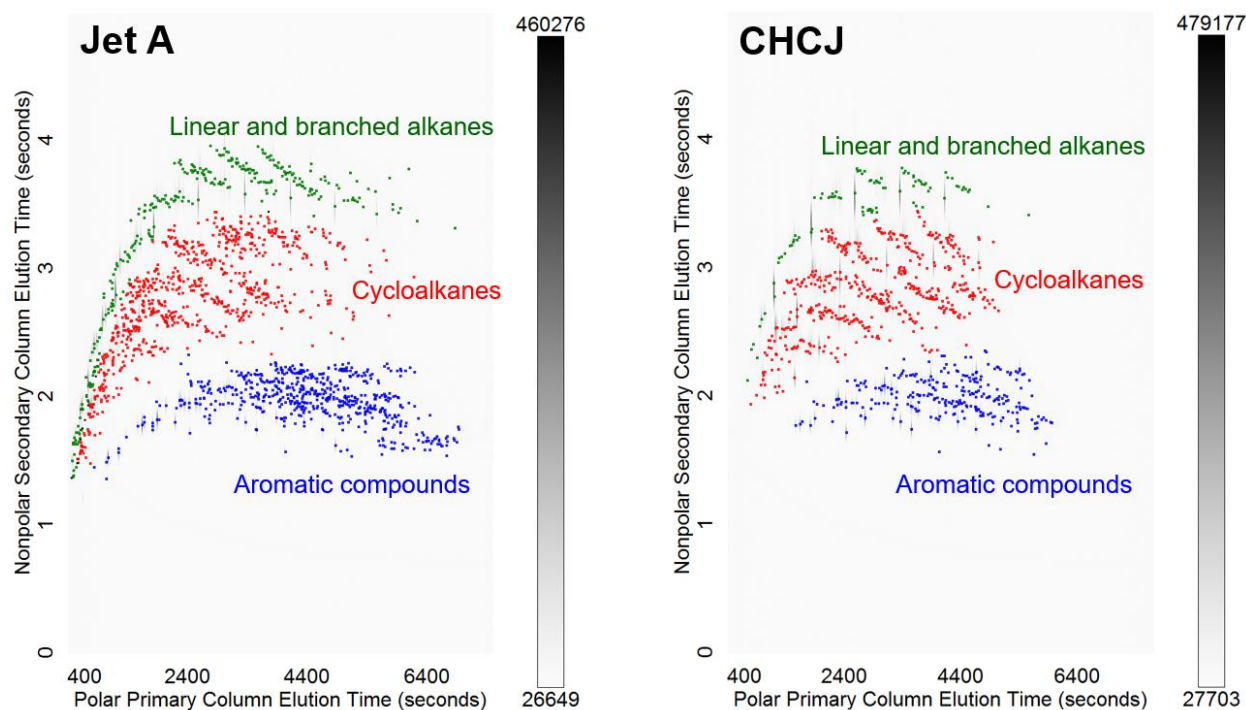
Figure 4.3 The total ion current (TIC) chromatograms measured for Jet A (left) and CHCJ (right).

The compounds identified in Jet A were also identified in the approved Jet A / HEFA fuel, as expected (Table 4.6). One of the major differences between Jet A / HEFA compared to neat Jet A was the presence of heavily branched alkanes with elution times ranging from approximately 4100 s up to 6200 s (Figures 4.3 and 4.4). These compounds are components of HEFA (Figure 4.5). These branched alkanes may suppress the freezing point of Jet A / HEFA below that of neat Jet A.

The fuel blending component Sasol IPK was found to be mostly composed of branched alkanes and linear alkanes (Figure 4.3 and Table 4.7). The largest linear alkane detected in Sasol IPK was *n*-tetradecane that eluted from the primary column at 4109 s. in comparison to octadecane detected in Jet A. The absence of larger linear alkanes in Sasol IPK is expected to decrease the freezing point compared to Jet A. Indeed, the freezing points measured for Sasol IPK and Jet A were ≤ -70 °C and – 40 °C, respectively (ASTM D2386 method).

Sasol IPK contains significantly fewer aromatic compounds than in Jet A (Figures 4.3 and 4.4) Further, the total aromatic content by mass in Sasol IPK was 0.3 % as determined by GCxGC FID, which is below the minimum standard set by Defense Standard 91-91. Hence, Sasol IPK has to be blended with a petroleum-based fuel to meet the standards set by ASTM. For example, the lack of aromatic compounds in Sasol IPK has been found to result in unsuccessful swelling of elastomeric seals[23] which may result in leaks in the fuel circulation system (see chapter 5).
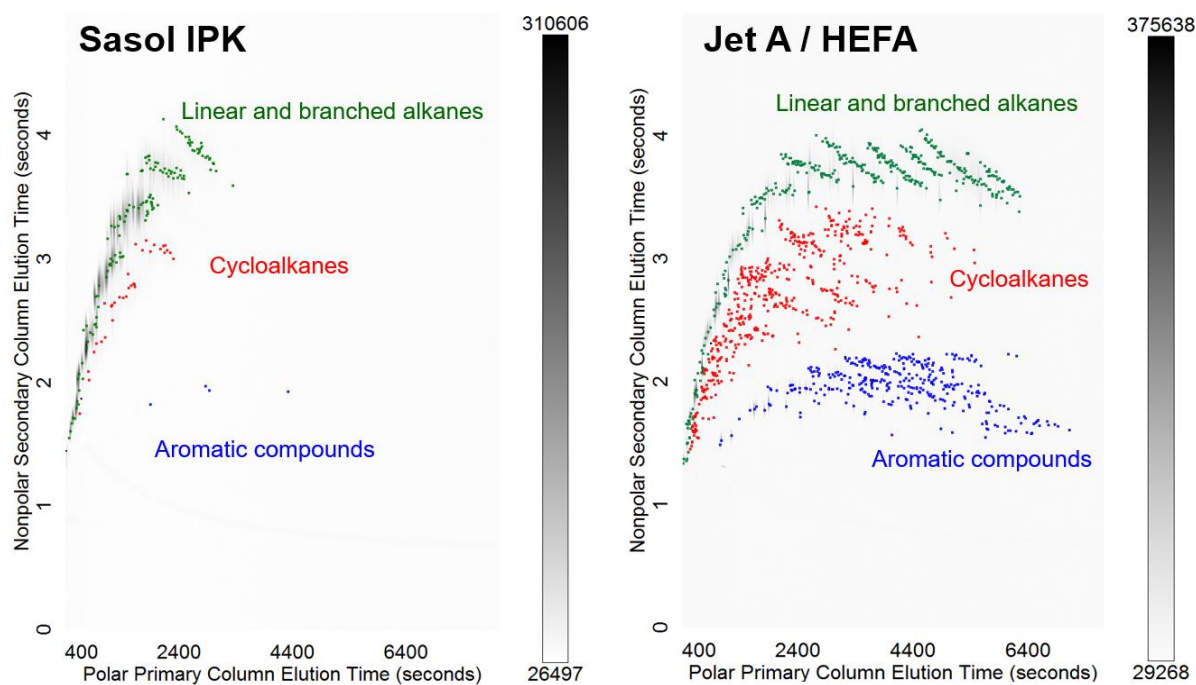
Figure 4.4 The total ion current chromatograms measured for Sasol IPK (left) and Jet A / HEFA (right).
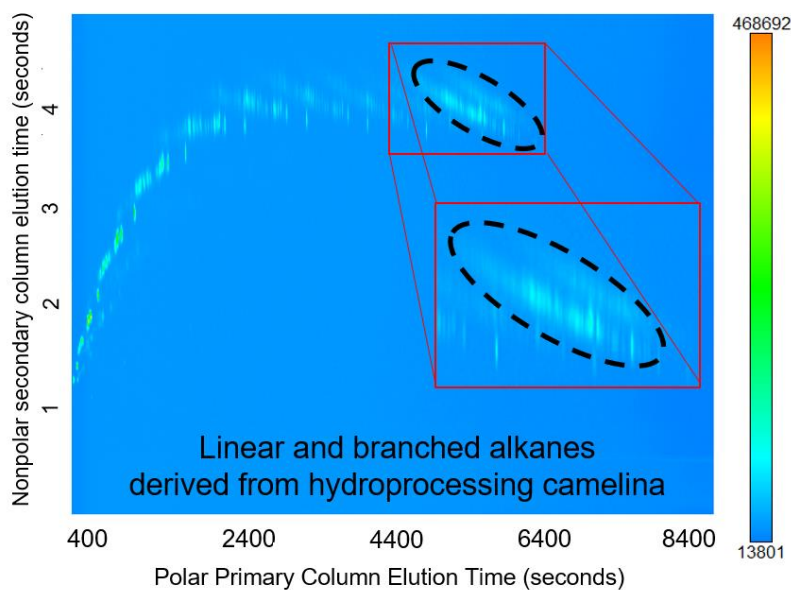
Figure 4.5 The total ion current chromatogram measured for neat HEFA derived from camelina. Located in the black dotted oval are branched alkanes that were also detected in the 50:50 (v/v) blend of Jet A and HEFA, but not in neat Jet A. The region was expanded for easier viewing.

The chemical composition of petroleum-based diesel fuel differs from that of CHCD (Figure 4.6 and Tables 4.6 and 4.7). The lightest and largest linear alkane detected in the diesel were n-octane and *n*-tetracosane, respectively eluting from the primary column at 464.99 s and 10127.80 seconds, respectively. However, the smallest and largest linear alkanes detected in CHCD were n-nonane and *n*-octadecane, respectively, eluting from the primary column at 729.93 s and 6863.53 s, respectively. Due to the presence of heavier linear alkanes in the diesel, its freezing point is likely greater than that of CHCD.

The smallest aromatic compounds detected in the diesel were alkylbenzenes eluting from the primary column at 1034 s or later. These compounds were determined to have a molecular weight of 106 Da and therefore, they correspond to compounds such as ethylbenzene and o- and m-xylenes. On the other hand, the smallest aromatic compounds detected in CHCD were alkylbenzenes eluting from the primary column at 1559 s or later. They were determined to have a molecular weight of 120 Da. Therefore, they correspond to compounds such as *n*-propylbenzene and 3-ethyltoluene. The absence of the smallest alkylbenzenes in CHCD may result in a greater vaporization temperature when compared to the diesel.[24]

Polycyclic aromatic hydrocarbons released into the atmosphere have been found to be carcinogenic, mutagenic and teratogenic.[25] The diesel fuel was shown to contain more polycyclic aromatic hydrocarbons than CHCD (Figure 4.6). Based on the elution times and analysis of the measured EI mass spectra, the the largest aromatic compounds in the diesel contain three or four fused benzene rings. For example, phenanthrene and pyrene elute from the primary column at 8753.10 s and 10882.68s, respectively, and were detected in the diesel (Table 4.6). On the other hand, based on elution times and analysis of the measured EI mass spectra, the largest aromatic compounds in CHCD contain only two benzene rings. Hence, individuals who regularly come in

contact with the diesel fuel may have more adverse health effects than individuals dealing with CHCD.

.
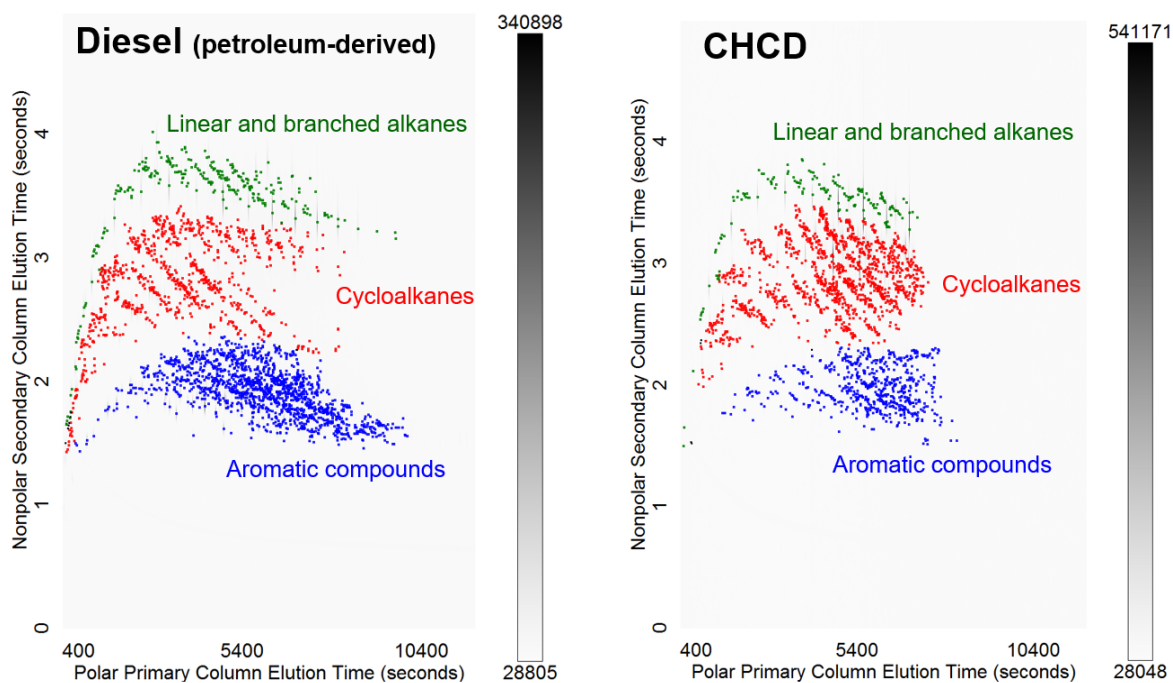
Figure 4.6 The total ion current chromatograms measured for petroleum-based diesel fuel (left) and CHCD (right).

Table 4.1 Elution times from the primary polar and secondary nonpolar columns and the numerical indicators for the compounds in the total ion current chromatogram shown in Figure 1 are reported. Compounds are classified into nine groups: n-alkanes, branched alkanes, alkenes and dienes, cycloalkanes, cycloalkenes, alkylbenzenes, naphthene-containing aromatic compounds, naphthalenes, multi-ring aromatic compounds and alkene-containing aromatic compounds.

Compound	Elution time polar column (s)	Elution time nonpolar column (s)	Numerical indicator
n-alkanes			
n-octane	459.99	1.507	1
n-decane	1189.82	2.808	9
n-dodecane	2574.51	3.538	32
n-tetradecane	4109.16	3.549	38
n-pentadecane	4843.99	3.497	41
n-hexadecane	5548.83	3.435	43
n-heptadecane	6218.68	3.363	49
n-octadecane	6853.53	3.322	51
n-nonadecane	7463.39	3.281	57
n-eicosane	8043.26	3.214	61
n-tetracosane	10167.80	3.139	65
branched alkanes			
2,2,4,6,6-pentamethylheptane	1029.86	2.973	6
2,2,4,4,6,8,8-heptamethylnonane	3344.33	4.068	34
2,6,10,14-tetramethylpentadecane	6113.70	3.749	48
2-methylheptadecane	6608.59	3.399	50
alkenes and cycloalkenes			
1,4-cyclohexadiene	464.99	1.085	2
1-octene	484.98	1.430	3
1-octadecene	6933.51	3.090	52
cycloalkanes			
1-methylcyclohexane	524.97	1.301	4
Isopropylcyclohexane	964.87	2.057	5
n-butylcyclohexane	1584.73	2.613	13
trans-decahydronaphthalene	1964.65	2.371	21
n-pentylcyclohexane	2314.56	2.911	27
adamantane	2399.55	2.170	29
cis-decahydronapthalene	2399.55	2.330	30
n-hexylcyclohexane	3114.38	3.039	33
tetradecahydroanthracene	5653.80	2.319	46
alkylbenzenes			
ethylbenzene	1034.86	1.491	7
m-xylene	1059.85	1.538	8

Table 4.1 continued

o-xylene	1234.81	1.574	10
isopropylbenzene	1364.78	1.702	11
n-propylbenzene	1559.74	1.764	12
3-ethyltoluene	1624.72	1.779	15
1,3,5-trimethylbenzene	1664.71	1.815	16
2-ethyltoluene	1804.68	1.779	17
tert-butylbenzene	1809.68	1.882	18
1,2,4-trimethylbenzene	1879.66	1.831	19
sec-butylbenzene	1919.65	1.944	20
1,2,3-trimethylbenzene	2179.60	1.810	24
1,3-diethylbenzene	2269.58	1.944	25
n-butylbenzene	2289.57	1.985	26
hexamethylbenzene	5738.79	1.857	47
1-phenylundecane	7463.39	2.237	56
saturated ring -containing			
compounds			
indane	2429.54	1.707	31
tetralin	3554.28	1.728	35
cyclohexylbenzene	4684.03	1.877	40
1,2,3,4,5,6,7,8-octahydroanthracene	7713.34	1.672	58
naphthalenes			
naphthalene	4029.18	1.558	37
1-methylnapthalene	5058.94	1.594	42
2-ethylnapthalene	5593.82	1.648	44
aromatic compounds containing			
more than one benzene ring			
biphenyl	5648.81	1.537	45
4-ethylbiphenyl	7113.47	1.599	53
fluorene	7243.44	1.527	54
9-methylfluorene	7303.43	1.564	55
9,10-dihydroanthracene	7913.29	1.512	59
2-methylfluorene	7963.28	1.568	60
9,10-dihydrophenanthrene	8053.26	1.496	62
phenanthrene	8753.10	1.471	63
anthracene	8803.09	1.481	64
pyrene	10882.60	1.476	66
C=C containing aromatic			
compounds			
allylbenzene	1609.73	1.671	14
cis-1-propenylbenzene	2019.63	1.702	22
4-methylstyrene	2054.62	1.718	23
trans-β-methylstyrene	2324.56	1.718	28

Table 4.1 continued

1,2-dihydronaphthalene	3694.25	1.656	36
1,1,4,4-tetramethyl-1,2,3,4-tetrahydronaphthalene	4634.04	2.067	39

Table 4.2 Compounds identified in Jet A by using GCxGC/(EI)TOF MS.

Compound	Elution time polar column (s)	Elution time nonpolar column (s)
n-alkanes		
n-octane	459.97	1.507
n-decane	1189.82	2.796
n-dodecane	2569.51	3.538
n-tetradecane	4109.16	3.554
n-pentadecane	4848.99	3.492
n-hexadecane	5548.83	3.430
n-heptadecane	6218.68	3.373
n-octadecane	6853.53	3.317
cycloalkanes		
isopropylcyclohexane	959.873	2.071
n-butylcyclohexane	1579.73	2.628
n-pentylcyclohexane	2314.56	2.916
trans-decahydronapthalene	1964.64	2.381
adamantine	2394.55	2.182
cis-decahydronapthalene	2404.54	2.332
n-hexylcycloalkane	3114.38	3.039
alkylbenzenes		
ethylbenzene	1034.86	1.497
m-xylene	1064.85	1.527
o-xylene	1239.81	1.569
isopropylbenzene	1364.78	1.702
n-propylbenzene	1559.74	1.774
3-ethyltoluene	1629.72	1.785
1,3,5-trimethylbenzene	1669.71	1.805
2-ethyltoluene	1804.68	1.800
1,2,4-trimethylbenzene	1879.66	1.836
sec-butylbenzene	1924.65	1.934
1,2,3-trimethylbenzene	2184.59	1.805
n-butylbenzene	2294.57	1.975
saturated ring -containing compounds		
indane	2424.54	1.718
tetralin	3544.29	1.743
cyclohexylbenzene	4689.03	1.898

Table 4.2 continued

naphthalenes		
naphthalene	4019.18	1.574
1-methylnapthalene	5053.94	1.589
2-ethylnaphthalene	5578.82	1.661
aromatic compounds containing more than one benzene ring		
biphenyl	5633.81	1.553
4-ethylbiphenyl	7118.47	1.625
fluorene	7248.44	1.533

Table 4.3 Compounds identified in CHCJ 10218 by using GCxGC/(EI)TOF MS.

Compound	Elution time polar column (s)	Elution time nonpolar column (s)
n-alkanes		
n-decane	1184.82	2.793
n-dodecane	2569.51	3.585
n-tetradecane	4109.16	3.559
n-pentadecane	4848.99	3.482
cycloalkanes		
n-butylcyclohexane	1584.73	2.618
trans-decahydronapthalene	1964.64	2.386
n-pentylcycloalkane	2319.56	2.911
cis-decahydronapthalene	2404.54	2.330
n-hexylcycloalkane	3119.38	3.003
alkylbenzenes		
n-propylbenzene	1559.74	1.774
3-ethyltoluene	1629.72	1.785
1,3,5-trimethylbenzene	1669.71	1.805
2-ethyltoluene	1809.68	1.774
1,2,4-trimethylbenzene	1884.66	1.826
sec-butylbenzene	1924.65	1.934
1,2,3-trimethylbenzene	2184.59	1.805
n-butylbenzene	2294.57	1.980
saturated ring-containing compounds		
indane	2424.54	1.718
tetralin	3544.29	1.738
cyclohexylbenzene	4689.03	1.893
naphthalenes		
naphthalene	4019.18	1.569
1-methylnapthalene	5058.94	1.589
2-ethylnaphthalene	5578.82	1.656
aromatic compounds containing more than one benzene ring		
biphenyl	5633.81	1.553

Table 4.4 Compounds identified in a 50:50 (v/v) blend of Jet A / HEFA by using GCxGC/(EI)TOF MS.

Compound	Elution time polar column (s)	Elution time nonpolar column (s)
n-alkanes		
n-octane	459.988	1.507
n-decane	1189.82	2.829
n-dodecane	2564.51	3.559
n-tetradecane	4109.16	3.564
n-pentadecane	4848.99	3.487
n-hexadecane	5548.83	3.446
n-heptadecane	6218.68	3.384
n-octadecane	6853.53	3.316
cycloalkanes		
isopropylcyclohexane	959.873	2.067
n-butylcyclohexane	1579.73	2.633
n-pentylcyclohexane	2314.56	2.926
trans-decahydronapthalene	1959.65	2.391
cis-decahydronapthalene	2404.54	2.317
n-hexylcycloalkane	3114.38	3.055
alkylbenzenes		
ethylbenzene	1034.86	1.502
m-xylene	1059.85	1.538
o-xylene	1234.81	1.575
isopropylbenzene	1364.78	1.707
n-propylbenzene	1554.74	1.774
3-ethyltoluene	1629.72	1.785
1,3,5-trimethylbenzene	1669.71	1.805
2-ethyltoluene	1804.68	1.785
1,2,4-trimethylbenzene	1884.66	1.826
sec-butylbenzene	1919.65	1.944
1,2,3-trimethylbenzene	2179.60	1.810
n-butylbenzene	2289.57	1.985
saturated ring-containing compounds		
indane	2424.54	1.718
tetralin	3544.29	1.742
cyclohexylbenzene	4689.03	1.895
naphthalenes		
naphthalene	4014.18	1.579
1-methylnapthalene	5058.94	1.599

Table 4.4 continued

2-ethylnaphthalene	5573.82	1.672
aromatic compounds containing more than one benzene ring		
Biphenyl	5633.81	1.553

Table 4.5 Compounds identified in Sasol IPK by using GCxGC/(EI)TOF MS.

Compound	Elution time polar column (s)	Elution time nonpolar column (s)
n-alkanes		
n-octane	459.988	1.507
n-dodecane	2564.51	3.559
n-tetradecane	4109.16	3.564
alkylbenzenes		
m-xylene	1059.85	1.538
1,2,4-trimethylbenzene	1884.66	1.826

Table 4.6 Compounds identified in petroleum-based diesel by using GCxGC/(EI)TOF MS.

Compound	Elution time polar column (s)	Elution time nonpolar column (s)
n-alkanes		
n-octane	464.99	1.505
n-decane	1189.82	2.813
n-dodecane	2569.51	3.549
n-tetradecane	4109.16	3.554
n-pentadecane	4848.99	3.482
n-hexadecane	5553.83	3.420
n-heptadecane	6218.68	3.363
n-octadecane	6858.53	3.329
n-nonadecane	7463.39	3.297
n-eicosane	8043.26	3.276
n-tetracosane	10127.80	3.220
cycloalkanes		
isopropylcyclohexane	964.87	2.061
n-butylcyclohexane	1584.73	2.628
trans-decahydronapthalene	1964.64	2.381
n-pentylcycloalkane	2319.56	2.916
cis-decahydronapthalene	2404.54	2.332
n-hexylcycloalkane	3119.38	3.029
tetradecahydoanthracene	5683.80	2.314
alkylbenzenes		
ethylbenzene	1034.86	1.497
m-xylene	1064.85	1.527
o-xylene	1239.81	1.563

Table 4.6 continued

isopropylbenzene	1369.78	1.697
n-propylbenzene	1559.74	1.769
3-ethyltoluene	1629.72	1.779
1,3,5-trimethylbenzene	1669.71	1.805
2-ethyltoluene	1809.68	1.774
1,2,4-trimethylbenzene	1884.66	1.826
sec-butylbenzene	1924.65	1.934
1,2,3-trimethylbenzene	2184.59	1.810
n-butylbenzene	2294.57	1.985
saturated ring-containing		
compounds		
indane	2424.54	1.718
tetralin	3544.29	1.743
cyclohexylbenzene	4689.03	1.898
1,2,3,4,5,6,7,8-octahydroanthracene	7718.34	1.666
naphthalenes		
naphthalene	4019.18	1.574
1-methylnapthalene	5058.94	1.589
2-ethylnaphthalene	5578.82	1.661
aromatic compounds containing		
more than one benzene ring		
biphenyl	5633.81	1.553
4-ethylbiphenyl	7118.47	1.625
fluorene	7248.44	1.533
9,10-dihydroanthracene	7918.29	1.582
2-methylfluorene	7968.28	1.587
9,10-dihydrophenanthrene	8053.26	1.500
phenanthrene	8753.1	1.466
pyrene	10882.6	1.471

Table 4.7 Compounds identified in CHCD 9261 by using GCxGC/(EI)TOF MS.

Compound	Elution time polar column (s)	Elution time nonpolar column (s)
_n_-alkanes		
_n_-octane	459.988	1.507
_n_-decane	1189.82	2.829
_n_-dodecane	2564.51	3.559
_n_-tetradecane	4109.16	3.564
_n_-pentadecane	4848.99	3.487
_n_-hexadecane	5548.83	3.446
_n_-heptadecane	6218.68	3.384
_n_-octadecane	6853.53	3.316
cycloalkanes		
isopropylcyclohexane	959.873	2.067
_n_-butylcyclohexane	1579.73	2.633
_n_-pentylcyclohexane	2314.56	2.926
trans-decahydronapthalene	1959.65	2.391
cis-decahydronapthalene	2404.54	2.317
_n_-hexylcycloalkane	3114.38	3.055
alkylbenzenes		
ethylbenzene	1034.86	1.502
_m_-xylene	1059.85	1.538
_o_-xylene	1234.81	1.575
isopropylbenzene	1364.78	1.707
_n_-propylbenzene	1554.74	1.774
3-ethyltoluene	1629.72	1.785
1,3,5-trimethylbenzene	1669.71	1.805
2-ethyltoluene	1804.68	1.785
1,2,4-trimethylbenzene	1884.66	1.826
sec-butylbenzene	1919.65	1.944
1,2,3-trimethylbenzene	2179.60	1.810
_n_-butylbenzene	2289.57	1.985
saturated ring-containing compounds		
indane	2424.54	1.718
tetralin	3544.29	1.742
cyclohexylbenzene	4689.03	1.895
naphthalenes		
naphthalene	4014.18	1.579

Table 4.7 continued

1-methylnapthalene	5058.94	1.599
2-ethylnaphthalene	5573.82	1.672
aromatic compounds containing more than one benzene ring		
biphenyl	5633.81	1.553

4.3.2   Elution boundaries for alkenes and heteroatom-containing compounds

Previous studies have classified compounds in fuels into several hydrocarbon classes (*i.e.,* linear and branched alkanes, cyclic alkanes and aromatic compounds) by using GCxGC/FID and GCxGC/(EI)TOF MS.[26-29] It is important to note that alkene and heteroatom-containing compound classes were not included as the amounts of these compounds were expected to be very low. The fuels analyzed in these studies had been treated to remove alkenes and heteroatom-containing compounds and as a result, the compounds have been reported to be present in the ppm range or lower.[30,31] Hence, the concentrations of these compounds, if present, are likely below the limit of detection of the instrument. This is desirable as alkenes and heteroatom-containing compounds pose a significant risk to the storage stability of fuel and adversely influence combustion properties.[33,33] However, if a fuel contains a large enough concentration of these harmful compounds to produce detectable signals, it is imperative to identify the compounds correctly.

When using GCxGC/FID, elution boundaries of known compounds are used to classify unknown compounds in fuels. However, if an alkene or heteroatom-containing compound happens to elute within these boundaries, it will be erroneously identified as an alkane or an aromatic compound. GCxGC/(EI)TOF MS has an advantage over GCxGC/FID at classifying and identifying compounds because the molecular weights and elemental compositions can be measured. Furthermore, the EI mass spectrum measured for an unknown compound can be compared to EI mass spectral libraries to facilitate identification.

To examine whether harmful compounds may be incorrectly assigned by using only elution boundaries (GCxGC/FID), the elution times of some alkenes and heteroatom-containing compounds were determined. These elution times were compared to those of known hydrocarbons to determine whether the alkenes and heteroatom-containing compounds elute in the same elution boundaries.

4.3.2.1   Alkenes

Upon combustion, alkenes produce greater amounts of reactive hydroperoxyl radicals ($HO_2\bullet$) and diolefins compared to alkanes.[32] The $HO_2\bullet$ radicals are highly reactive and may decrease the stability of fuel. Fuel stability is defined as the resistance of the fuel to physical and chemical changes that adversely affect vehicle performance. Therefore, the ability to detect alkenes in fuels is important.[32,33] The alkenes used in this study were not detected in any of the fuel samples analyzed (Table 4.1). According to the Chevron Corporation, alkene content in aviation fuel must not exceed the ppmrange.[30] Therefore, the concentrations of the alkenes are expected to be below the limit of detection of the GCxGC/(EI) TOF MS instrument.

Based on GCxGC/(EI) TOF MS measurements, the elution times for the alkenes are similar to those of alkanes and cycloalkanes (Table 4.1). As a result, elution boundaries cannot be used to differentiate alkanes and cycloalkanes from alkenes (Figure 4.**7**). For example, 1-octene (numerical indicator 3, please see Figure 1) has similar elution times as *n*-octane (numerical indicator 1) and 1-methylcyclohexane (numerical indicator 4). 1-Octadecene (numerical indicator 52) elutes in a boundary diagnostic for cycloalkanes.[27,28]

Alkylbenzenes with a C=C bond were shown to have elution times similar to alkylbenzenes that lack the C=C bond (Table 4.1). For example, allylbenzene (14), *cis*-1-propenylbenzene (22),

4-methylstyrene (23) and *trans*-β-methylstyrene (28) have elution times similar to those of 2-ethyltoluene, 1,2,4-trimethylbenzene and 1,2,3-trimethylbenzene (Figure 4.7)

Above results demonstrate that classification of compounds based solely on elution times is likely to result in erroneous classification for alkenes if they produce detectable signals. Hence, GCxGC/(EI)TOF MS has an important advantage over GCxGC/FID as it can be used to identify the eluting compounds.
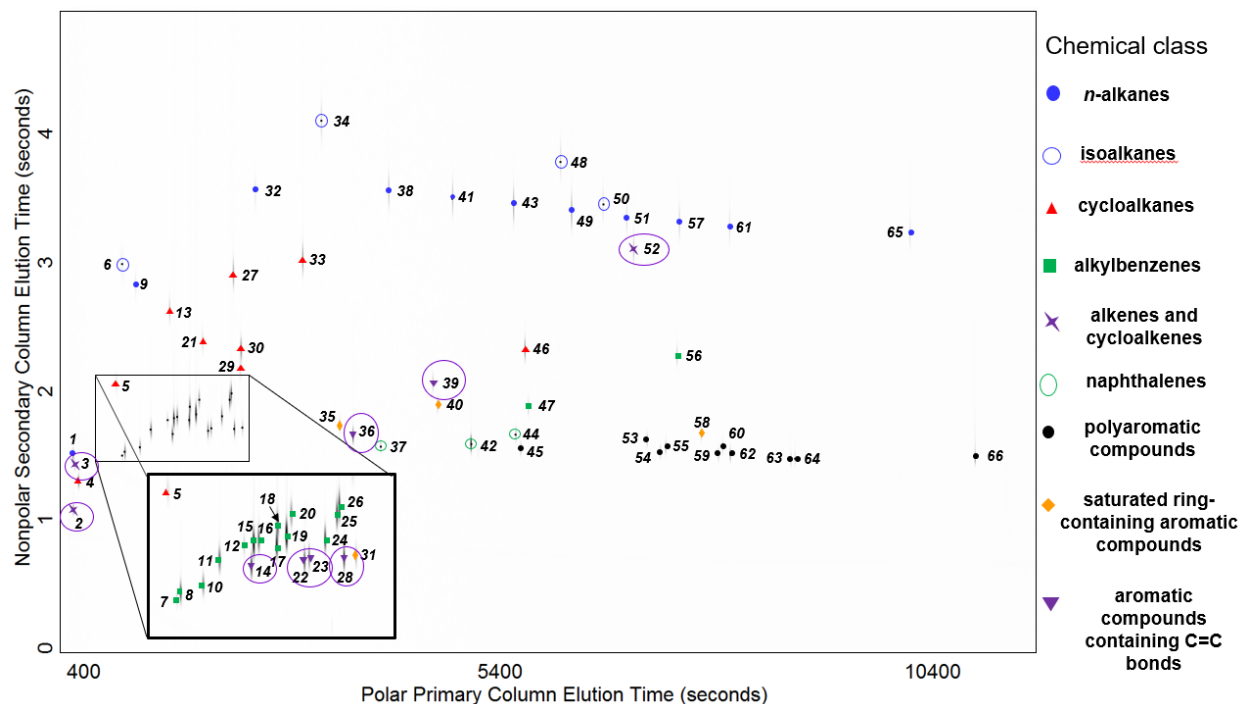
Figure 4.7 Total ion current chromatogram (TIC) shown in Figure 4.2 with the aromatic compounds containing C=C bonds circled in purple. 1,4-Cyclohexadiene (2) and 1-octene (3) have elution times similar to branched and linear alkanes and cycloalkanes. Allylbenzene (14), *cis*-1-propenylbenzene (22), 4-methylstyrene (23) and *trans*-β-methylstyrene (28) have elution times similar to alkylbenzenes and saturated ring-containing compounds. 1,2-Dihydronaphthalene (36) has elution times between those of a saturated ring-containing aromatic compound and a naphthalene . Further, 1-octadecane (52) elutes in the cycloalkane boundary. The region were several aromatic containing C=C bonds was expanded for easier viewing.

4.3.2.2   Heteroatom-containing compounds

Nitrogen and sulfur-containing compounds, alkenes and organic acids decrease the storage stability of a fuel,[33-35] ultimately producing large insoluble particulates and gums. [33-35] For example, heterocyclic nitrogen-containing compounds (*e.g*., indole, shown in Figure 4.8) have been reported to react with phenalenones to form sediment and gums.[36-39] Unstable petroleum-based fuels have also been found to contain greater concentrations of quinolines compared to stable fuels.[40]

When fuels are combusted, sulfur-containing compounds produce SO_2 that gets oxidized to form sulfuric acid, which contributes to air pollution, decreasing visibility (*i.e.,* smog) and exacerbating human diseases (*i.e.,* pre-existing respiratory and cardiovascular diseases).[41-43] It is therefore important to determine whether the elution boundaries of heteroatom-containing compounds can be distinguished from those of hydrocarbons.
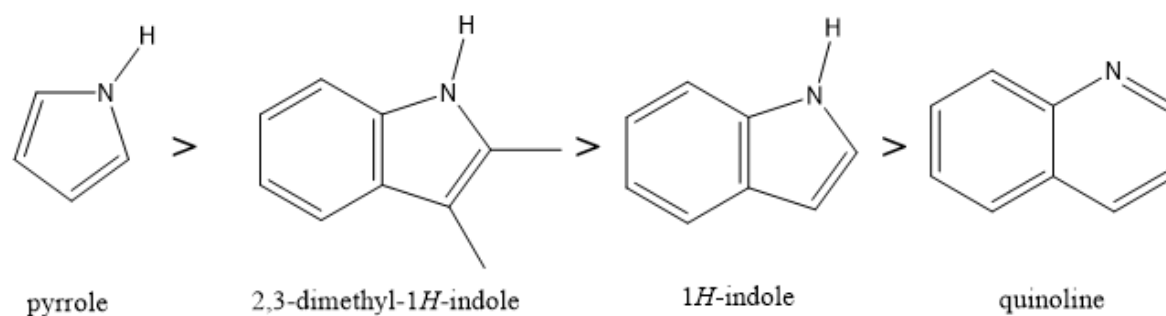
Figure 4.8 Propensity of different nitrogen-containing compounds in fuel to form sediment

To determine the elution times for some heteroatom-containing compounds, an equimolar mixture of five compounds (quinolone, isoquinoline, indole, benzo[a]thiophene and benzothiazole) was prepared in *n*-hexane and diluted to a final concentration of 125 µM. The elution times for the compounds were determined and are presented in Table 4.8. Based on the elution times of these five heteroatom-containing compounds, overlap with aromatic hydrocarbons did not occur.

When the five heteroatom-containing compounds were doped into Jet A, the compounds can be easily distinguished from the hydrocarbon compounds in Jet A (Figure 4.9). Further, these five compounds were not detected in any of the fuel samples measured in this study (Tables 4.1 – 4.7).
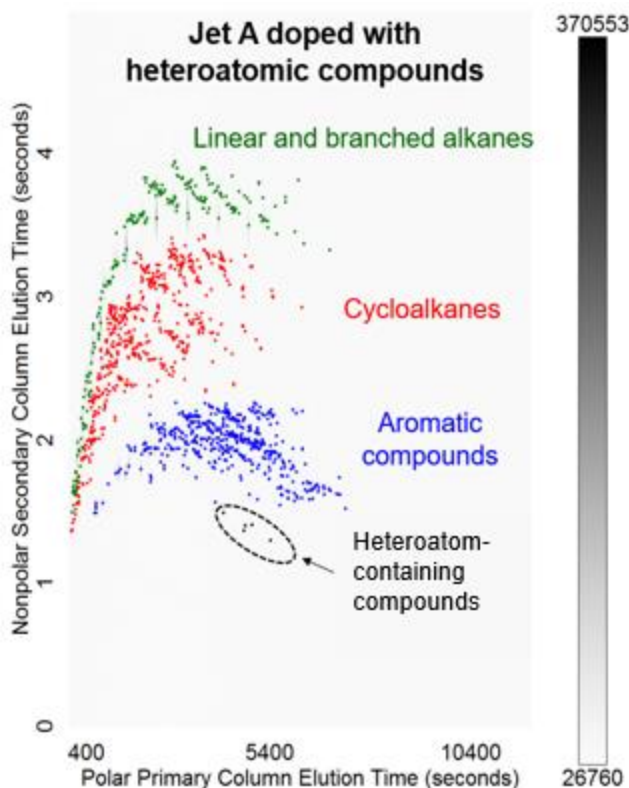
Figure 4.9 Jet A doped with quinoline, isoquinoline, indole, benzo[a]thiophene and benzothiazole. These compounds have shorter elution times than the aromatic compounds in Jet A. The structures of the heteroatom-containing compounds are shown in Figure 4.10.

The five heteroatom-containing compounds studied did not contain an alkyl chain(s). As the number of saturated carbons increases, the polarity of the compounds will likely decrease. For heteroatom-containing compounds, this may result in greater retention in the nonpolar column. Consequently, the elution times for the heteroatom-containing compounds may overlap with aromatic compounds. Future studies should examine whether commercially available 2-methylbenzothiophene and 2-ethylthiophene have elution times in the first column that are greater than those of benzothiophene and thiophene, respectively. The elution times of 2-methylbenzothiophene and 2-ethylthiophene may overlap with aromatic compounds (*e.g.*, naphthalene) and therefore elute in the aromatic elution time boundary.

Although the compounds in this study were not detected in the fuel samples, it is highly recommended to measure the elution times of additional harmful compounds (*i.e.,* commercially available 3-methylquinoline, 2-ethylquinoline 2-propylquinoline) in order to determine if their elution times overlap with aromatic compounds. It is also recommended to extract and concentrate heteroatom-containing compounds in fuels prior to GCxGC(EI)/TOF MS measurements. Harmful compounds may be present in fuel, but are below the detection limit of the instrument. Hence, if the harmful compounds are concentrated before analysis, the harmful analytes may produce detectable signals.

Table 4.8 Elution times for heteroatom-containing aromatic compounds measured by using GCxGC/(EI)TOF MS.

Name and Structure	Elution time from primary column (s)	Elution time from secondary column (s)
benzothiophene	4214.13	1.497
benzothiazole	4734.01	1.373
quinoline	4759.01	1.409
isoquinoline	4938.97	1.409
indole	5383.87	1.306

4.4   Conclusions

The major aim of this study was to determine the chemical compositions of petroleum-based jet fuel and a diesel fuel, alternative aviation fuels, aviation fuel blending components, and potential aviation fuels by using GCxGC/(EI) TOF MS. An additional aim was to determine whether the elution boundaries for harmful alkenes and heteroatom-containing compounds overlap with those of beneficial hydrocarbons.

Overall, the chemical compositions of petroleum-based fuels (*i.e.,* Jet A and diesel) were found to differ slightly when compared to potential alternative aviation fuels (*i.e.,* CHCJ and CHCD), likely influencing many physical and chemical properties (*i.e.,* freezing point and vaporization temperature). The linear alkanes and aromatic compounds in petroleum-based fuels have a greater range of differently sized compounds than the alternative fuels. The absence of small alkanes and aromatic compounds in CHCJ and CHCD may result in greater vaporization points when compared to Jet A and diesel. Greater vaporization temperatures of fuels would result in safer working conditions for ground crew personnel working on aircraft carriers as the flash point would be greater and less volatile cancer-causing compounds would be released into the air. The larger linear alkanes in Jet A and diesel likely contribute to greater freezing point temperatures compared to CHCJ and CHCD. An aircraft flying at high altitudes and/or cold temperatures may perform better when using CHCJ instead of Jet A because the large linear alkanes in Jet A will crystalize in the fuel lines than smaller alkanes.

Based on the EI mass spectra database libraries, the largest aromatic compounds in Jet A and diesel contain three to four fused benzene rings. Conversely, the largest aromatic compounds in CHCJ and CHCD contain only two fused benzene rings. This finding suggests that CHCJ and CHCD may produce less soot and emissions compared to Jet A and diesel during combustion.

Future studies should explore the extent of emissions and soot production for these potential fuels and compare the findings to diesel and Jet A.

The elution boundaries of the alkenes were found to overlap with those of alkanes and cycloalkanes. Therefore, the use of solely elution times (GCxGC/FID) can lead to incorrect classification of compounds in fuels. To clearly distinguish between eluted alkenes, alkanes and cycloalkanes, the identification of the compounds via measurement of EI mass spectra was necessary. The alkenes studied here were not detected in any of the fuel samples analyzed using GCxGC/(EI)TOF MS.

Heteroatom-containing compounds were also studied. Their elution times in the first column were less than those of tested aromatic compounds. It is important to note that if the polarity of these compounds decreases, for example upon addition of alkyl chains, the heteroatom-containing compounds may elute in the qualitative boundary diagnostic for aromatic compounds. Future studies should determine whether commercially available heteroatom-containing compounds elute in regions diagnostic for aromatic hydrocarbons.

The heteroatom-containing compounds studied here were not detected in any of the fuels analyzed using GCxGC/(EI)TOF MS. The compounds may be present but below the limit of detection for the instrument. Extraction and separation methods may be necessary before analysis using h GCxGC/(EI)TOF MS to adequately detect minor heteroatom-containing compounds.

4.5   References

1. Striebich, R.C.; Shafer, L.M.; Adams, R.K.; West, Z.J.; DeWitt, M.J.; Zarbarnick, S. Hydrocarbon Group-type Analysis of Petroleum-Derived and Synthetic Fuels Using Two-dimensional Gas Chromatography. *Energy Fuels* **2014**, *28* (9), 5696-5706.

2. Benoit, J.; Perry, D.; Mondal, K. Fischer-Tropsch synthesis in supercritical CO_2 – Inhibition of CO_2 Selectivity for Enhanced Hydrocarbon Production. *Fuel* **2017**, *209*, 383 – 393.

3. Yang, R.; Zhou, L.; Gao, J.; Hao, X.; Wu, B.; Yang, Y.; Li, Y. Effects of Experimental Operations on the Fischer-Tropsch Product Distribution. *Catal. Today* **2017**, *298*, 77-88.

4. Caldwell, L.; Van Vuuren, DS. On the Formation and Composition of the Liquid Phase in Fischer-Tropsch Reactors. *Chem. Eng. Sci.* **1986**, *41* (1), 89-96.

5. Starck, L.; Pidol, L.; Jeuland, N.; Chapus, T.; Bogers, P.; Bauldreay, J. Production of Hydroprocessed Esters and Fatty Acids (HEFA) – Optimisation of Process Yield Oil & Gas Science and Technology – Rev. IFP *Energies Nouvelles* **2016**, *71* (1), 10 – 22.

6. Tao, L.; Milbrandt, A.; Zhang, Y.; Wang, W.C. Techno-economic and Resource Analysis of Hydroprocessed Renewable Jet Fuel. *Biotechnol. Biofuels* **2017**, *10*, 261 – 277.

7. Corporan, E.; Edwards, T.; Shafer, L.; DeWitt, MJ.; Klingshirn, C.; Zabarnick, S.; West, Z.; Striebich, R.; Graham, J.; Klein, J. Chemical, Thermal Stability, Seal Swell, and Emissions Studies of Alternative Jet Fuels. *Energy Fuels* **2011**, *25* (3), 955-966.

8. Wang, W.C.; Tao, L.; Markham, J.; Zhang, Y.; Tan, E.; Batan, L.; Warner, E.; Biddy M. Review of biojet fuel conversion technologies. Golden: NREL (National Renewable Energy Laboratory); 2016.

9. ARA. https://www.ara.com/capabilities/advanced-biofuels-andrenewable-chemicals (accessed December 28, 2016).

10. Moore, R.H.; Shook, M.; Beyersdorf, A.; Corr, C.; Herndon, S.; Knighton, W.B.; Miake-Lye, R.; Thornhill, K.L.; Winstead, E.L.; Yu, Z.; Ziemba, LD.; Anderson, B.E. Influence of Jet Fuel Composition on Aircraft Engine Emissions: A Synthesis of Aerosol Emissions Data from the NASA APEX, AAFEX, and ACCESS Missions. *Energy Fuels* **2015**, *29* (4), 2591 – 2600.

11. National Research Council (US) Subcommittee on Permissible Exposure Levels for Military Fuels. Permissible Exposure Levels for Selected Military Fuel Vapors. Washington (DC): National Academies Press (US); 1996. Physical and Chemical Properties of Military Fuels.Available from: https://www.ncbi.nlm.nih.gov/books/NBK231234/

12. Standard Test Method: ASTM D1319 Standard Test Method for Hydrocarbon Types in Liquid Petroleum Products by Fluorescent Indicator Adsorption. ASTM International, West Conshohocken, USA (2015), D02.04.0C,

13. Standard Test Method: ASTM D1840 Standard Test Method for Naphthalene Hydrocarbons in Aviation Turbine Fuels by Ultraviolet Spectrophotometry. ASTM International, West Conshohocken, USA (2017), D02.04.0F

14. Standard Test Method: ASTM D4294 Standard Test Method for Sulfur in Petroleum and Petroleum Products by Energy Dispersive X-ray Fluorescence Spectrometry. ASTM International, West Conshohocken, USA (2016), D02.03. 2016

15. Hope J, Sinha A, Prazen B, Synovec R.J Evaluation of the Dotmap Algorithm for Locating Analytes of Interest Based on Mass Spectral Similarity in Data Collected Using Comprehensive Two-Dimensional Gas Chromatography Coupled with Time-of Flight Mass Spectrometry. *Chrom A* **2005**, *1086* (1-2), 185–192.

16. Sinha, A.E.; Fraga, C.G.; Prazen, B.J.; Synovec, R.E.Trilinear Chemometric Analysis of Two-Dimensional Comprehensive Gas Chromatography-Time_of_Flight Mass Spectrometry Data. *J Chrom A* **2004**, *1027* (1-2), 269–277.

17. Hakim. M.; Broza, Y.Y.; Barash, O.; Peled, N.; Phillips, M.; Amann, A.; Haixk, H. Volatile Organic Compounds of Lung Cancer and Possible Biochemical Pathways. *Chem. Rev.* **2012**, *112*, 5949 – 5966.

18. Filipiak, W.; Sponring, A.; Mikoviny, T.; Ager, C.; Schubert, J.; Miekisch, W.; Amann, A.; Troppmair, J. Release of Volatile Organic Compounds (VOCs) from the Lung Cancer Cell Line CALU-1 in vitro. *Cancer Cell Int.* **2008**, *8*, (17) 1-11.

19. Sponring, A.; Filipiak, W.; Mikoviny, T.; Ager, C.; Schubert, J.; Miekisch, W.; Amann, A.; Troppmair, J. Release of Volatile Organic Compounds from Lung Cancer Cell Line NCI-H2087 in vitro. *Anticancer Res.* **2009**, *29* (11), 419 – 426..

20. Lemmon, E. W.; Friend, M. M. Thermophysical Properties of Fluid Systems. NIST Chemistry WebBook, NIST Standard Reference Database Number 69; Linstrom, P.J., Mallard, W.G., Eds.; National Institute of Standards and Technology: Gaithersburg MD, http:// webbook.nist.gov.

21. Das, D.D.; McEnally, C.S.; Kwan, T.A.; Zimmerman, J.B.; Cannella, W.J.; Mueller, C.J.; Pfefferle, L.D. Sooting Tendencies of Diesel Fuels, Jet Fuels, and Their Surrogates in Diffusion Flames. *Fuel* **2017**, *197* (4), 445 – 458.

22. Sabatini, N.A. AC 43-206 Inspection, Prevention, Control, and Repair of Corrosion of Avionics Equipment. Advisory Circular, US Department of Transportation. Federal Aviation Adminstration, 05-30-01. 1- 171.

23. Romanczyk, M.; Ramirez, J.H.; Xu, L.; Vozka, P.; Dissanayake, P.; Wehde, K.E.; Roe, N.; Keating, E.; Kilaz, G.; Trice, R. W.; Luning Prak, D.J. Kenttämaa, H.I. The Capability of Organic Compounds to Swell Acrylonitrile Butadiene O-rings and Their Effects on O-ring mechanical Properties. *Fuel* **2019**, *238*, 483 – 492.

24. Ruzicka, V.; Zabranshy, M.; Ruzicka, K.; Maher, V. Vapor Pressures for Group of High-boiling alkylbenzenes under environmental conditions. *Thermochim. Acta*. 1994, 245 (10) 121 – 144.

25. Working Group on PAH. Ambient air pollution by polycyclic aromatic hydrocarbons (PAH): Position papers and annexes; Office for Official Publications of the European Communities, Luxembourg, 2001; ISBN 92−894−2057-X; http://ec.europa.eu.

26. Shi, X.; Li, H.; Song, Z.; Zhang, X.; Liu, G. Quantitative Composition-Property Relationship of Aviation Hydrocarbon Fuel Based on Comprehensive Two-Dimensional Gas Chromatography with Mass Spectrometry and Flame Ionization Detector. *Fuel* **2017**, *200*, 395 – 406.

27. Vozka, P.; Modereger, B.A.; Park, A.C.; Zhang, W.T.J.; Trice, R.W.; Kenttämaa, H.I.; Kilaz, G. Jet Fuel Density via GCxGC FID. *Fuel* **2019**, *235* (1), 1052 – 1060.

28. Vozka, P.; Huaping, M.; Šimáček, P.; Kilaz, G. Middle Distillates Hydrogen Content via GCxGC-FID. *Talanta* **2018**, *186*, 140 – 146.

29. Luning Prak, DJ, Romanczyk M, Wehde KE, Ye S, McLaughlin M, Luning Prak PJ, Foley MP, Kenttämaa HI, Truelove PC, Kilaz G, Xu L, Cowart JS. Analysis of Catalytic Hydrothermal Conversion Jet Fuel and Surrogate Mixture Formulation: Components, Properties, and Combustion. *Energy Fuels* **2017**, *31* (12), 13802-13814.

30. Aviation Fuels Technical Review. Chevron Products Company, 2007, page 27.

31. Van der Westhuizen, R.; Ajam, M.; De Coning, P.; Beens, J.; de Villiers, A. Sandra, P. Comprehensive Two-Dimensional Gas Chromatography for the Analysis of Synthetic and Crude-Derived Jet Fuels. *J Chromatogr. A* **2011**, *1218* (28) 4478–4486.

32. Mehl, M.; Pitz, W.J.; Westbrook, C.K.; Curran, H.J. Kinetic Modeling of Gasoline Surrogate Components and Mixtures Under Engine Conditions. *Proceedings of the Combustion Institute* **2011**, *33* (1), 193–200.

33. Frankenfeld, J. W.; Taylor, W. F.; Brinkman, D. W. Storage Stability of Synfuels from Oil Shale. 2. Effects of Nitrogen Compound Type and the Influence of Other Non-hydrocarbons in Sediment Formation in Model Fuel Systems. *Ind. Eng. Chem. Res.* **1983**, *22* (4), 615 - 621

34. Mushrush, G. W.; Cooney, J. V.; Beal, E. J.; Hazlett, R. N. Characterization and Stability Properties of Polar Extracts Derived from a Recent Shale Liquid. *Fuel Sci. Technol. Int.* **1986**, *4*, 103 – 125.

35. Pradelle, F.; Braga, S.L.; Martins, A.R.; Turkovics, F.; Pradelle, R.N.C. Gum Formation in Gasoline and Its Blends: A Review. *Energy Fuels* **2015**, *29* (12), 7753 – 7770.

36. Pedley, J.F.; Hiley, R.W.; Hancock, R.A. Storage Stability of Petroleum-Derived Diesel Fuel. *Fuel* **1988**, *67* (8), 1124 – 1130.

37. Frankenfeld, J.W.; Taylor, W.F. Storage Stability of Synfuels from Oil Shale, 1. General Features of Sediment Formation in Model Fuel Systems. *Ind. Eng. Chem. Prod. Res. Dev.* **1983**, *22* (4), 608 – 614.

38. Oasmaa, A.; Kuoppala, E. Fast Pyrolysis of Forestry Residue. 3. Storage Stability of Liquid Fuel. *Energy Fuels* **2003**, *17* (4), 1075 – 1084.

39. Dahlin, K.E.; Daniel, S.R.; Worstell, J.H. Deposit Formation in Liquid Fuels. 1. Effect of Coal-Derived Lewis Bases on Storage Stability of Jet A Turbine Fuel. *Fuel* **1981**, *60* (6), 477- 480.

40. Bauserman, J.W.; Mushrush, G.W.; and Hardy, D.R. Organic Nitrogen Compounds and Fuel Instability in Middle Distillate Fuels. *Ind. Eng. Chem. Res.* **2008**, *47* (22), 2867 – 2875.

41. Pope, C.A. 3rd; Dockey, D.W. Health Effects of Fine Particulate Air Pollution: Lines that Connect. J. *Air Waste Manage. Assoc.* **2006**; *56* (6), 709 – 742.

42. Zanobetti, A.; Schwartz, J.; Gold, D. Are There Sensitive Subgroups for the Effects of Airborne Particles? *Environ. Health Pers.* **2000**, *108* (9), 841-845.

43. Goldberg, M.S.; Burnett, R.T.; Bailar, J.C., III; Tamblyn, R.; Ernst, P.; Flegel, K.; Brook, J.; Bonvalot, Y.; Singh, R.; Valois, M.-F.; Vincent, R. Identification of Persons with Cardiorespiratory Conditions Who Are at Risk of Dying from the Acute Effects of Ambient Air Particles; *Environ. Health Pers.* **2001**, *109* (4), 487-494.

CHAPTER 5.   EFFECTIVENESS OF DIFFERENT AROMATIC AND NONAROMATIC COMPOUNDS TO SWELL ACRYLONITRILE BUTADIENE O-RING SEALS

5.1   Introduction

As petroleum resources diminish, efforts to produce non-petroleum based fuel from alternative and sustainable resources have received national attention.[1] In recent years, the United States Department of Defense has untaken efforts to develop fuel via the Fischer-Tropsch (FT) catalytic process.[2] Feedstocks for the FT catalytic process include coal, natural gas and biomass.[3,4] The FT process produces mixtures composed of linear and branched saturated hydrocarbons, which differ in chemical composition when compared to petroleum-based fuels (*i.e.,* Jet A and JP-8), which are composed of linear, branched, and cyclic saturated hydrocarbons and aromatic compounds. The absence of aromatic compounds in FT products is a concern because the aromatic compounds are chiefly responsible for swelling o-ring seals in the fuel circulations systems of aircraft.[2,5] If fuels lacking aromatic compounds are used in fuel circulation systems, the o-ring seals may not swell to an appropriate volume, which may result in fuel leaks.[6] Hence, the hydrocarbon products produced by FT are not used as a neat fuel and require blending with a petroleum fuel up to 50 % by volume to be used in airplanes.[7]

The extend of o-ring swelling is dictated by the physical and chemical properties of the compounds in the fuels, the composition of the polymer matrix, and the extent of polymer cross linking in the o-ring seal.[2,5,7-11] O-ring seals found in aircraft fuel circulation systems are commonly composed of nonpolar polybutadiene and polar polyacrylonitrile chains (commonly referred to as Buna-N or nitrile rubber o-rings).[7,12,13] The nonpolar chains contribute to the overall softness and

pliability of the seals via weak dispersion forces.[5] The polar chains are fuel resistant[12] and contain

polar cyano groups on opposing chains that form strong dipole-dipole intermolecular forces.[5]

The mechanism of o-ring swelling is described by two competing processes: the free energy

of mixing (ΔF_m) and the elastic free energy (ΔF_{el}) and is expressed as shown in Eq. 5.1.[8]

$$\Delta F = \Delta F_m + \Delta F_{el} \tag{5.1}$$

In fuel circulation systems, o-ring seals contribute to a volume into which compounds in fuel may

spread. Consequently, the compounds can increase their entropy by entering the o-ring seals. Upon

entry, the compounds stretch the polymer chains and elastic retractable forces develop within the

o-rings. As the concentration of the compounds entering the seals increases, the elastic free energy

increases until the energy is equal in magnitude, but opposite in sign, to the free energy of mixing.

At this point, an equilibrium is reached between the force of the compounds entering the seals and

the force of the polymer matrix pushing against the fuel.

Previous studies have examined crude-oil related aromatic compounds and their efficacy

to swell Buna-N o-ring seals.[5] Overall, aromatic compounds with a low molar mass, low molar

volume and a polar functionality capable of exhibiting hydrogen bonding (*e.g.,* benzyl alcohol and

phenol) were found to swell o-rings with the greatest efficiency.[2,5,7,9] The subclass of aromatic

compounds (*i.e.,* benzenes and naphthalenes) were also shown to influence their effectiveness at

swelling seals. For example, alkylnaphthalenes swell seals more effectively than alkylbenzenes.[14]

The aim of this work was to evaluate the propensies of different aromatic and nonaromatic

compounds to swell o-ring seals. It is important to note that aromatic compounds decrease the

fuel's combustion efficiency, contribute to a lower smoke point, are characterized as a major soot

producer, and release high emissions and large particulates into the atmosphere.[15-17] These events

can contribute to an underperforming engine and detrimental effects on the environment and air

quality. Furthermore, the engine may require more effective maintenance. Currently, fuel blending components are blended with petroleum-based fuel which may contain aromatic compounds that do not swell seals efficiently, but still contribute to adverse effects (*i.e.,* soot production). In lieu of blending a fuel blending component with a petroleum-based fuel, tailored aromatic formulations should be designed that contain compounds that swell o-ring seals efficiently while contributing to fewer adverse effects. Hence, this study was designed to determine how the exact structure of aromatic and nonaromatic compounds influences their propensity to swell o-ring seals.

5.2   Experimental

5.2.1   Chemicals and materials

Ethylbenzene (99 % purity) was purchased from Alfa Aesar. *n*-Propylbenzene (98 % purity), isopropylbenzene (98 % purity), 1,3,5-trimethylbenzene (98 % purity), *n*-butylbenzene (≥ 99 % purity), *sec*-butylbenzene (≥ 99 % purity), *tert*-butylbenzene (99 % purity), 1,2,4,5-tetramethylbenzene (98 % purity),1,5-hexadiene (97 % purity), 1-methylcyclohexene (97 % purity), cyclohexene (99 % purity), phenol (≥ 99.0) and 2,6-di-*tert*-butyl-4-methylphenol (≥ 99 % purity) were purchased from Sigma-Aldrich. Indane (95 % purity) and cyclohexane (99 % purity) were purchased from Acros. Tetralin (≥ 97 % purity) and *n*-hexane were purchased (≥ 97 % purity) from Fluka. Sasol isoparaffinic kerosene (referred to as Sasol IPK), and Jet A mixed with hydroprocessed esters and fatty acids (HEFA) at a 50:50 (v/v) (referred to as Jet A/HEFA) were provided by Dr. James T. Edwards of the Wright-Patterson Air Force Base, Dayton, OH. Catalytic hydrothermal conversion jet (CHCJ) fuel (lot number 10128) was received from Dr. Dianne J. Luning Prak of the United States Naval Academy, Annapolis, MD. All compounds Sasol IPK, Jet A/HEFA and CHCJ were used as received without additional purification.

Durometer 70A Buna-N nitrile o-ring seals were procured from USA Sealing Incorporated and used as received. Buna-N nitrile o-rings were chosen for this study because they have a variety of fuel related applications[2,7,9] and are frequently used in aircraft fuel circulation systems.[13]

5.2.2 Instrumentation and methods

To determine the effectiveness of organic compounds to swell o-ring seals, Sasol IPK was doped individually with aromatic or nonaromatic compounds at 8 % by volume. Antioxidants phenol and 2,6-di(*tert*-butyl)-4-methylphenol were doped individually in Sasol IPK at 0.02 % by volume. Due to poor solubility, naphthalene was doped in Sasol IPK at only 1 % by volume. Approximately 100 mL Sasol IPK or 92 mL of Sasol IPK and 8 mL of an organic dopant were added to an Erlenmeyer flask and mixed thoroughly. For dopant 1,2,4,5-tetramethylbenzene, approximately 6.94 g was added into Sasol IPK to end up with a total volume of 100 mL (this dopant is solid at room temperature). Three o-ring seals were submerged in neat or doped Sasol IPK for 48 hours and kept submerged with a metal suspension rig crafted in house (Figure 5.1). The rig was designed to hold three o-ring seals, prevent the seals from touching the flask, and ensure that the o-ring seals were completely submerged. The flask was fitted with a rubber stopper and it contained an opening in the center to insert a condenser. Cold water was flushed through the condenser during the 48-hour immersion period to prevent evaporation of Sasol IPK and the dopant.

O-ring seals were also immersed in 100 mL of alternative fuel Jet/HEFA and potential fuel CHCJ. Alternative fuel Jet A/HEFA is approved for commercial use. It served as a bench mark to compare the effectiveness of the organic dopants added into Sasol IPK at swelling o-ring seals.

A Nikon Profile Projector V-12 was used to measure the cross-sectional diameters of the o-ring seals before and directly after the immersion period (Figure 5.2). The cross-sectional

diameter for each o-ring seal is given as an average of eight measurements (Figure 5.3). The volume

swell percent values for the o-ring seals were calculated with the following equation[18]

$$\mu_i = \left[\left(\frac{d_f}{d_o} \right)^3 - 1 \right] \times 100 \qquad (5.2)$$

where μ_i is the average volume swell percent and d_o and d_f are the average diameters before and

right after the submersion period, respectively.
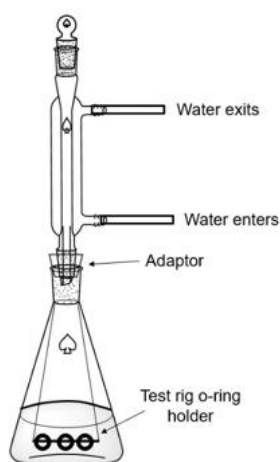
Figure 5.1 The test rig used to immerse o-ring seals in neat and doped Sasol IPK.

Figure 5.2 Nikon Profile Projector V-12 used to measure the diameters of the o-ring seals.
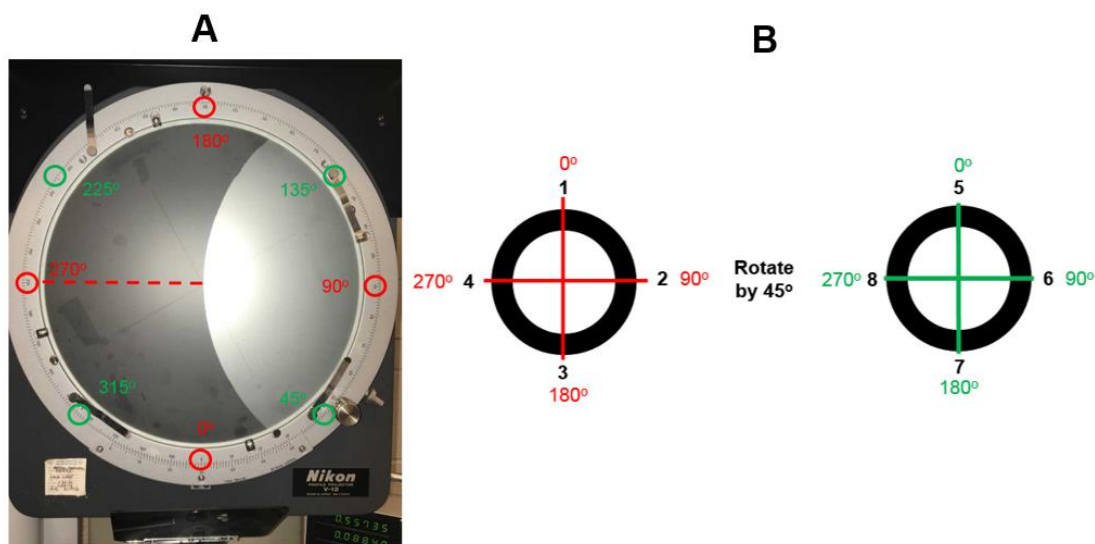
Figure 5.3 (A) The Nikon projector has labeled markings from 0 up to 359 degrees (A). The o-ring seals were positioned in the center of the projector. (B) The cross-sectional diameter of each o-ring seal was measured at 0°, 90°, 180° and 270° (B) (red lines). Each o-ring seal was then rotated by 45° and the diameter was measured again at 0°, 90°, 180° and 270° (green lines). In total, each o-ring seal was measured eight times at 45° intervals. The diameter values used in Equation 5.2 were the averages of the eight measurements.

5.3   Results and discussion

The main goal of this study was to develop correlations between the structures of aromatic and nonaromatic compounds and their propensities to swell o-ring seals (Figure 5.4). The ultimate goal is to learn whether, in lieu of blending fuel blending components with petroleum-based fuels to meet ASTM certifications (i.e., adequate seal swelling), fuel blending components may be doped with only compounds that are highly effective in swelling the seals.

5.3.1   Volume swelling of o-ring seals by nonaromatic compounds

According to Defense Standard 91-91, an alternative fuel must contain aromatic compounds at a minimum of 8 % by volume.[19] Fuel blending component Sasol IPK contains only 0.4 % by volume[20] and therefore, cannot be used as a fuel as such. . In this study, Sasol IPK was doped with aromatic and non-aromatic compounds to evaluate each dopant's propensity to swell

o-ring seals. Non-aromatic compounds were also examined in this study as aromatic compounds contribute to more soot and emissions upon combustion than aliphatic compounds.[21-24] If nonaromatic compounds are found that can effectively swell seals some aromatic compounds could be replaced with such compounds, thus leading to improvements in fuel quality, combustion properties and environmental effects. The volume swell percent values for each dopant measured in this study are presented in Figure 5.5 and Table 5.1.

O-ring seals immersed in neat Sasol IPK and Sasol IPK doped with *n*-hexane did not swell o-ring seals effectively and were the least effective of the mixtures tested (volume swell percents 0.05 ± 0.04 % and 0.02 ± 0.03 %, respectively). These results are in agreement with past findings which showed that linear and branched saturated hydrocarbons do not swell seals to any significant extent.[18,25] Although the linear and branched saturated hydrocarbons contribute to minimal swelling, the volume of the o-ring seals remains relatively the same because there is extraction of plasticizers and processing aides from the seals.[26]

When o-ring seals were immersed in cyclohexane, the volume swell percent was 0.4 ± 0.1 %. It is noteworthy that cyclohexane has a smaller molar volume than compared to *n*-hexane. Previous studies have correlated the volume swell percent of a compound to the inverse of its molar volume.[5,9,27] This line of reasoning may explain why cyclohexane swells seals more effectively than *n*-hexane.

Ultimately, nonaromatic and unsaturated hydrocarbons were found to swell o-ring seals more effectively than saturated hydrocarbons. Cyclohexene swelled o-ring seals four times more effectively than cyclohexane and 1,5-hexadiene swelled seals seventy-five time more effectively than *n*-hexane. Clearly, the presence of double bonds vastly improves the effectiveness of the dopant to swell seals. It is important to note that cyclic cyclohexene swells seals approximately

13 % more effectively than acyclic 1,5-hexadiene. The smaller molar volume of cyclohexane may explain this finding.

While the alkene dopants used in this study were shown to be effective at swelling seals, alkenes produce reactive hydroperoxyl radicals ($HO_2\bullet$) and diolefins which may attenuate the stability of the fuel.[28] Hence, the alkenes used in this study may not ultimately be desired dopants.

Nonaromatic compounds

cyclohexane   hexane   cyclohexene   1,5-hexadiene   1-methylcyclohexene

Aromatic compounds

ethylbenzene   *n*-propylbenzene   1,3,5-trimethylbenzene   isopropylbenzene

n-butylbenzene   *sec*-butylbenzene   *tert*-butylbenzene   1,2,4,5-tetramethylbenzene

indane   tetralin   naphthalene   phenol   2,6-di(*tert*-butyl)-4-methylphenol
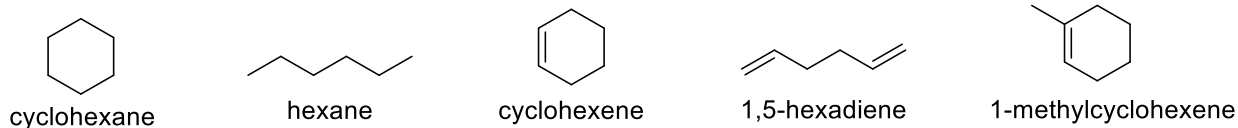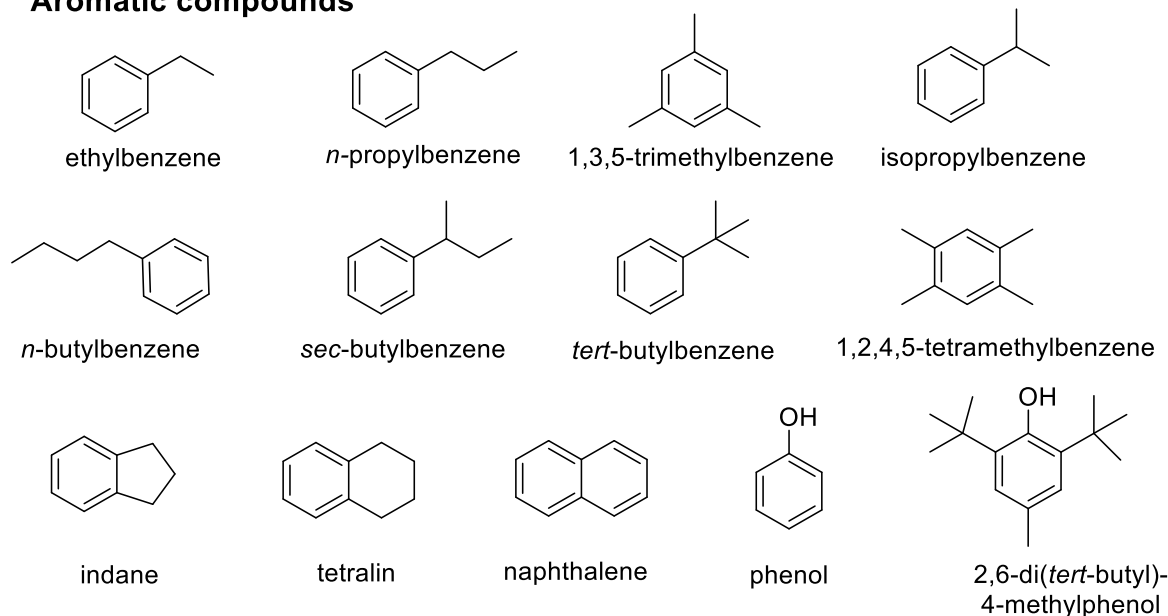
Figure 5.4 Names and structures of dopants used in this study.

5.3.2   Volume swelling of o-ring seals by aromatic compounds

Chemical characterization of petroleum-derived fuel Jet A-1 revealed that alkylbenzenes were the most abundant subclass of aromatic compounds in this jet fuel[29] and that the fuel

contained many isomeric alkylbenzene .[29,30] Hence, several isomeric alkylbenzenes were evaluated to determine their effectiveness to swell seals.

When o-ring seals were immersed in Sasol IPK doped individually with *n*-propylbenzene and isopropybenzene, the volume swell percent values were 1.9 ± 0.2 % and 1.6 ± 0.2 %, respectively. *n*-Propylbenzene swelled o-ring seals 16 % more effectively than isopropylbenzene. When evaluating the propensity of structural isomers with the chemical formula $C_{10}H_{14}$ to swell o-ring seals, the volume swell percent values increased as follows: *tert*-butylbenzene (0.7 ± 0.1 %) < *sec*-butylbenzene (0.9 ± 0.1 %) < *n*-butylbenzene (1.4 ± 0.1 %). It is noteworthy that as the number of branches off the main alkyl group attached to benzene increased, the propensity of the compound to swell o-ring seals decreased.

When o-ring seals were immersed in Sasol IPK doped individually with 1,3,5-trimethylbenzene and 1,2,4,5-tetramethylbenzene, the volume swell percent values were 1.0 ± 0.1 % and 0.29 ± 0.02 %, respectively. Based on this finding, an increase in the number of alkyl groups attached to benzene decreases the propensities of the compounds to swell seals. Dopants 1,3,5-trimethylbenzene and 1,2,4,5-tetramethylbenzene swelled seals least effectively within their isomer group and had the smallest molar volume within their isomeric group. , These dopants did not follow the trend established in previous studies, which showed a correlation between the volume swell percent and the inverse of the molar volume of the dopant.[5] Steric effects may decrease the propensity of 1,3,5-trimethylbenzene and 1,2,4,5-tetramethylbenzene to swell seals.

As the *n*-alkyl group attached to benzene increased, the propensity of the compound to swell o-ring seals decreased. For example, ethylbenzene swelled seals 1.6 and 2.2 times more effectively than *n*-propylbenzene and *n*-butylbenzene, respectively. This result agrees with previous literature.[5] Dopants with a naphthene ring fused to benzene also showed greater

propensities to swell seals compared to alkylbenzene compounds of the same total carbon number. For example, indane swelled o-ring seals 47 % more effectively than *n*-propylbenzene, and tetralin swells o-ring sealed 50 % more effectively than *n*-butylbenzene. The smaller molar volume of indane and tetralin compared to *n*-propylbenzene and *n*-butylbenzene, respectively may explain the above findings.

Naphthalene was also evaluated for its propensity to swell o-ring seals. Due to poor solubility, naphthalene was doped at 1 % by volume in Sasol IPK. Despite the small concentration, it swelled o-ring seals very effectively. Although naphthalene swells o-ring seals more effectively than other dopants at higher concentrations (8 % by volume), naphthalene has a greater sooting index compared to alkylbenzenes and it releases large particulates into the atmosphere upon combustion.[24] Hence, it is not a desirable component of fuels. Studies examining how much soot is released when the concentration of naphthalene is one eighth of alkylbenzenes should be conducted to determine whether doping with naphthalene at a low concentration would still swell seals effectively while contributing to an equal amount of soot as alkylbenzenes at eight times the concentration.

Previous studies have suggested that upon a decrease in the molar mass and molar volume of organic dopants the volume swell percent of o-ring seals increased.[5] To further test these trends by using compounds studied here, the volume swell percent for the aromatic and nonaromatic compounds was plotted against their molar masses and molar volumes (Figure 5.5). No correlations were found unless the compounds were separated into aromatic and aliphatic classes, where nonlinear trends were found in agreement with literature.[5]

The correlations drawn above between the structures of the compounds and the volume swell percent may be related to the diffusivity of the compounds into the polymer matrix and their

partition coefficients into the o-ring seals. The diffusivity of some alkylbenzene into Buna-N o-rings increases as follows: xylene isomers < toluene < benzene.[10,27] The partition coefficients for some alkylbenzenes into o-ring seals increases as follows: *n*-pentylbenzene < *n*-propylbenzene < ethylbenzene < xylene isomers < toluene < benzene. Hence, greater steric hindrance (*i.e.,* the length of the alkyl group attached to benzene, the number of branches in the main alkyl chain and the number alkyl groups attached to benzene) appears to attenuate the diffusivity and partition coefficients for the alkylbenzenes into o-ring seals. This reasoning may explain why 1,3,5-trimethylbenzene and 1,2,4,5-tetramethylbenzene have a decreased propensity to swell seals despite having a smallest molar volume among their isomeric groups.

Aromatic compounds with a polar functionality (*e.g.* phenol groups) have been suggested to effectively swell o-ring seals.[9] Therefore, dopants phenol and 2,6-di(*tert*-butyl)-methylphenol were evaluated for their effectiveness to swell seals compared toother aromatic and the nonaromatic compounds. According to ASTM D1655, the maximum allowed concentration of antioxidants in fuels is 24 mg / L. Previous studies evaluating the effectiveness of antioxidants at swelling seals were performed atconcentrations 400 times the approved concentration.[9,31] In this study, phenol and the hindered phenol were used at a concentration of 24 mg / 100 mL (0.002 % by volume). This concentration was ten times greater than the approved amount in order to have a measureable effect in the 48 hour immersion period. The sterically hindered phenol did not swell o-ring seals to any significant extent. Conversely, despite the low concentration, phenol swelled o-ring seals more effectively than several alkylbenzenes at a larger volume percent (8 % by volume).

Previous studies have drawn correlations between the structure of a compound and its Hansen solubility parameters, which describe the solubility of a solute in a given solvent.[5] The

volume swell percent values of dopants were plotted against their Hansen Solubility parameters for the dispersion, polar and hydrogen-bonding capabilities (Figure 5.6). Nonlinear trends appear to exist between the volume swell percent and the Hansen Solubility parameters of the dopants with the exception of phenol and ethylbenzene. The polar and hydrogen bonding parameters of phenol appear to positively influence the effectiveness of the dopant to swell seals as the phenol functional group has favorable interactions with the polar cyano groups of the polyacrylonitrile chains.
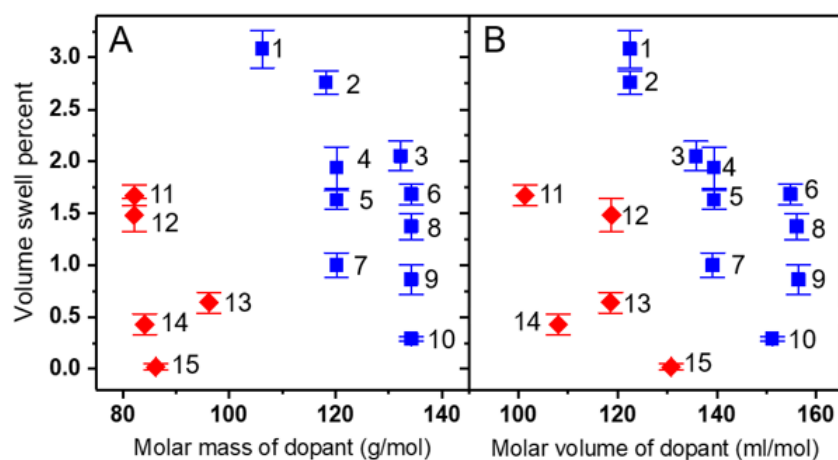
Figure 5.5 The volume swell percent values for o-ring seals vs the dopant molar mass (A) and the dopant molar volume (B). The identities of the compounds in the figure are as follows: ethylbenzene 1, indane 2, tetralin 3, *n*-propylbenzene 4, isopropylbenzene 5, *n*-butylbenzene 6, 1,3,5-trimethyl-benzene 7, *sec*-butylbenzene 8, *tert*-butylbenzene 9, 1,2,4,5-tetramethylbenzene 10, cyclohexene 11, 1,5-hexadiene 12, 1-methylcyclohexene 13, cyclohexane 14 and *n*-hexane 15. The red diamonds indicate data measured for aliphatic compounds and the blue squares for aromatic compounds.
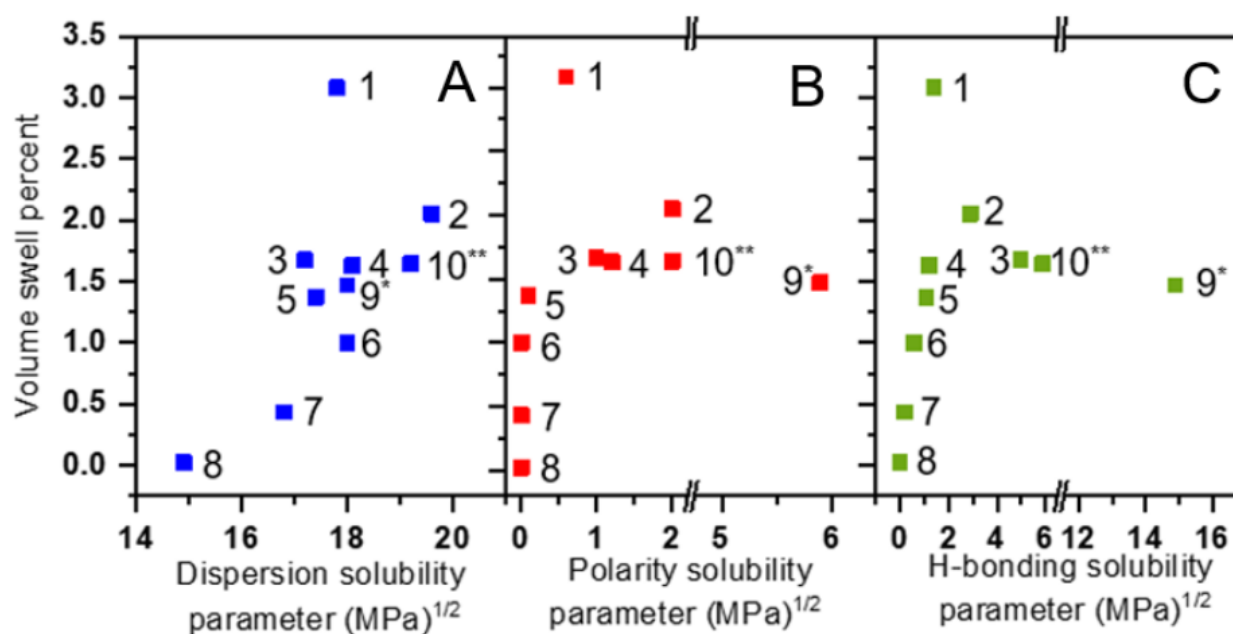
Figure 5.6 Volume swell percent for selected aromatic and nonaromatic dopants versus (A) dispersion solubility parameter, (B) polarity solubility parameter and (C) H-bonding solubility parameter. The identity of the organic dopants is as follows: ethylbenzene 1, tetralin 2, cyclohexene 3, isopropylbenzene 4, n-butylbenzene 5, 1,3,5-trimethylbenzene 6, cyclohexane 7, n-hexane 8, phenol 9 and naphthalene 10. The parameter values were taken from reference 32. Please note that as opposed to the other compounds (doped at 8% by volume), phenol (9)* and naphthalene (10**) were doped only at 0.02 % and 1 % by volume, respectively, in Sasol IPK.

Table 5.1 Volume swell percent values for o-ring seals immersed in CHCJ, a 50:50 blend by volume of Jet A and HEFA, neat Sasol IPK or Sasol IPK doped with different organic compounds at 8 % by volume, except for naphthalene that was doped at 1 % by volume due to its poor solubility into Sasol IPK.

Organic mixtures/compounds used to swell o-ring seals	Volume swell percent[a]	Molar mass of dopant (g/mol)	Molar volume of dopant (ml/mol)
CHCJ	5.5 ± 0.3 %	N/A[b]	N/A[b]
Jet A / HEFA	2.2 ± 0.2 %	N/A[b]	N/A[b]
Sasol IPK	0.05 ± 0.04 %	N/A[b]	N/A[b]
Aromatic dopants			
ethylbenzene	3.1 ± 0.2 %	106.168	122.45
indane	2.8 ± 0.1 %	118.179	122.47
tetralin	2.1 ± 0.1 %	132.206	135.74
n-propylbenzene	1.9 ± 0.2 %	120.195	139.44
naphthalene[c]	1.6 ± 0.2 %	128.174	125.53
isopropylbenzene	1.6 ± 0.1 %	120.195	139.44
n-butylbenzene	1.4 ± 0.1 %	134.222	156.07
1,3,5-trimethylbenzene	1.0 ± 0.1 %	120.195	139.12
sec-butylbenzene	0.9 ± 0.1 %	134.222	156.44
tert-butylbenzene	0.7 ± 0.1 %	134.222	154.81
1,2,4,5-tetramethylbenzene	0.29 ± 0.02 %	134.222	151.15
Nonaromatic dopants			
cyclohexene	1.7 ± 0.1 %	82.143	101.29
1,5-hexadiene	1.5 ± 0.2 %	82.143	118.70
1-methylcyclohexene	0.6 ± 0.1 %	96.173	118.59
cyclohexane	0.4 ± 0.1 %	84.162	108.04
n-hexane	0.02 ± 0.03 %	86.178	130.77
Heteroatomic dopants			
Phenol[d]	1.5 ± 0.2 %	94.113	87.96
2,6-di(*tert*-butyl)-4-methylphenol[d]	0.04 ± 0.07 %	220.351	209.86

[a] Values are reported as an average of three measurements. The standard deviation ($\mu = \pm 1\sigma$) was also determined. [b] Not applicable. [c] Approximately 1.14 g of naphthalene was dissolved in Sasol IPK to obtain a total volume of 100 ml. [d] Approximately 24 mg of phenol or 2,6-di(*tert*-butyl)-4-methylphenol were dissolved individually in 100 mL of Sasol IPK.

5.3.3   Swelling of o-ring seals by alternative fuel Jet A/HEFA and CHCJ fuel

Alternative aviation fuel Jet A/HEFA is made up of Jet A blended up to 50 % by volume with a mixture composed of linear, branched and cyclic saturated hydrocarbons derived from hydroprocessed esters and fatty acids (HEFA).[33] The mass percent of aromatic compounds in Jet A/HEFA used in this study was 11 %. The volume swell percent for o-ring seals immersed in Jet

A/HEFA was 2.2 ± 0.2. It is noteworthy that this value is smaller than the volume swell percent values for o-ring seals immersed in Sasol IPK doped with ethylbenzene (3.1 %) and indane (2.8 %), respectively (the mass percent for ethylbenzene and indane were 10 % and 11 %, respectively). Hence, doping HEFA with ethylbenzene or indane may result in greater swelling when compared to blending HEFA with Jet A up to 50 % by volume. It is important to note that doping HEFA with neat ethylbenzene or indane may decrease the vaporization temperature below that of the 50:50 (v/v) mixture of Jet A/HEFA. The vaporization temperature of Sasol IPK doped with ethylbenzene or indane should be measured to determine if the vaporization temperature would be lower than the approved value set by ASTM. A tailored mixture of many aromatic compounds may be required to swell seals while also meeting other required ASTM physical and chemical properties of fuels (*i.e.,* flash point and gravimetric energy content).

CHCJ fuel is an alternative fuel that has yet to be approved for commercial use in military and civilian aircraft. The chemical composition was reported early.[34] and is included in this dissertation (please see Chapter 4). The volume swell percent for o-ring seals immersed in CHCJ was 5.5 ± 0.3 % and the mass percent of aromatic compounds in CHCJ was 22 %. Hence, the large aromatic content in CHCJ may explain why it was more effective at swelling seals when compared to Jet /HEFA.

5.3.4   Volume swell percent of o-ring seals after changing the solvent

Previous studies showed that when an aircraft fuel tank was originally filled with a petroleum-based aviation fuel and the fuel was then switched to FT derived product, a fuel leak resulted.[6] This observation implies that the volume of o-ring seals after swelling is not constant but is subject to change based on the solvent. To the authors' knowledge, this hypothesis has not been tested.

In order to test above hypothesis, o-ring seals were immersed for 48 hours in Sasol IPK doped with ethylbenzene at 8 % by volume. Afterwards, the volume swell percent of the o-ring seals was determined. Then, the o-ring seals were immediately immersed in neat Sasol IPK and the volume swell percent values were re-measured after 4, 8, 24, 72 and 96 hours. While the o-ring seals were immersed in neat Sasol IPK, aliquots were taken and the concentration of ethylbenzene was quantified by using GCxGC/FID. The volume swell percent was plotted against the concentration of ethylbenzene (Figure 5.7).

The volume swell percent for o-ring seals decreased for the first 50 hours before leveling off. Concurrently, the concentration of ethylbenzene in Sasol IPK increased for the first 50 hours before leveling off. These findings suggest that o-ring volume swelling is a dynamic property. Further, the chemical composition of the solvent influences the volume of the o-ring seals. Neat Sasol IPK contains a smaller concentration of aromatic compounds relative to the concentration of ethylbenzene inside of the o-ring seals. Hence, ethylbenzene diffuses from the seals into the solvent (i.e., Sasol IPK) until a new equilibrium is established.
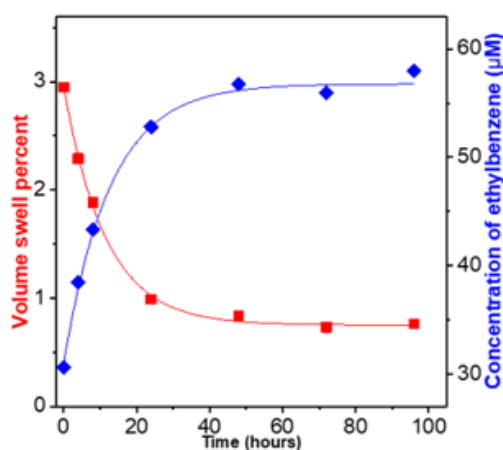

Figure 5.7 Volume swell percent of o-ring seals (red squares) and the concentration of ethylbenzene (blue diamonds) (quantified by using GCxGC/FID) in Sasol IPK after diffusion of ethylbenzene from the o-ring seals as a function of time.

5.4   Conclusions

The volume swell percent of o-ring seals immersed in Sasol IPK doped with different organic compounds was examined. Steric effects were found to influence the propensity of the compounds to swell seals. As the branching in alkyl chains attached to benzene increased, the dopants effectiveness to swell seals decreased. As the length of the alkyl chain attached to benzene increased, the propensity of the dopant to swell o-ring seals decreased. Further, as the number alkyl groups attached to benzene increased, the effectiveness of the dopant decreased. Cyclic compounds were shown to swell o-ring seals more effectively than acyclic compounds of the same carbon number. The presence of carbon-carbon double bonds and benzene ring(s) increased the effectiveness of the dopant to swell o-ring seals. The presence of a phenol group also enhanced the propensity of the dopant to swell o-ring seals, but the efficiency may be attenuated by steric effects (*i.e.,* a hindered phenol did not swell o-ring seals to any significant extent). Nonlinear trends were found between the volume swell percent of the o-ring seals and the molar mass and molar volume of the compounds, which agreed with previous research.[5] Nonlinear trends were also found between the volume swell percent and the Hansen solubility parameters of the dopants.

The total aromatic content by mass in CHCJ is twice that of Jet A/HEFA, which may explain why CHCJ swells o-ring seals more effectively than the approved alternative fuel Jet A/HEFA. It is noteworthy that ethylbenzene and indane doped in Sasol IPK swelled o-ring seals more effectively than Jet A/HEFA, despite having a smaller concentration of aromatic compounds. Addition of ethylbenzene or indane into alternative fuel blending components may swell o-ring seals to adequate volumes while contributing to fewer harmful effects (*i.e.,* soot production and emissions) than blending with petroleum-based fuels.

5.5   References

1. White House, Blueprint for a Secure Energy Future, Washington, DC: Executive Office of the President, March 2011.

2. Gormley, R.J.; Link, D.D.; Baltrus, J.P.; Zandhuis, P.H. Interactions of Jet Fuels with Nitrile O-rings: Petroleum-Derived Versus Synthetic Fuels. *Energy Fuels* **2009**, *23* (2), 857-861.

3. Striebich, R.C.; Shafer, L.M.; Adams, R.K.; West, Z.J.; DeWitt, M.J.; Zarbarnick, S. Hydrocarbon Group-type Analysis of Petroleum-derived and Synthetic Fuels Using Two-dimensional Gas Chromatography. *Energy Fuels* **2014**, *28* (9), 5696-5706.

4. Benoit, J.; Perry, D.; Mondal, K. Fischer-Tropsch Synthesis in Supercritical CO_2 – Inhibition of CO_2 Selectivity for Enhanced Hydrocarbon Production. *Fuel* **2017**, *209*, 383-393.

5. Graham, J.L.; Striebich, R.C.; Myers, K.J.; Minus, D.K.; Harrison, W.E. Swelling of Nitrile Rubber by Selected Aromatics Blended in a Synthetic Jet Fuel. *Energy Fuels* **2006**, *20* (2), 759-765.

6. Anderson, B.E.; Beyersdorf, A.J.; Hudgins, C.H.; Plant, J.V.; Thornhill, K.L.; Winstead, E.L.; Howard, R; Corporan, E; Miake-Lye, R.C.; Herndon, S.C.; Timko, M;, Woods, E.; Dodds, W.; Lee, B; Santoni, G.; Whitefield, P; Hagen, D; Lobo, P; Knighton, W.B.; Bulzan, D.; Tacina, K.; Wey, C.; Vander, Wal R.; Bhargava, A.; Kinsey, J.; Liscinsky, D.S. Alternative Aviation Fuel Experiment (AAFEX). NASA/TM-2011-217059. February 2011.

7. Corporan, E.;, Edwards, T.; Shafer, L.; DeWitt, M.J.; Klingshirn, C.; Zabarnick, S.; West, Z.; Striebich, R.; Graham, J.; Klein, J. Chemical, Thermal Stability, Seal Swell, and Emissions Studies of Alternative Jet Fuels. *Energy Fuels* **2011**, *25* (3), 955-966.

8. Flory PJ. *Principles of Polymer Chemistry*; Cornell University Press: Ithaca, NY, 1953.

9. Link, D.D.; Gormley, R.J.; Baltrus, J.P.; Anderson, R.R.; Zandhuis, P.H. Potential Additives to Promote Seal Swell in Synthetic Fuels and Their Effect on Thermal Stability. *Energy Fuels* **2008**, *22* (2), 1115-1120.

10. Mathai, A.E.; Singh, R.P.; Thomas, S. Transport of Substituted Benzenes through Nitrile Rubber/Natural Rubber Blend Membranes. *J. Membr. Sci.* **2002**, *202* (1-2), 35-54.

11. Joseph, A.; Mathai, A.E.; Thomas, S. Sorption and Diffusion of Methyl Substituted Benzenes Through Cross-linked Nitrile Rubber/Poly(ethylene co-vinyl acetate) Blend Membranes. *J. Membr. Sci.* **2003**, *220* (1), 13-30.

12. Handbook of Elasteromers, 2nd Ed.; Bhowmick, A.K.; Stephens, H.L. Eds; Marce; Dekker: New York, 2007.

13. Roberts, J. O-rings. Lockheed Martin Service News, A Service Publication of Lockheed Martin Aeronautical Systems. Vol. 22 No 4 and Vol. 23 No 1. Pages 1 – 36. October 1995 – March 1996.

14. DeWitt, M.J.; Corporan, E.; Graham, J.; Minus, D. Effects of Aromatic Type and Concentration in Fischer-Tropsch Fuel on Emissions Production and Material Compatibility. *Energy Fuels* **2008**, *22* (4), 2411–2418.

15. Corporan, E.; Edwards, T.; Shafer, L.; DeWitt, M. J.; Klingshirn, C.; Zarbarnick, S.; West, Z.; Striebich, R.; Graham, J.; Klien, C. Chemical, Thermal Stability, Seal Swell, and Emissions Studies of Alternative Jet Fuels. *Energy Fuels* **2011**, *25* (3), 955-966.

16. Beyersdorf, A.J.; Timko, M.T. Ziemba, L.D.; Bulzan, D., Corporan, E. Herndon, S.C.; Howard, R. Miake-Lye, R. Thornhill, K.L.; Winstead, Wey, C.; Yu, Z.; Anderson, B.E. Reductions in Aircraft Particulate Emissions Due to the Use of Fischer-Tropsch Fuels. *Atmos. Chem. Phys.* **2014**, *14*, 11 - 23.

17. Timko, M.T.; Yu, Z.; Onasch, T. B.; Wong, H.W.; Miake-Lye, R. C.; Beyersdorf A.J.; Anderson, B.E.; Thornhill, K.L.; Winstead, E.L.; Corporan, E.; Dewitt, M.J.; Klingshirn, C.D.; Wey, C.; Tacina, K.; Liscinsky, D.S.; Howard, R.; Bhargava, A. Particulate Emissions of Gas Turbine Engine Combustion of a Fischer-Tropsch Synthetic Fuel. *Energy Fuels* **2010**, *24* (11), 5883 – 5896.

18. Fu, J,: Turn S.Q. Effects of Aromatic Fluids on Properties and Stability of Alternative Marine Diesels. *Fuel* **2018**, *216* (2), 171-180.

19. Turbine Fuel, Kerosine Type, Jet A-1; Defence Standard 91-91/Issue 7, Ministry of Defence: U.K. 2015.

20. Romanczyk, M.; Ramirez, J.H.; Xu, L.; Vozka, P.; Dissanayake, P.; Wehde, K.E.; Roe, N.; Keating, E.; Kilaz, G.; Trice, R. W.; Luning Prak, D.J. Kenttämaa, H.I. The Capability of Organic Compounds to Swell Acrylonitrile Butadiene O-rings and Their Effects on O-ring mechanical Properties. *Fuel* **2019**, *238*, 483 – 492.

21. Beyersdorf, A.J.; Timko, M.T.; Ziemba, L.D.; Bulzan, D.; Corporan, E.; Herndon, S.C.; Howard, R.; Miake-Lye, R.; Thornhill, K.L.; Winstead, E.; Wey, C.; Yu, Z.; Anderson, B.E. Reductions in Aircraft Particulate Emissions Due to the Use of Fischer-Tropsch Fuels. *Atmos. Chem. Phys.* **2014**, *14*, 11-23.

22. Timko, M.T.; Yu, Z.; Onasch, T.B.; Wong, H.W.; Miake-Lye, R.C.; Beyersdorf, A.J.; Anderson, B.E.; Thornhill, K.L.; Winstead, E.L.; Corporan, E.; Dewitt, M.J.; Klingshirn, C.D.; Wey, C.; Tacina, K.; Liscinsky, D.S.; Howard, R.; Bhargava, A. Particulate Emissions of Gas Turbine Engine Combustion of a Fischer-Tropsch Synthetic Fuel. *Energy Fuels* **2010**, *24* (11), 5883–5896.

23. Xue, X.; Hui, X.; Singh, P.; Sung, C.J. Soot Formation in No-premixed Counterflow Flames of Conventional and Alternative Fuels. *Fuel* **2017**, *210*, 343-351.

24. Das, D.D.; McEnally, C.S.; Kwan, T.A.; Zimmerman, J.B.; Cannella, W.J.; Mueller, C.J.; Pfefferle, L.D. Sooting Tendencies of Diesel Fuels, Jet Fuels, and Their Surrogates in Diffusion Flames. *Fuel* **2017**, *197*, 445-458.

25. Balster, L.M.; Corporan, E.; DeWitt, M.J.; Edwards, J.T.; Ervin, J.S.; Graham, J.L.; Lee, S.Y.; Pal, S.; Phelps, D.K.; Rudnick, L.R.; Santoro, R.J.; Schobert, H.H.; Shafer, L.M.; Striebich, R.C.; West, Z.J.; Wilson, G.R.; Woodward, R.; Zabarnick S. Development of an Advanced, Thermally Stable, Coal-Based Jet Fuel. *Fuel Process. Technol.* **2008**, *89*, 364 – 378.

26. "Final Report for Alternative Fuels Task: Impact of SPK Fuels and Fuel Blends on Non-metallic Materials used in Commercial Aircraft Fuel Systems," FAA Office of Environment and Energy under CLEEN OTA Number: DTFAWA-10-C-0030, December, 2013.

27. Mathai, A.E.; Thomas, S.J. Transport of Aromatic Hydrocarbons through Crosslinked Nitrile Rubber Membranes. *J Macromol Sci, Phys.* **1996**, *B35* (2), 229-253.

28. Mehl, M.; Pitz, W.J.; Westbrook, C.K.; Curran, H.J. Kinetic Modeling of Gasoline Surrogate Components and Mixtures Under Engine Conditions. *Proc.Combust.Inst.* **2011**, *33* (1), 193–200.

29. Jennerwein, M.K.;, Eschner, M.; Gröger, T.; Wilhamr, T.; Zimmerman, R. Complete Group-Type Quantification of Petroleum Middle Distillates Based on Comprehensive Two Dimensional Gas Chromatography Time-of-Flight Mass Spectrometry (GCxGC-TOFMS) and Visual Basic Scripting. *Energy Fuel* **2014**, *28* (9), 5670-5681.

30. Bernabei, M.; Reda, R.; Galiero, R.; Bocchinfuso, G. Determination of Total Polycylic Aromatic Hydrocarbons in Aviation Fuel. *J. Chromatogr. A* **2003**, *985* (1-2), 197-203.

31. Standard Specification for Aviation Turbine Fuels; Designation No. D1655 – 18a; ASTM International: West Conshohocken, PA 2018.

32. Maciel, A.V.; Machado, J.C.; Pasa, V.M. The Effect of Temperature on the Properties of NBR/PVC Blend Exposed to Ethanol Fuel and Different Gasolines. *Fuel*, **2013**, *113*, 679-689.

33. Gawron, B.; Białecki, T. Impact of a Jet A-1/HEFA Blend on the Performance and Emission Characteristics of a Miniature Turbojet Engine. *Int. J. Environ. Sci. Technol.* **2018**, *15* (7), 1501-1508.

34. Luning Prak, D.J.; Romanczyk, M.; Wehde, K.E.; Ye, S.; McLaughlin, M.; Luning Prak, P.J.; Foley, M.P.; Kenttämaa, H.I.; Truelove, P.C.; Kilaz, G.; Xu, L.; Cowart, J.S. Analysis of Catalytic Hydrothermal Conversion Jet Fuel and Surrogate Mixture Formulation: Components, Properties, and Combustion. *Energy Fuels* **2017**, *31* (12), 13802-13814.

VITA

Mark Romanczyk was born in Scranton, Pennsylvania. His parents are David and Roseann Romanczyk who live in Dickson City, PA. His brother is Gregory Romanczyk, a professional engineer, who lives in Miami Beach, FL. Mark attended the Pennsylvania State University and majored in Biology, where he graduated with distinction. He obtained a master's degree in Biochemistry from the University of Scranton under the direction of Dr. Joe Vinson and was class salutatorian. He was hired as a Lecturer at the University of Scranton, where he taught general chemistry, organic chemistry and forensic science for several years. Upon receiving acceptance into medical school and graduate school, he decided to enroll at Purdue University to obtain a PhD in Chemistry in 2013. He worked for Professor Hilkka Kenttämaa and defended his work on January 18, 2019.

PUBLICATIONS

1. **Romanczyk, M**.; Ramirez, J.H.; Xu, L.; Vozka, P.; Dissanayake, P.; Wehde, K.E.; Roe, N.; Keating, E.; Kilaz, G.; Trice, R. W.; Luning Prak, D.J. Kenttämaa, H.I. The Capability of Organic Compounds to Swell Acrylonitrile Butadiene O-rings and Their Effects on O-ring mechanical Properties. *Fuel*. **2019**, *238*, 483 – 492.

2. Yerabolu, R.; Kotha, R.R.; Niyonsaba, E.; Dong, X,; Manheim, J.M.; Riedeman, J.S.; **Romanczyk, M**.; Johnston, C.T.; Kilaz, G.; Kenttämaa, H.I. Molecular Profiling of Crude Oil by Distillation Precipitation Fractionation Mass Spectrometry (DPF-MS). *Fuel*, **2018**, *234*, 492 – 501.

3. Luning Prak, D.J.; **Romanczyk, M**.; Wehde, K.E.; Ye, S.; McLaughlin, M.; Luning Prak, P.J.; Foley, M.P.; Kenttämaa, H.I.; Truelove, P.C.; Kilaz, G.; Xu, L.; Cowart, J.S. Analysis of Catalytic Hydrothermal Conversion Jet Fuel and Surrogate Mixture Formulation: Components, Properties, and Combustion. *Energy Fuels*, **2017**, *31*, 13802 – 13814.

4. Jin, C.; Viidanoja, J.; Li, M.; Zhang, Y.; Ikonen, E.; Root, A.; **Romanczyk, M.**; Manheim, J.M.; Dziekonski, E.; Kenttämaa, H.I. Comparison of Atmospheric Pressure Chemical Ionization and Fueld Ionization Mass Spectrometry for the Analysis of Large Saturated Hydrocarbons. *Anal Chem.* **2016**, *88*, 10592 – 10598.